論文 / 著書情報
Article / Book Information

題目(和文)	
Title(English)	In-situ electron microscope study on a LiMn2O4 Li-ion battery cathode
著者(和文)	LeeSoyeon
Author(English)	Soyeon Lee
出典(和文)	学位:博士(理学), 学位授与機関:東京工業大学, 報告番号:甲第9414号, 授与年月日:2014年3月26日, 学位の種別:課程博士, 審査員:山本　直紀,菅野　了次,平山　博之,佐々木　聡,川路　均
Citation(English)	Degree:Doctor (Science), Conferring organization: Tokyo Institute of Technology, Report number:甲第9414号, Conferred date:2014/3/26, Degree Type:Course doctor, Examiner:,,,,
学位種別(和文)	博士論文
Type(English)	Doctoral Thesis

In-situ electron microscope study on a $LiMn_2O_4$ Li-ion battery cathode

A DISSERTATION SUBMITTED TO
THE COMMITTEE ON GRADUATE STUDIES OF
TOKYO INSTITUTE OF TECHNOLOGY
IN PARTIAL FULLFILLMENT OF THE REQUIREMENTS FOR THE DEGREE OF
DOCTOR OF PHILOSOPHY

DEPARTMENT OF MATERIAL SCIENCE AND ENGINEERING

BY

SOYEON LEE
(이 소연)
(李 少淵)

TOKYO INSTITUTE OF TECHNOLOGY

FEBRUARY 2014

Committee

Prof. N. Yamamoto (Supervisor)	Quantum Nanoelectronics research center, Tokyo Institute of Technology
Prof. S. Sasaki	Materials and Structure Lab., Tokyo Institute of Technology
Prof. H. Hirayama	Material Science and Engineering, Tokyo Institute of Technology
Prof. H. Kawaji	Materials and Structure Lab., Tokyo Institute of Technology
Prof. R. Kanno	Electronic chemistry, Tokyo Institute of Technology

Abstract

In-situ transmission electron microscope (TEM) observation of a $LiMn_2O_4$ nanowire battery was performed for revealing the mechanism of capacity fade out during 4 V charge/discharge reaction. $LiMn_2O_4$ crystal is a promising cathode material for lithium ion batteries (LIBs) because of the high natural abundance of manganese.

This thesis consists of six chapters. In chapter 1, the structure of LIBs and the aging phenomena which is important issue for long life time of LIBs are introduced. To improve the life time, the aging mechanism, irreversible local structure change, is required to be understood. Therefore, real-time observation during charge-discharge cycles was performed by TEM.

In chapter 2, as a new microscope method to image lithium ion behavior in LIBs, annular bright field (ABF) imaging was investigated. We demonstrated that lithium atoms in the diffusion channel of the spinel structure (a thin LiV_2O_4 crystal) were visualized and their number was countable one-by-one by using ABF imaging method: the lithium column intensity varied with increasing number of single lithium atoms in correlation with the thickness change of the LiV_2O_4 crystal.

A through-focus series of ABF images of a thin $LiMn_2O_4$ crystal were observed in order to clarify the image mechanism. Contrast reversal of an atomic column depending on the defocus reversal proved the ABF imaging to be a potential imaging of individual atomic columns.

The proportional relationship of the ABF image contrast to the number of ions has enabled us to study motion of ions through the contrast change accompanied with structure change. During the structural transformation of spinel LiV_2O_4 crystals into defective $Li_xV_2O_4$, ABF images revealed that lithium ions displacement from the tetrahedral sites induced the redistribution of vanadium ions at octahedral sites. *In-situ* ABF imaging of thin specimens is a promising method for investigating local structural transformations accompanied by lithium movement.

The ABF image taken with a large convergence angle is sensitive to the top surface and is useful to image the surface profile of LIB electrode materials such as vacancy or adsorption.

From the chapter 3, we focused on the structure change of a $LiMn_2O_4$ cathode material during the battery cycles. In chapter 3, the development of a “nano-battery” using $LiMn_2O_4$ nanowires is introduced. The $LiMn_2O_4$ nanowires were suspended on ionic liquid electrolyte placed upon $Li_4Ti_5O_{12}$ anode. The nano-battery was observed to work as a 4V rechargeable battery, showing clear current peaks in the cyclic voltammetry.

In chapter 4, during charge and discharge cycles, structure change was observed by *in-situ* TEM with simultaneous electrochemical measurement which was cyclic voltammetry. The $LiMn_2O_4$ nanowire cathode was found to be changed partially into the tetragonal phase (Li excess state) at

the interface region adjacent to the electrolyte during the discharge process of the 4 V reaction (vs Li/Li^+). The lithium ions were inserted into the nanowire at higher rate than diffused to the bulk-side of the nanowire. The tetragonal phase of the $LiMn_2O_4$ cathode was restored to be cubic phase without any fracture in the charge process. No fracture while cubic-tetragonal transition is promising for the long-life-time battery with $LiMn_2O_4$ nanowire cathode.

In chapter 5, we developed a single nanowire battery for investigating lithium diffusion behavior in the bulk-side of $LiMn_2O_4$ nanowire. During a discharge-charge process, the phase boundary between Li-poor and Li-rich cubic structures was probed. The phase boundary advanced toward Li-poor phase during discharge process, indicating the volume of Li-poor phase decreased. The phase boundary movement reversed during charge process. However, the phase boundary was observed to move even after cathodic/anodic current stopped. It indicated that lithium ions diffusion was not limited by the phase transformation. The charge capacity estimated from the phase boundary movement was about 30 times smaller than the one estimated from the simultaneously obtained CV curve. The phase transformation is considered to occur at multiple positions along the nanowire simultaneously and to be completed with the time delay due to redistribution of lithium ions inside the nanowire after charge/discharge process.

In this study, the phase transformation of a $LiMn_2O_4$ crystal during charge/discharge process was observed at the bulk-side of $LiMn_2O_4$ nanowire and at the interface region between $LiMn_2O_4$ and the electrolyte. Lithium diffusion inside $LiMn_2O_4$ nanowire was not limited by the phase transformation between Li-poor and Li-rich phases. However, the lithium insertion rate from the electrolyte into $LiMn_2O_4$ was still higher than the rate of lithium diffusion from the interface region to bulk-side of the $LiMn_2O_4$ nanowire.

This study suggests that the 1-dimentional morphology is the most profit for a $LiMn_2O_4$ cathode material. It prevents the capacity fade out due to the severe volume change of $LiMn_2O_4$ crystals during the transformation between tetragonal and cubic phases. For the case of common batteries where whole body of a $LiMn_2O_4$ crystal is soaked in electrolyte the 1-dimentional morphology allow whole body of the nanowire to be regarded as interface region with electrolyte. It would enable fast charge/discharge process.

CONTENTS

Chapter 1. Introduction

During past two decades the lithium ion battery (LIB) market has increased (Figure 1.1). The recent commercialization of electric vehicle (EV) accelerates to increase the demand of LIBs (Figure 1.2). LIBs become one of the most important devices in today's mobile society, being applied from small smart phones to huge energy storages [1,2,3,4,5].

LIBs are required to have the higher battery performance – higher power, higher energy density, low cost and long lifetime (Figure 1.3) although current LIBs show prior performances to conventional rechargeable batteries such Ni-Cd and lead batteries [1,2,3,4,5]. For better battery performance, a lot of methodologies to design LIBs have been developed. Also, a huge amount of researches have been performed to understand the phenomena in LIBs such as lithium diffusion mechanism, surface chemical reaction, structure change and so on.

In this chapter, we review the LIBs, our research object. The structure and issues of LIBs are given in section 1.1, the structure and electrochemical properties of $LiMn_2O_4$ cathode materials in section 1.2. In section 1.3, the purpose of this study is given.

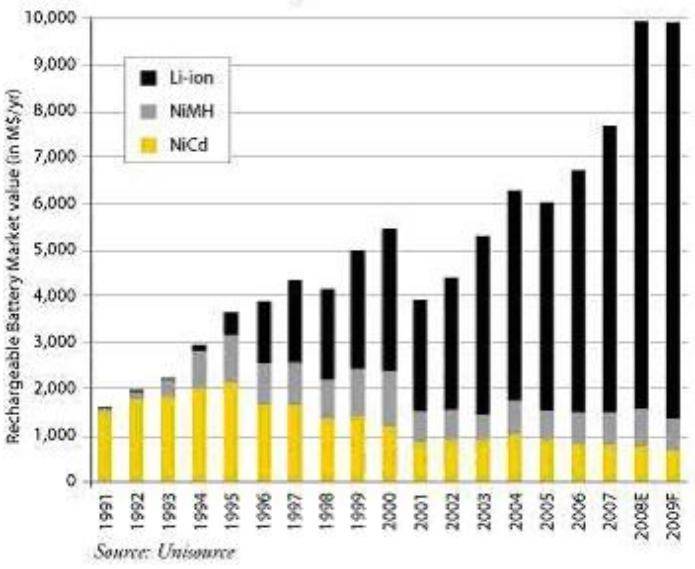

Source : Unisource

Figure 1.1. The change of rechargeable battery market value.

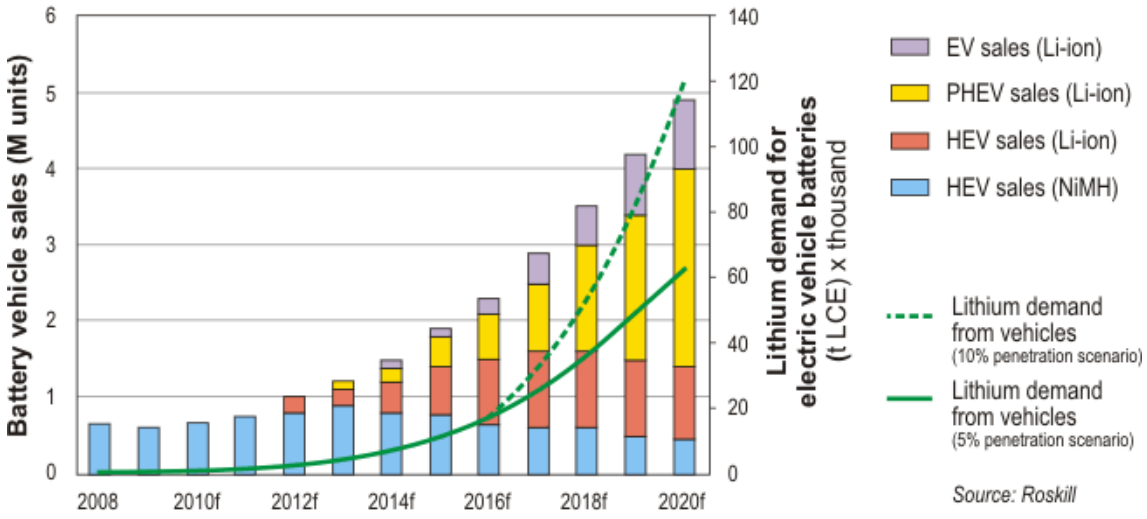

Figure 1.2. World electric vehicle production and lithium demand

Class	End of FY2012	FY2020
High power LIBs	Energy density: 30-50Wh/kg, Powerdensity: 1400-2000W/kg Cost: ¥100k-150k/kWh	200Wh/kg 2500W/kg ¥20k/kWh
	Calendar life: 5-10 years Cycle life: 2000-4000	10-15 years 4000-6000
High energy density LIBs	Energy density: 60-100Wh/kg, Powerdensity: 330-600W/kg Cost: ¥70k-100k/kWh	250Wh/kg 1500W/kg ¥20k/kWh
	Calendar life: 5-10 years Cycle life: 500-1000	10-15 years 1000-1500
Spec of LIBs For EV	The driving range: 120-200km Weight of LIB packs: 200-300kg Capacity of LIB packs: 16-24kWh Cost of LIB packs: ¥1100k-2400k Cost of vehicle: ¥2600k-3760k	250-350km 100-140kg 25-35kWh ¥500k-800k ¥2000k-2300k

Figure 1.3 Now and future of LIB for electric vehicle from NEDO roadmap 2013

1.1 Lithium Ion batteries (LIBs)

1.1.1 Lithium ion batteries of actual

Lithium ion battery (LIB) was originated from lithium metal battery. Lithium metal battery was proposed in 1970s [1,6], but owing to the safety problem, lithium metal was alternated with electrode which is containing lithium ions and able to lithium-intercalation. In 1991, Sony and Asahi Kasei released the first commercial LIB [1], having same construction with current commercial LIBs: $LiCoO_2$ cathode and graphite anode.

Figure 1.4 shows the schematic geometric structure of the current LIB [1]. Cathode (positive electrode) and anode (negative electrode) is separated by electrolyte which have ionic conductivity but no electric conductivity. During discharge, due to the difference of electrochemical potential (voltage) between two electrodes, electrons are flows from anode to cathode (circuit current flow from cathode to anode). Inside the LIB, lithium ions are diffused from anode to cathode through the electrolyte. The chemical reaction during discharge is as follows;

Anode: $Li_xC \rightarrow x\ Li^+ + x\ e^- + C$

Cathode: $x\ Li^+ + x\ e^- + Li_{1-x}CoO_2 \rightarrow LiCoO_2$

Overall reaction: $Li_{1-x}CoO_2 + Li_xC \rightarrow LiCoO_2 + C$

During the charge/discharge reaction, the charge neutrality in cathode materials can be satisfied by changing the valance of transition metal ions.

Figure 1.5 shows the electronic band structure of LIBs. The open circuit voltage (OCV, V_{oc}) is given by the difference of electrochemical potential between cathode (μ_C) and anode (μ_A) [6];

$eV_{oc} = \mu_C - \mu_A$

Where *e* represents the electron charge. Thus, the higher cell voltage can be acquired by the pair of the cathode of the lower electrochemical potential and the anode of the higher one.

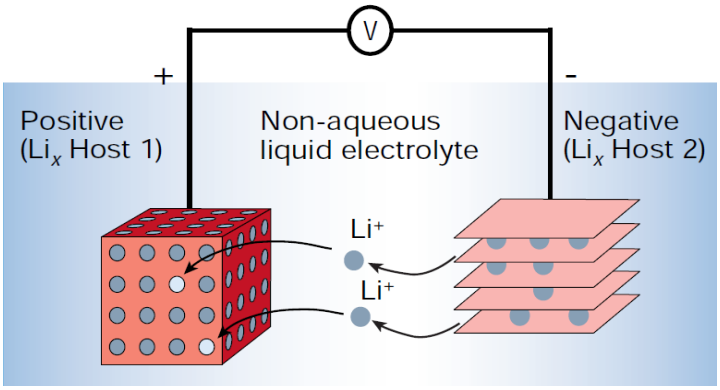

Figure 1.4 The schematic of the structure and reaction in a lithium ion battery [1]

As mentioned above, electrolyte has to have no electric conductivity so as to avoid internal contact between cathode and anode (short circuit). Furthermore, electrolyte needs to have wide band gap, E_g. The lowest unoccupied molecular orbital (LUMO) have to be higher than the electrochemical potential of anode (μ_A). When μ_A is higher than LUMO of electrolyte, electrolyte is reduced, resulting solid electrolyte interface (SEI) layer formation at the electrolyte/anode interface [7]. The reduction of electrolyte (or formation of SEI) continues until the IR drop due to the SEI becomes the same with the difference between μ_A and LUMO. Similarly, the highest occupied molecular orbital (HOMO) of electrolyte have to be lower than the electrochemical potential of cathode (μ_C). If not, electrolyte is oxidized, resulting SEI layer formation at the electrolyte/cathode interface. If the formed SEI layer is not dense and stable enough to passivate the electrode, the cell capacity becomes fade out due to the decomposition of the electrolyte and the electrodes.

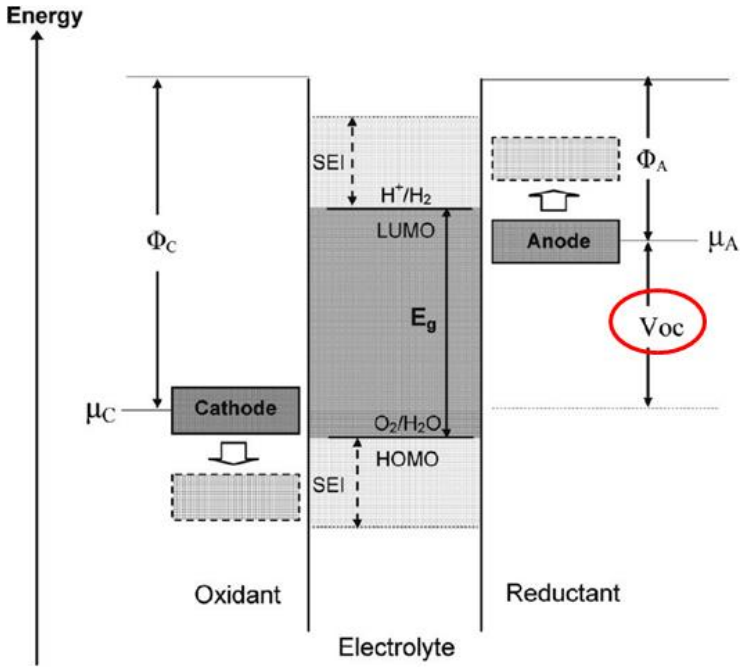

Figure 1.5 The electronic band structure of LIBs. [6]

1.1.2 Lithium ion batteries for future

LIBs are subject to improve the following four properties: high power (V), high energy density (C/g and C/cm^3), low cost and long lifetime (calendar and cycle lifetime). For these four properties, the required properties of each component are listed in Table 1.1.

LIBs consist of three components – cathode, electrolyte and anode. Among them, in this study, cathode materials are focused. Widely used cathode material is $LiCoO_2$. $LiCoO_2$ has high reaction voltage (~4 V) and relatively good energy density (~140 mAh/g) [1,8]. Furthermore, $LiCoO_2$ shows good cycle properties of small capacity fading rate, and is easily obtained by simple synthesis methods. However, $LiCoO_2$ costs high due to cobalt of a limited reserve. To improve the four properties, other material systems having low amount of or having no cobalt are under consideration.

Figure 1.6 shows the voltage versus capacity for cathode materials presently used or under considerations for the next generation of rechargeable Li-based cell. Among them three systems, $LiMn_{1/3}Ni_{1/3}Co_{1/3}O_2$, $LiFePO_4$, $LiMn_2O_4$ marked by red circles have been developed extensively and shown good cycle property. $LiMn_{1/3}Ni_{1/3}Co_{1/3}O_2$ shows relatively high energy density (~170mAh/g), and costs lower than $LiCoO_2$ by substituting cobalt ions with manganese and nickel ions [9]. $LiFePO_4$ costs lowest because of not using cobalt [10,11]. Some challenge has been undertaken to increase the low reaction voltage (~3.5 V) by replacing iron with other transition metal such as manganese and cobalt [11,12]. $LiMn_2O_4$ is one of the most promising cathode materials due to high reaction voltage (~4 V) and costs low [13]. $LiMn_2O_4$ is commercialized as LIBs for electric vehicles (EVs). Spinel structure which $LiMn_2O_4$ have gives higher reaction voltage, e.g. 5V, by substituting manganese with other transition metal ions (Cr, Fe, Co, Ni, Cu) [14,15,16]. Among the substituted spinel oxide, $LiNi_{0.5}Mn_{1.5}O_4$ shows stable charge/discharge cycle property [17].

Recent development of EV requires fast charge/discharge rate in addition to the four properties. For fast charge/discharge, the morphology of cathode materials became the subject to be designed. Figure 1.7 shows nano-structured cathode materials – mesoporous crystals [18,19] and crystalline nanowires [20,21]. During fast charge/discharge rate, more than 30 C, nano-structured cathode materials show capacity retention, 50 % higher than that of the commercial powder [18,20]. It is important issue to reveal the mechanism of such high retention for fast charge/discharge cycles.

Table 1.1 The required properties of LIB components

Class	Requirement
Cathode	•**High voltage** •**High energy density** (capacity/mass or vol.) •Good Electrical conductivity
Electrolyte	•**Wide potential window** (wide band gap) •**High Li diffusivity** •**Electrical insulator** •(Stable-SEI formable)
Anode	•**Low voltage** •**High energy density** (capacity/mass or vol.) •Good Electrical conductivity
All	•**Low cost** •Simple synthesis process •**Long life** •High Li diffusivity •Low toxic •Environment friendly •Abundant reserves

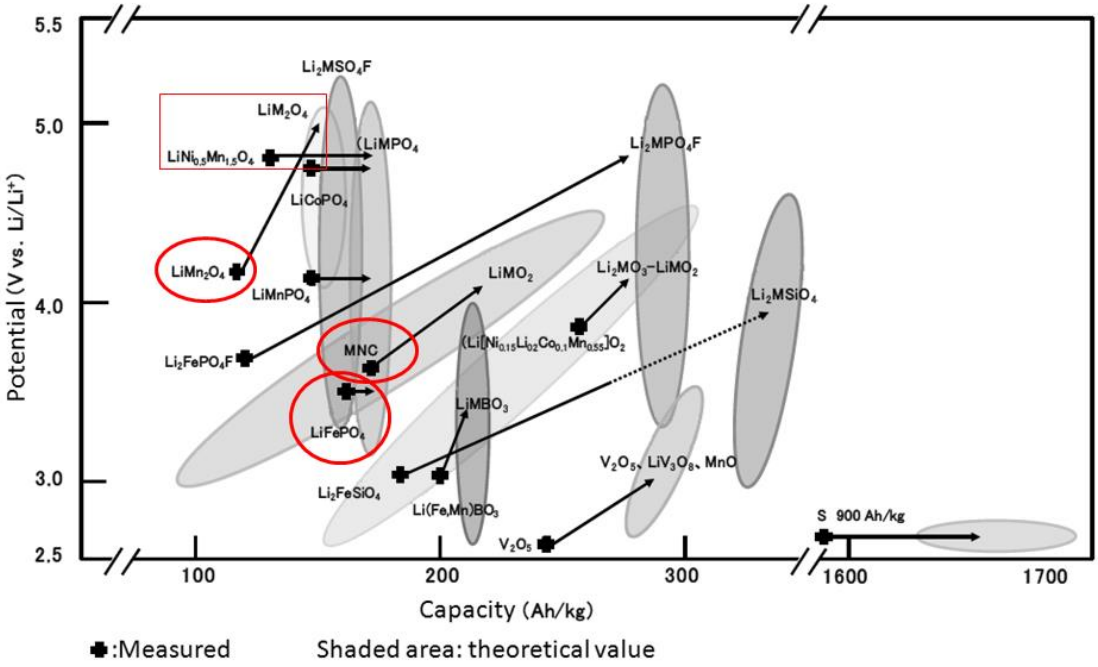

Figure 1.6 Voltage versus capacity for cathode materials presently used or under considerations for the next generation of rechargeable Li-based cell (NEDO roadmap 2013). Black plus shows current properties and arrows, developing tendency. Mainly developed three systems are marked by red circles. Spinel system showing high voltage is marked by a red rectangle.

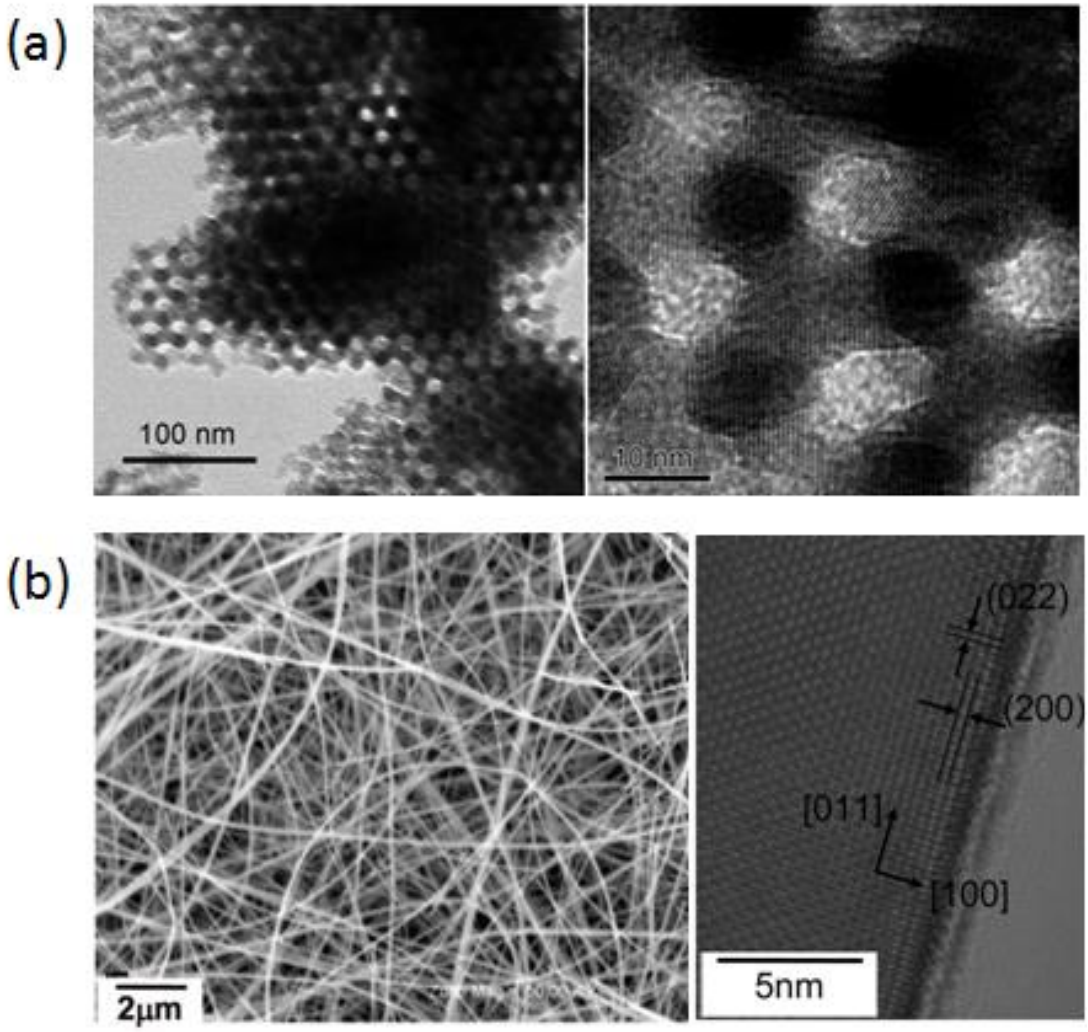

Figure 1.7 (a) TEM images of mesoporous $LiMn_2O_4$ crystals [18] (b) SEM and TEM images of the synthesized single crystalline spinel $LiMn_2O_4$ nanowires. [20]

1.1.3 Interface between electrode and electrolyte

The interface between electrode and electrolyte is the place where lithium ions are inserted and extracted. The interface structure can affect the lithium movements and can be changed by lithium movements. The interface structure can also be changed by the electronic structure of electrode and electrolyte, resulting formation of solid electrolyte interface (SEI) layer as mentioned in section 1.1.1. Such interface structure changes have been the issue for improving the battery performance.

The changes of the interface structure have been investigated with various techniques, such electrochemical measurements, spectroscopy, diffraction and microscopy. Electrochemical measurement such as impedance spectroscopy [22,23] is one of the most popular methods to monitor the interface structure. The impedance and capacity change due to the structure change at the interface is monitored by analysis with a model equivalent circuit. By using impedance spectroscopy, it is able to obtain not only the resistance and capacity of the interface between electrode and electrolyte, but also the conductance of each element (electrodes, electrolyte, current collector) and the capacity of the interface between each element. Potentiostatic intermittent titration technique (PITT) has been also reported to be able to monitor the resistance to surface reaction of electrodes [24]

The SEI formation on anode has been investigated by Fourier-transform infrared and Raman spectroscopy studies [25,26]. The formation process and the composition of SEI layer have been identified in conjunction with electrochemical techniques [27]. The composition of SEI layer has also been investigated by X-ray photospectroscopy [28], energy dispersive analysis of X-ray [29] and electron energy loss spectroscopy [30]. The SEI layer on graphite anode for several electrolyte systems was classified in three types – well developed SEI, limiting intercalation and badly damaging electrode as shown in Figure 1.8

The stability of electrode surface in electrolyte is one of interesting issues of LIBs. *Ex-situ* and *in-situ* X-ray diffraction (XRD) has revealed the change of the surface structure of electrode materials [31,32]. *In-situ* surface XRD study has been reported that the surface of $LiMn_2O_4$ crystals changed for each stage of battery cycles as shown in Figure 1.9 [32]. The dependence of surface stability on the crystal plane was pointed out that the (111) plane is more stable than the (110) plane for $LiMn_2O_4$ crystals. This result has been reproduced by the electrochemical evaluating the nanoparticles whose surfaces are mostly the {111} planes [33].

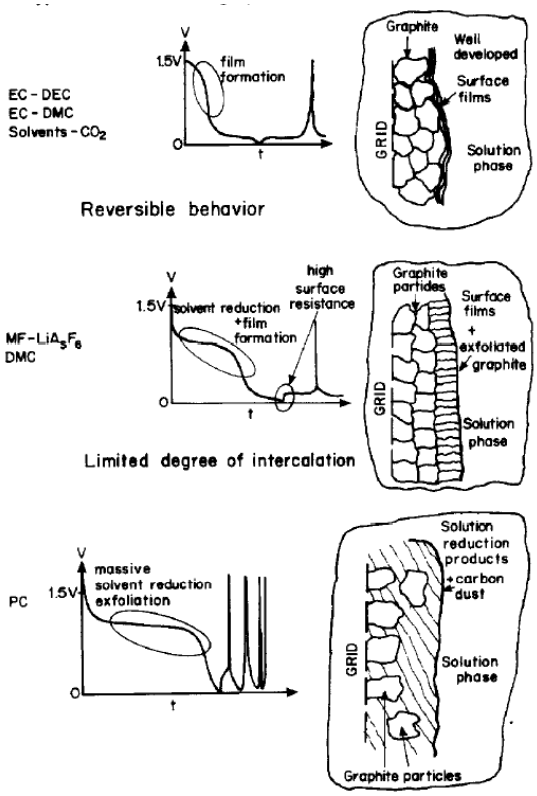

Figure 1.8 Three typical SEI layers and behaviors during battery cycles [7]

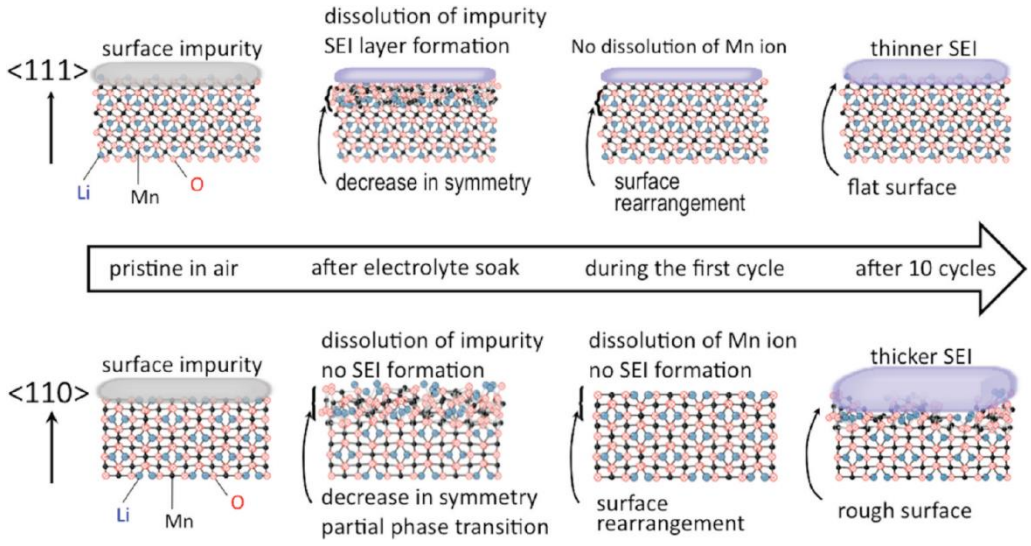

Figure 1.9 The surface structure change of $LiMn_2O_4$ cathode materials for each stage from synthesis to after 10 cycles. [32]

Microscope techniques have given the important information about local structure. *In-situ* SEM has visualized the morphology change such formation of dendrites. Figure 1.10(a) shows the lithium dendrite at the anode surface after cycles [34]. Lithium dendrite, which can make short circuit, caused the explosion of lithium battery. Figure 1.10(b) shows the cupper dendrite formation at the cathode surface. The dendrites were formed due to the lithium insertion during discharge, and caused the physical fracture of cathode [35].

The locally changed structure of cathode material has been investigated by transmission electron microscopy (TEM) [36,37]. Figure 1.11 shows a TEM image of $LiMn_2O_4$ particles after discharge above 3.3 V vs Li/Li^+, where the surface has transformed into the tetragonal phase from the cubic phase [36]. Such structure change localized at surface area was proposed to cause capacity fading out; Large lattice mismatch of the tetragonal and cubic phase (18 %) can cause physical fracture of $LiMn_2O_4$ particles [37,38]. TEM technique coupled with electron energy loss spectroscopy (EELS) has been revealed the inhomogeneous distribution of transition metal ions in cathode materials after charge/discharge cycles [39]. Figure 1.12 is the EELS mapping of Ni^{2+} distribution in $LiNi_{0.8}Co_{0.15}Al_{0.05}O_2$ cathode materials before and after 500 cycles. After the cycles the nickel ions (Ni^{2+}) have increased in vicinity of grain boundary, which suggests the formation of NiO-type phase. It indicates that the capacity fading out of $LiNi_{0.8}Co_{0.15}Al_{0.05}O_2$ cathode materials is originated by the formation of inactive NiO-type phase at the grain boundary.

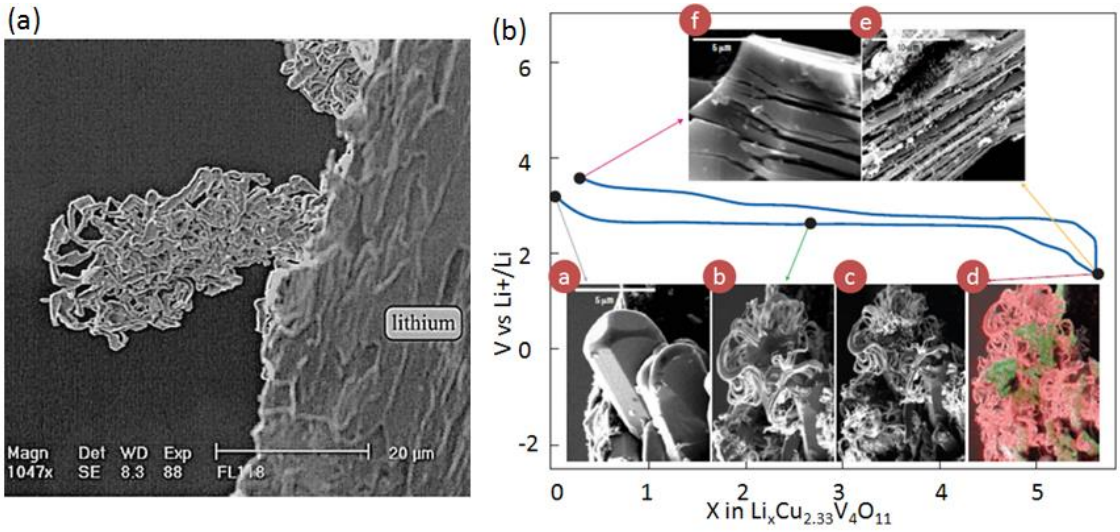

Figure 1.10 (a) The SEM image of lithium dendrites on the surface of lithium anode [34]. (b) *In-situ* SEM observations of a Cu2.33V4O11/Li cell during charge/discharge cycling. The cell was initially dischared (a~d), and then charged (e~f). The energy-dispersive X-ray spectrometry mappings are shown in d (the red and green colours for Cu and V metal) [35]

Recently, *in-situ* TEM observations have been performed on various electrode materials, Si, SnO and etc [40-49]. The atomic structure change as well as morphology change was monitored, giving hints of physics and/or chemistry of batteries. However, simultaneous electrochemical measurement has not been obtained. The relationship between electrochemical properties and structure change is important for understanding the dynamics of lithium diffusion and phase transformation. The dynamics which the battery reaction follows is important issue for design of LIBs.

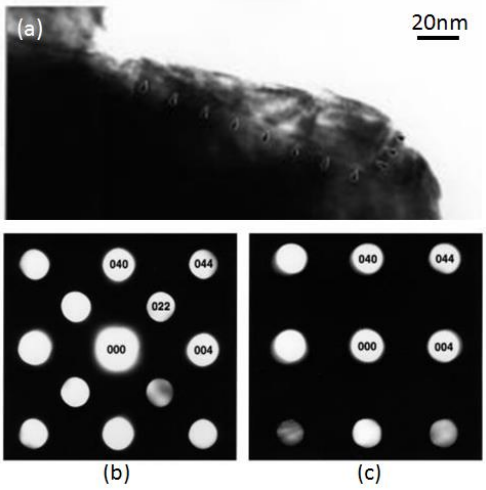

Figure 1.11 (a) The TEM image of a $LiMn_2O_4$ crystal discharged above 3.3V vs Li/Li^+ having two phases (indicated by black arrows). (b) The nano beam diffraction pattern obtained from bulk phase showing cubic spinel lattice. (c) The nano beam diffraction pattern obtained from the surface indicated by black arrows in a showing tetragonal lattice [36]

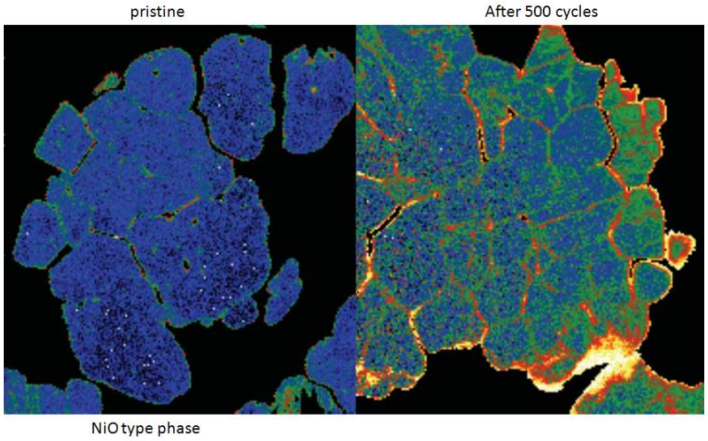

Figure 1.12 The Ni^{2+} distribution EELS mapping in $LiNi_{0.8}Co_{0.15}Al_{0.05}O_2$ cathode materials before and after 500 charge/discharge cycles. [39]

1.1.4 Aging Issues of cathode materials

Cathode consists of active materials, conductive carbon, polymer binder and metal current collector. So, the aging mechanism of cathode can be distinguished by two classes. One is degradation of active materials, which is the storage host of lithium ions. The other is degradation of non-active materials, such oxidation of conductive particle, corrosion of current collector and binder decomposition (Figure 1.13) [50].

The degradation of active materials can also be classified in two kinds of groups. One increases the impedance at the surface: Thick SEI formation by electrolyte decomposition and precipitation of new inactive phase. The other decreases the capacity of the active material particle due to micro-cracking, dissolution of matal ions and/or oxygen ions, and structural disordering. Ni-including active materials – $LiNiO_2$ and $LiMNiO_2$ (M=Mn, Co, etc) have been pointed out to be degraded by Ni substitutional defect at Li site (disordering) [51], new inactive phase formation and Ni dissolution [52]. Spine $LiMn_2O_4$ crystals have been pointed out to suffer from Jahn-Teller distortion [38], Mn dissolution [53], microstrain [54] and etc.

Most of aging behaviors are local structural change of cathode materials. The aging mechanism is to be clarified by microscopy, the technique which gives the information about local structure.

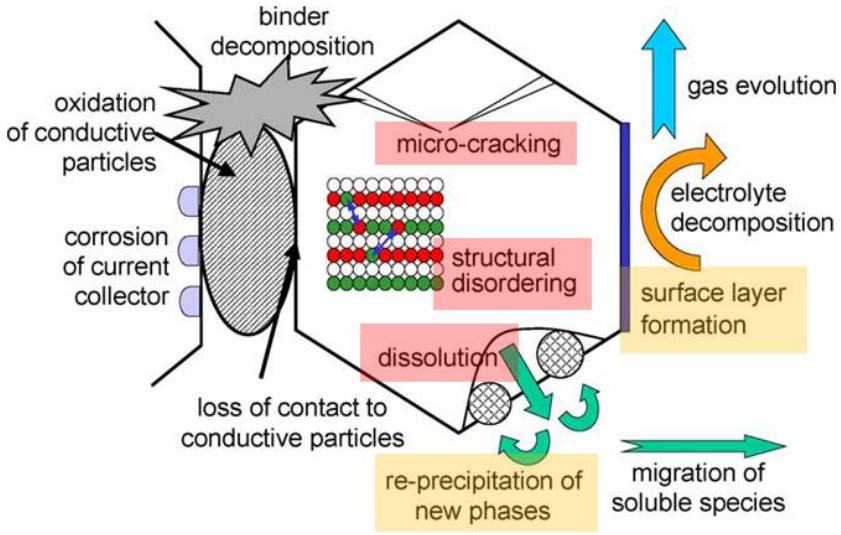

Figure 1.13 The schematic of aging behaviors of cathode. [50]

1.2 Lithium Manganese Oxide

1.2.1 Structure-Spinel

Lithium manganese oxide ($LiMn_2O_4$) crystal, one of the most promising cathode materials for lithium ion batteries due to the advantages of environmental harmlessness, great natural abundance, good safety and low cost [1,2,5,13], has the normal spinel structure. The normal spinel minerals have the formula AB_2O_4. Cations A are positioned at the tetrahedral site (8a), cations B are positioned at the octahedral site (16d) in the cubic close packed array of oxygen ions. For $LiMn_2O_4$ crystals, lithium ions occupy 8a sites and manganese ions, 16d sites [13] .

Figure 1.14 shows the atomic structure of $LiMn_2O_4$ crystals. A MnO_6 octahedron shares sides with neighbor MnO6 octahedrons, which align along the [110] direction. Along the [100] direction, the lines of MnO_6 octahedrons are aligned with 4-folded screw symmetry. Lithium ions diffuse in the scaffold of MnO_6 octahedrons in order of 8a-16c-8a-…. [55-57]

Figure 1.15 shows the atomic structure of $LiMn_2O_4$ crystals of the [110] view. In this view, each atomic column contains only one kind of elements. In the rhombic unit cell (marked by black line in right side), there are two atomic columns, each of which contain lithium ions. They construct the lithium diffusion channel (8a-16c-8a-…). The atomic structure of $LiMn_2O_4$ crystals viewed from the [100] direction is shown in Figure 1.16.

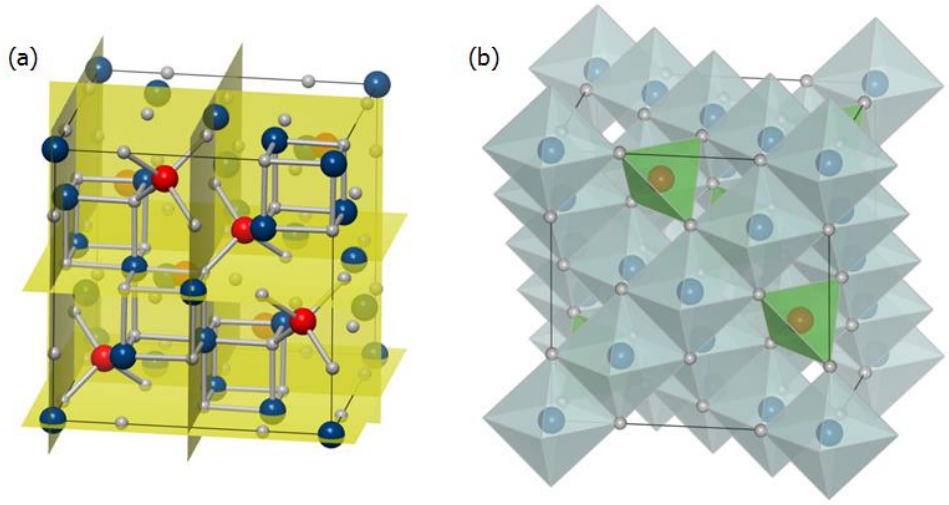

Figure 1.14 The normal spinel structure of $LiMn_2O_4$ crystals. Red spheres are lithium cations, blue ones are manganese cations and gray ones, oxygen anions which has the cubic close packed array structure. (a) spinel structure consists of 8 parts, each of which has one LiO_4 tetrahedron and one Mn_4O_4 cube. (b) spinel structure expressed with polyhedra network. Blue one is a MnO_6 octahedron, green one is a LiO_4 tetrahedron.

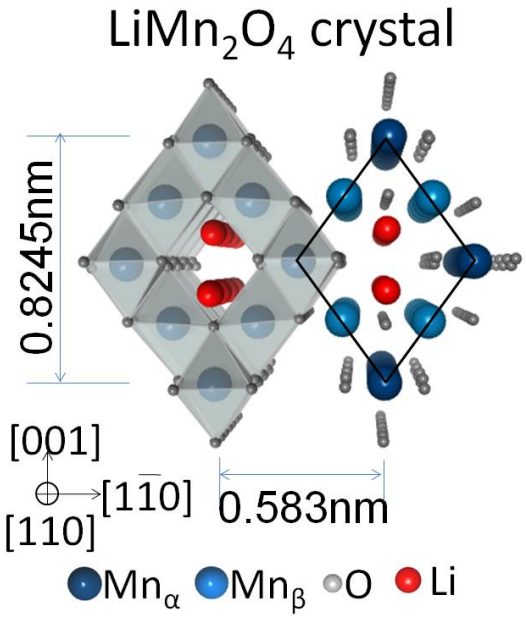

Figure 1.15 The atomic structure of $LiMn_2O_4$ crystals viewed from the [110] direction. Each atomic column consists of one element. Among Mn columns, there are two site, a and b. a site has twice high density of manganese ions as that in b site. The ratio of the ion density for all kinds of atomic columns along the [110] direction is as follow-Mn a:Mn b:O:Li=2:1:2:1.

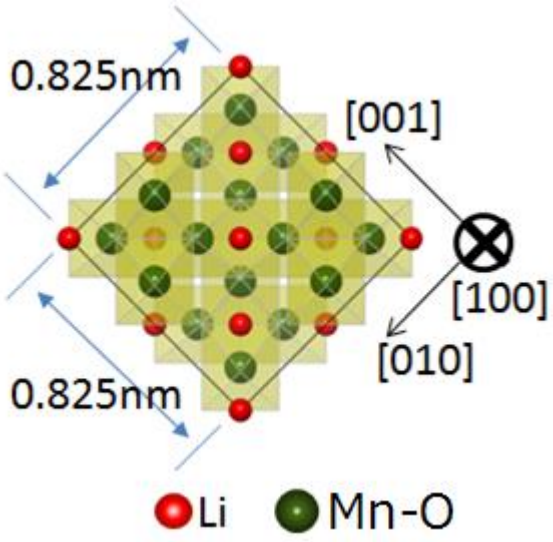

Figure 1.16 The atomic structure of $LiMn_2O_4$ crystal viewed from the [100] direction. In this view direction, Li column has only lithium ions, but Mn-O column has manganese ions and oxygen ions alternatively.

1.2.2 Electrochemical properties and structure change

The electrochemical reaction of $Li_xMn_2O_4$ crystals (0<x<2) is classified by two voltage ranges, 3 and 4 V verse standard lithium electrode. Figure 1.17 shows the voltage profile of $Li_xMn_2O_4$ crystals as a function of lithium composition, x (top of Figure) and capacity (bottom of Figure). In the profile, there are three plateaus - 2.7 V, 3.9 V and 4.1 V [6,13,58-60]. At 4.1 V, two phases, $Li_xMn_2O_4$ (x~0.1 [59,60]) and $Li_{0.5}Mn_2O_4$ phases coexist (first order phase transition) [13,59,60]. At 3.9 V, $Li_{0.5}Mn_2O_4$ crystal becomes $LiMn_2O_4$ by the lithiation of second order phase transition [13,59,60]. The voltage is shifted from 4 V to 3 V when the lithium insertion site is changed from tetrahedral site (8a) to octahedral site (16c) [6,58]. It corresponds to the point that the composition of lithium equals 1. At the 2.7 V, $LiMn_2O_4$ and $Li_2Mn_2O_4$ phases coexist (first order phase transition) [58].

Figure 1.18 shows the results of *in-situ* XRD, which shows the lattice parameter change during the discharge process in the range of 0<x<1 in $Li_xMn_2O_4$. In the range of 0.35<x<1, which corresponds to the 3.9 V reaction, only one phase was detected. While two phases were detected in the range of 0.35<x<0.1, which corresponds to the 4.1 V reaction.

The structure of $Li_xMn_2O_4$ crystals for each phase is shown in Figure 1.19. $LiMn_2O_4$ crystals have the normal spinel structure mentioned in section 1.2.1. The $Li_xMn_2O_4$ crystals (x~0.1) have the spinel structure where lithium site (8a) is empty, but the scaffold of MnO_6 octahedrons is maintained. The structure of $Li_{0.5}Mn_2O_4$ crystals is not still identified despite of lots of previous studies [60-67].

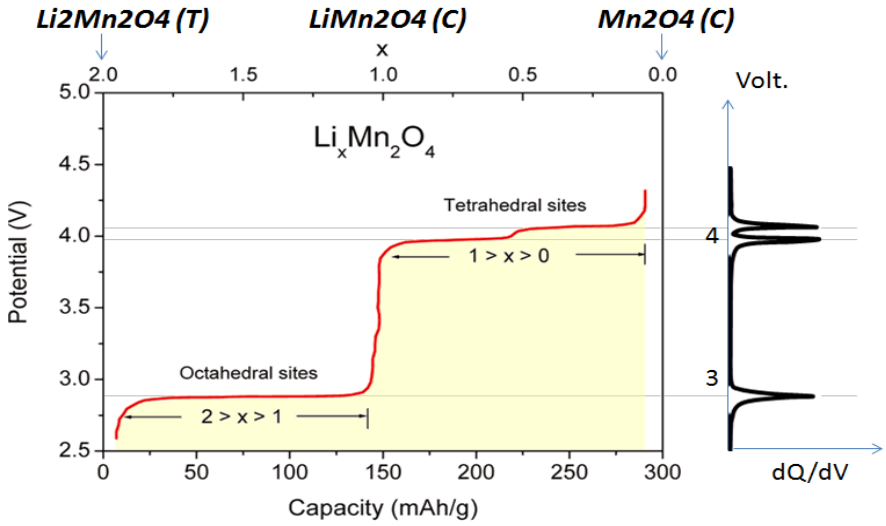

Figure 1.17 The voltage profile of $Li_xMn_2O_4$ crystals as a function of lithium composition (top of Figure) and capacity (bottom of Figure). The corresponding differential capacity profile is shown in right-side. [6]

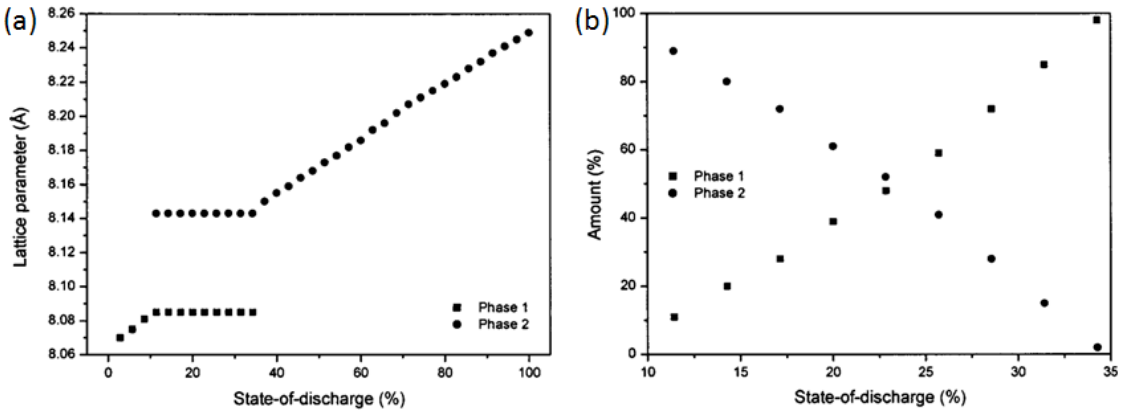

Figure 1.18 (a) Changes in $Li_xMn_2O_4$ cell parameter as a function of lithium composition, x during *in-situ* XRD measurement under the discharge rate of C/10. (b) Amount of each phase in the two-phase region of (a). [59]

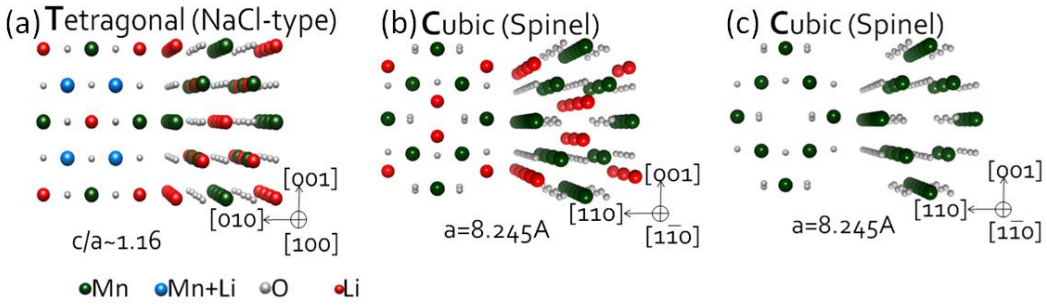

Figure 1.19 The atomic structure of $Li_xMn_2O_4$ crystals (0<x<2). (a) x~2, (b) x=1, and (c) x~0

The $Li_xMn_2O_4$ crystals (x~2) have tetragonal phase shown in Figure 1.17 (a), where lithium ions occupy 16c sites instead of 8a site [58]. Due to the lithium composition, x=2, the valance of manganese ion is +3, and it induces the Jahn-Teller effect. The Jahn-Teller effect is due to the characteristic of electron structure of a manganese ion. The transition metals have the degenerated d electron orbitals: e_g orbital and t_{2g} orbital. When the valance of a manganese ion is +3, three electrons occupy t_{2g} orbital and one electron occupys e_g orbital. By geometrical distortion of the lattice, the degeneracy is removed and the overall energy can be lowered. (This distortion is called as 'Jahn-Teller distortion'.) Thus, when the valance of a manganese ion is +3, the cubic phase changes into tetragonal phase due to the Jahn-Teller distortion. However, when a manganese ion has the valance of +4, the Jahn-Teller distortion does not occur because of no electron in e_g orbital. The schematic of the Jahn-Teller effect is shown in Figure 1.20. The left state of Figure 1.20 [68] is the degenerated orbital, and the middle one is the state after lattice distortion.

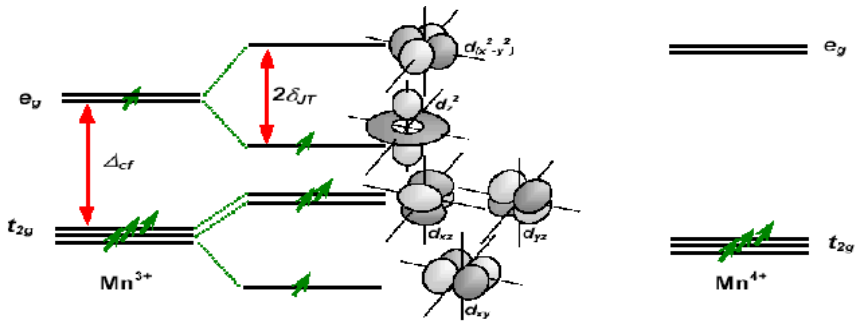

Figure 1.20 The schematic of the Jahn-Teller effect. The left state is the degenerated electron state of a Mn^{3+} ion, the middle one is the state of distorted lattice due to the Jahn-Teller effect. The righ state is the degenerated electron state of a Mn^{4+} ion.

1.2.3 Aging issue of $LiMn_2O_4$ crystals at the 4V range

The capacity fade of the aged $LiMn_2O_4$ crystals is the most serious issue to be solved. A lot of researches have been investigated to clarify the reasons for the capacity fade. The reported reasons are as follow:

(1) Inset of the Jahn-Teller effect [36,38]: the tetragonal phases due to the Jahn-Teller distortion was found at the surface of the $LiMn_2O_4$ crystals discharged above 3.3 V vs Li/Li^+. Since the tetragonal phase has large lattice mismatch with cubic phase (~6 %vol change), it has been pointed out to cause the physical fracture.

(2) Mn dissolution [53,69]: 2 Mn^{3+} ions can be changed into Mn^{2+} + Mn^{4+}. Mn^{2+} is dissolvable in electrolyte. As Mn ions are dissolved, the capacity of cathode materials becomes faded out. Also, dissolved Mn ions diffuse to carbon composite anode and make the carbon anode degraded.

(3) Phase transformation [54,70]: Since the charge/discharge reaction at the 4V range is the two-phase reaction (first ordered phase transition), the lattice mismatch appears between the two phases – $Li_xMn_2O_4$ (x~0) and $Li_{0.5}Mn_2O_4$. It gives the strain field and help to physical fracture.

(4) Instability of high charged phase [71, 72]: the Li-poor, high charged $Li_xMn_2O_4$ (x~0, or λ-MnO_2) is unstable, esp. above 55 ℃. It can be decomposed into MnO_2 and Mn_2O_3. During the decomposition process, Mn^{2+} ions appear and dissolved in electrolyte.

Such reasons for capacity fade out have been proposed with various methodologies. However, the real time behavior of the lithium diffusion and phase transformation which cause the capacity fade has not been uncovered. It is necessary to reveal the dynamic aging behavior of $LiMn_2O_4$ cathode materials due to the lithium diffusion for improving the aging effect.

1.3 Purpose

For understanding the mechanism of the capacity fade, the local structure change caused by lithium diffusion behavior is required to be revealed, namely, observed by TEM. In this study, the issue is to observe the lithium diffusion behavior and the local structure change of $LiMn_2O_4$ cathode materials in real time, and to obtain the electrochemical properties simultaneously during *in-situ* TEM observation: A set of the TEM images which reflect structure change and the simultaneously obtained electrochemical properties has never been reported yet.

As a strategy for *in-situ* TEM observation, lithium imaging method, ABF imaging was investigated. Because ABF imaging is a powerful tool to visualize lithium ions at an atomic scale in real space. Second, we developed *in-situ* observation system which can obtain the electrochemical properties of pA-order current. Third, we fabricated the 'nano-battery' for *in-situ* observation. Finally, we performed *in-situ* TEM observation to clarify the lithium diffusion behavior and the local structure change in $LiMn_2O_4$ crystal.

These obtained results are expected to contribute to design the better spinel system cathode materials by feedback (Figure 1.21).

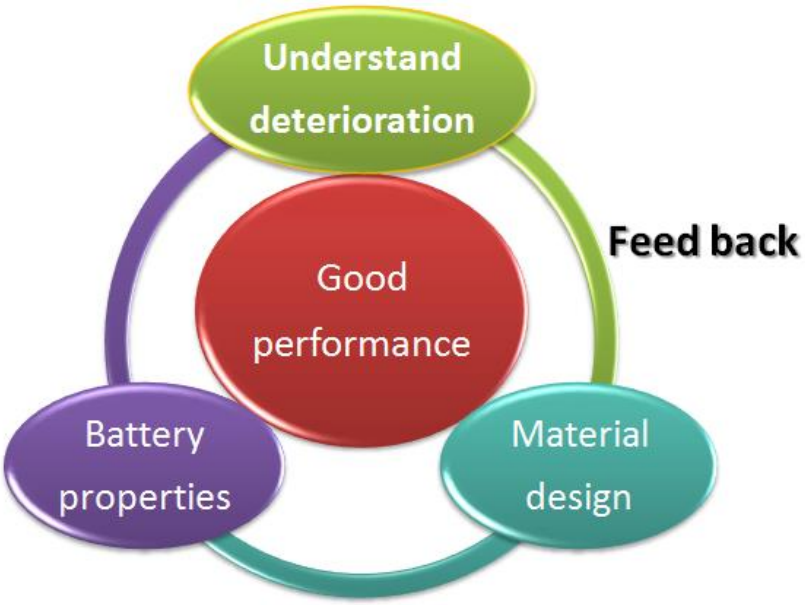

Figure 1.21 The relationship between understanding the aging (deterioration) mechanism investigated in this study and the goal to obtain good battery performance.

Chapter 2. Electron microscopy for LIBs' materials

2.1 Introduction – Electron microscopy for LIB.

Since the lithium diffusion from anode to cathode gives the electricity of LIB, how lithium ions diffuse and what hinders the lithium diffusion is the important issue to improve the battery performance. The monitoring of the lithium diffusion has been performed by electrochemical technique such cyclic voltammetry (CV), constant current cycling and impedance spectroscopy. These techniques give the information from the whole parts of a battery and useful to understand the mean reaction in the battery. However, for understanding of the lithium diffusion at a micro scale, the tool providing the information from local area is needed. TEM is one of the most powerful techniques, directly visualizing the local structure. TEM imaging is expected to visualize the lithium diffusion behavior in the electrode materials and in the interface area of electrode and electrolyte by *in-situ*.

Recently, annular bright field (ABF) imaging in scanning transmission electron microscopy (STEM) has directly visualized the lithium atomic columns in cathode materials such LiV_2O_4 [73], $LiMn_2O_4$ [74], $LiCoO_2$ [75] and $LiFePO_4$ [76]. The ABF imaging mechanism has been studied with thick specimen [77,78], However, the imaging mechanism of ABF image is still not fully understood.

In this study, we investigated the ABF imaging mechanism for using *in-situ* observation and concluded that single lithium ion movement can be visualized during charge/discharge process.

In section 2.2, simple introduction of aberration corrected electron microscope, R005, we used is given, and in section 2.3, simple introduction of TEM image contrast we used during *in-situ* observation. In section 2.4, the imaging mechanism of the ABF image investigated in this study is given.

2.2 Aberration corrected electron microscope, R005

Aberration corrected electron microscope, R005 was used in this study. Figure 2.1(a) shows the appearance of R005 microscope. The R005 microscope is equipped with double aberration correctors, one for STEM imaging and the other for TEM imaging, which cancel the positive spherical aberration of object lens by applying negative spherical aberration [79-81]. The electron gun is cold field emission gun (CFEG), which give narrow energy deviation, 0.3~0.5 eV at the acceleration voltage of 300 kV. The chromatic aberration coefficient, Cc, is 1.65 mm. With the support from the equipments-Cs corrector, CFEG, and so on, the 47pm-resolution was achieved [82].

R005 is equipped with HAADF detector, ABF detector and EELS detector for imaging and analyzing. So, three kinds of images (information) can be obtained simultaneously. (The detector angle of ABF imaging is 1/2α~α, α is the convergent angle of the incident beam.) The brief ray path and detector position for STEM imaging is shown in Figure 2.1(b).

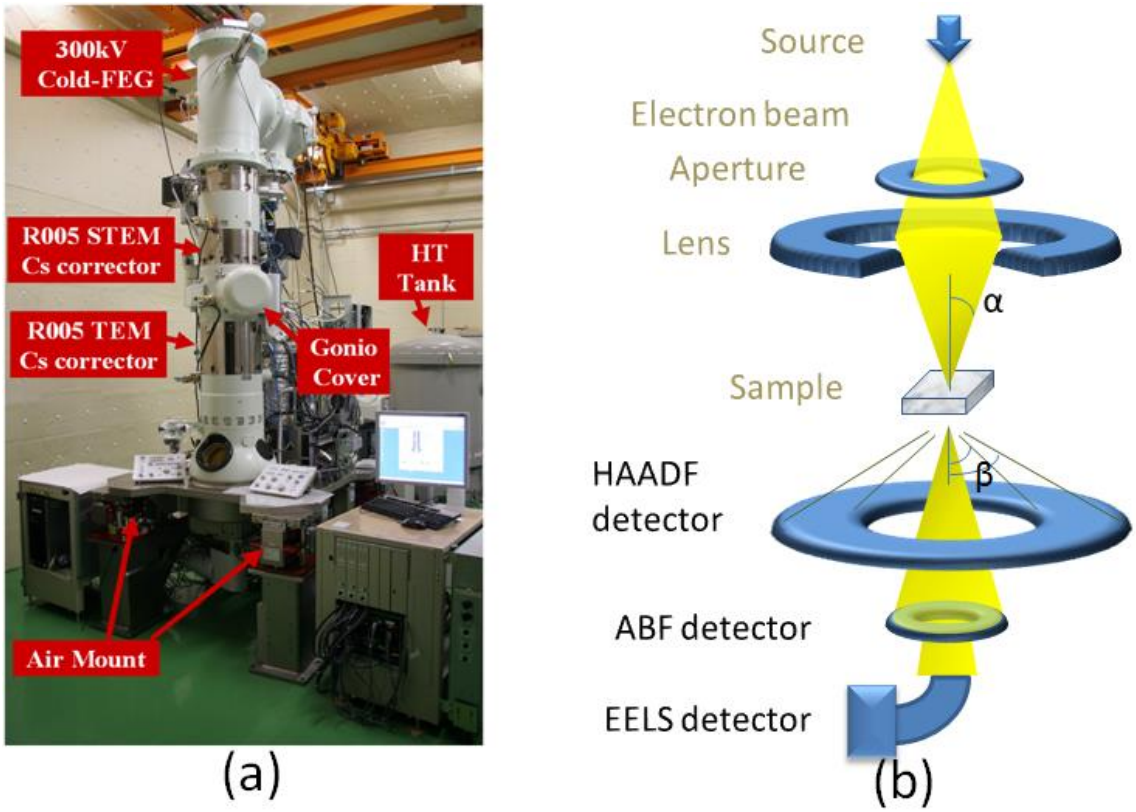

Figure 2.1 (a) The appearance of aberration corrected electron microscope, R005. (b) Brief ray path and detector position for STEM imaging.

2.3 TEM imaging [83]

Conventional TEM imaging visualizes the micro-structure of the materials (object) with the image contrast. The image contrast in TEM image originates from the transmission function of the object and the transfer function of the lens (mainly object lens), because the electron wave passed the materials is modified by the transfer function of the lens. The image contrast of TEM image can be written as follow:

$I(x) = |\psi(x)|^2$, $\psi(x) = q(x) \otimes t(s)$, $t(x) = FT\{T(u)\}$

Where, I(x) is the image contrast as a function of position, x, ψ(x) is the wave function of electron magnified by lens, q(x) is the transmission function of the object observed, T(u) is the lens transfer function, ⊗ is the convolution operator and FT is the Fourier transform.

The transmission function, q(x) is a function of the potential distribution inside the object, which changes the phase and the amplitude of the transmitted electron wave. If the thickness of the object is thick enough, the image contrast is mainly contributed by the modification of the amplitude of the incident electron wave (amplitude contrast). In other hands, if the thickness is thin enough, the amplitude of electron wave is almost retained. Instead, the image contrast is contributed by the modification of the phase of the incident electron wave (phase contrast).

The transmission function of the object can be written as follow:

$q(x) = \exp i\sigma\{V(x)+U(x)\}$

where V(x) is the phase changing component of the potential, U(x) is the amplitude changing component of the potential and σ is the interaction constant, $\sigma = 2me\lambda/h^2$. If the thickness of the object is thin enough ($V(x)<<1, U(x)\sim0$), the potential inside the objected can be approximated as the potential projected along the incident direction of the electron wave, projected potential, φ(x).

$V(x) \sim \int(\text{potential})dz = \varphi(x)$

$q(x) \sim \exp\{i\sigma\varphi(x)\} \sim 1 - i\sigma\varphi(x)$: weak phase object approximation (WPOA)

The transmitted electron wave can be focused by using object lens. At the focal plane of the object lens, the wave is diffracted: strengthen each other and cancel each other depending on the diffracted angle (k position in reciprocal space). The diffracted wave makes diffraction pattern due to the periodicity (symmetry) of the atomic array in the object. The TEM image contrast consists of each diffracted wave. If one diffracted wave is interrupted by beam cutter such as an aperture, the contribution of that diffracted wave is cut and the image intensity (brightness) decrease at the area which have the lattice plane diffracting the cut wave (diffraction contrast). It is the principle of the bright field image and dark field image.

The transmitted electron wave is modified by the transfer function of the object lens which

magnifies the transmitted electron wave at the first. The transfer function can be written briefly as follow:

$T(u) = A(u)\exp\{i\chi(u)\}$

Where A(u) is the aperture function and $\chi(u)$ is the aberration function:

$A(u) = 0$ for $u > u_0$, 1 for $u < u_0$ (u_0 is the size of the aperture or the lens)

$\chi(u) = \pi f\lambda u^2 + \pi Cs\lambda^3 u^4/2$

Where f is the defocus and Cs is the spherical aberration coefficient, $|u| = 2\sin(\alpha/2)/\lambda$ and α is the scattering angle. The transfer function is the function of the aberration function which is the function of the defocus. Thus, the transfer function can be changed by the defocus. If the object is thin enough to satisfy the WPOA, the TEM intensity change from bright contrast to dark contrast as the sign of the defocus change.

2.4 ABF-STEM imaging for visualizing Lithium

ABF-STEM imaging has directly visualized the lithium atomic columns in cathode materials of LIBs. However, the imaging mechanism of ABF image is still not uncovered completely. Thus, we investigated the dependence of ABF image on thickness, defocus and convergent angle. In this study, we found that the ABF image contrast of an atomic column varied with the proportional relationship with the sample thickness, the number of ions in an atomic column. The ABF image gives an atomic column reversible contrast as the sign of defocus changes: dark contrast with overfocus, bright contrast with underfocus. These results are the evidence of the phase contrast, in which the potential change can be visible as contrast change. The visualization of lithium movement in cathode materials was demonstrated by *in-situ* ABF imaging during the phase transformation. In addition, the visualization of the ion vacancy at the surface of a cathode material by large convergent angle ABF imaging was discussed with the theoretical calculation.

2.4.1 Detection of Li movement at atomic level

2.4.1.1 Counting ions – thickness dependence

In our previous work [84] (the work of master degree), it was found that the number of lithium atoms was countable in the individual diffusion channels of the LiV_2O_4 spinel structure. In the ABF imaging of STEM, the contrast of the lithium column intensity varied by a step of single lithium atoms in correlation with the thickness change of the very thin LiV_2O_4 crystal as shown in Figure 2.2. The experimentally obtained result was in accordance with theoretical simulations. This proportional relationship suggests that using ABF imaging, dynamic behavior of lithium atoms in the thin cathode material could be detected at the atomic scale with the intensity change of lithium atomic column.

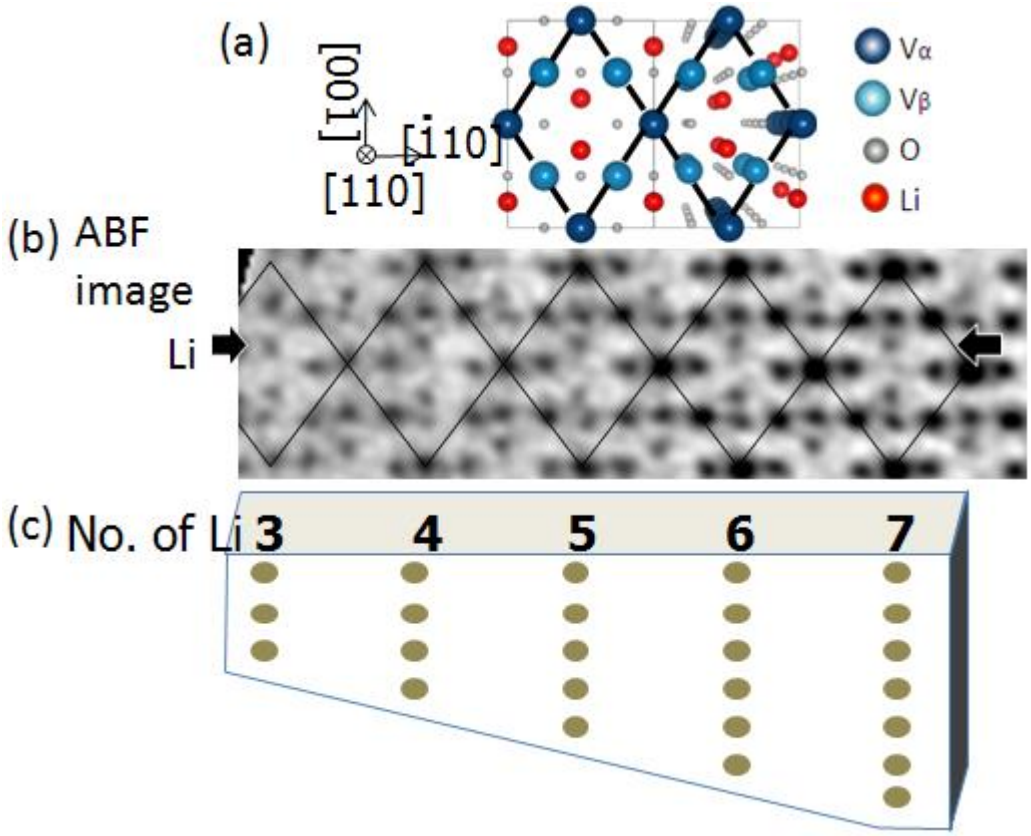

Figure 2.2 (a) An atomic model of LiV_2O_4 crystals viewed from the [110] direction. The rhombic unit cell is indicated by bold black line. Dark blue spheres indicate the vanadium α column (Vα); blue, the vanadium β column (Vβ); gray, oxygen; and red, lithium. The crystal has a period of 0.583 nm along the <110> directions. The crystal structure is schematically depicted by a projection (left-side half) and in perspective (right-side half) to better illustrate the number of atoms in each atomic column. The number of vanadium atoms at the Vα sites is twice as many as those at the Vβ sites. (b) A typical ABF image of a wedge shape LiV_2O_4 crystal showing linear relationship between the ABF intensity and the number of lithium atoms shown in (c). Two black arrows connect the upper lithium columns in each rhombic unit. The image contrast of each column was enhanced by nonlinear scale.

2.4.1.2 Phase contrast – defocus dependence

The relationship between the ABF image contrast and the defocus gives the contribution of phase contrast in the ABF image and helps to understand the image mechanism of ABF imaging. For clarifying the relationship, we used the nanowire, whose thickness change is constant. Figure 2.3(a) illustrates the morphology of the observed $LiMn_2O_4$ nanowire. The nanowire has the [001] axis and {110} lateral surfaces truncated by {100} surfaces. The morphology was derived by ABF images observed with the electron probe propagating along the [100] direction. Figure 2.3(b) shows the geometry of atomic columns of the $LiMn_2O_4$ nanowire observed, and Figure 2.3(c) shows a typical ABF image. In Figure 2.3(b), the column indicated by red dots consists of one lithium ion per unit length (=0.825 nm) along the [100] direction. While the column indicated by green dot consists of one manganese and two oxygen ions per unit length (called as Mn-O column hereafter). The unit cell is shown by a square in Figure 2.3(b) and 2.3(c), where Mn-O columns locate at the corner of the unit cell. In the unit cell in Fig. 2.3(c), the Mn-O columns show darker contrast. The four Mn-O columns aligned along the perpendicular direction of the nanowire axis had increasing number of Mn ions of 4, 4, 5 and 5, respectively: the number increases one-by-one for each two columns. The number of manganese ions was determined from quantitative analysis of the image intensity of the column (Figure 2.4), which is proportional to the dip-height of the Mn-O columns [84].

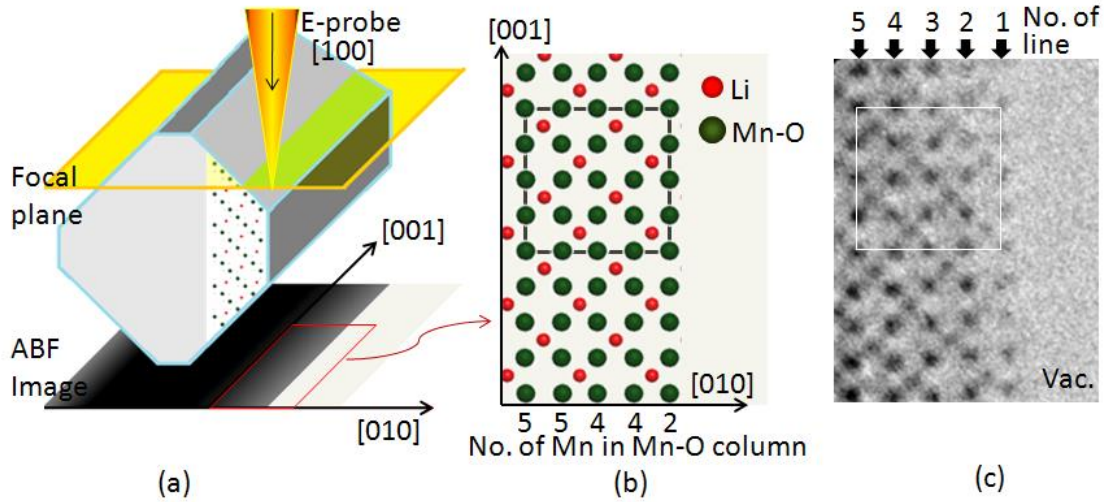

Figure 2.3 (a) Schematic illustration of a $LiMn_2O_4$ nanowire with a truncated-square cross-section. View from the [100] direction. The yellow sheet corresponds to the focal plane. (b) Projection of atomic columns of the spinel $LiMn_2O_4$ structure: Green dots are Mn–O columns and red dots are Li columns. The bold rectangle shows the unit cell size of 0.825x0.825 nm2 in the (001) plane. (c) Typical ABF image of a $LiMn_2O_4$ nanowire.

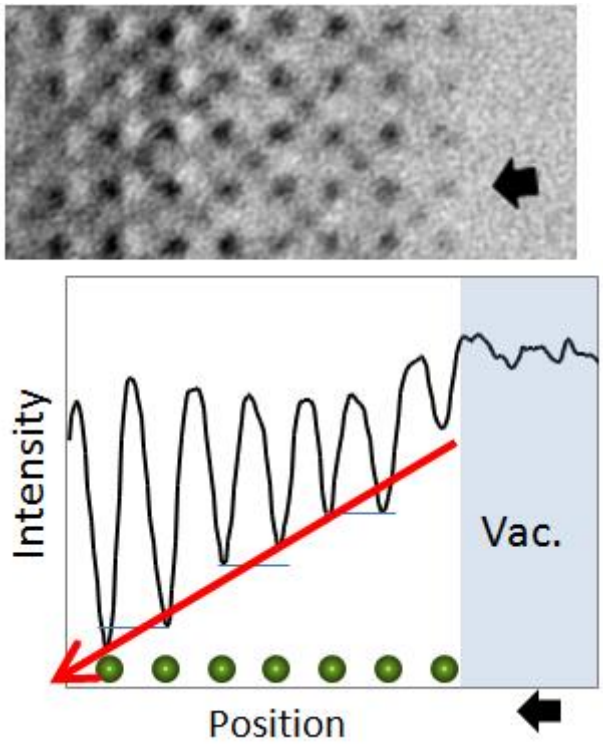

Figure 2.4 (upper) The ABF image of the nanowire edge observed. (bottom) The image intensity corresponding the line indicated by the black arrow in the upper ABF image. The position of dips in the profile corresponds to the position of the Mn-O columns. The dip-height of the Mn-O columns changes monotonously with the step for every two columns.

Figure 2.5 shows through-focus series of ABF and HAADF images for the $LiMn_2O_4$ nanowire. Both ABF and HAADF images were observed simultaneously at the convergent angle of 30 mrad (Figure 2.5(a) and (b)). The focal plane of the electron probe was changed by a step of 2 nm in a range from +10 (over-focus) to -10 nm (under-focus). The ABF images in Figure 2.5(a) show reversible column contrast by the change of defocus sign: atomic columns show dark dips at the over-focus regime, while they, bright peaks at the under-focus one. The dark dip in ABF image observed at the defocus of +2 nm gave the highest contrast. The unit cell area is marked by a square in the Figure. The contrast corresponds to the position of atomic columns and no artificial contrast appears in the ABF image. The optimum-defocus which gives the maximum contrast is about + 2 nm. The HAADF images in Figure 2.5(b) showed bright column contrast regardless of the defocus. The maximum contrast is obtained at the defocus of about -2 nm.

More quantitatively, the visibility of the Mn-O atomic column was measured as follow,

$$Visibility = -\left(\frac{I_c - I_{bg}}{I_c + I_{bg}}\right) \quad \text{for ABF images}$$

and

$$Visibility = \frac{I_c - I_{bg}}{I_c + I_{bg}} \quad \text{for HAADF images,}$$

Where I_c and I_{bg} are the image intensities of a column and background, respectively (Figure 2.7d). The visibility of ABF image becomes positive when a column appears with dark contrast. Figure 2.6 summarizes the defocus dependence of visibility at the Mn-O atomic columns in Figure 2.5. The plots marked by diamond, square, triangle and cross are, respectively, the visibilities of the Mn-O columns in the 2^{nd}, 3^{rd}, 4^{th}, and 5^{th} columns from the edge of the nanowire (Figure 2.3c). In these plots, the defocus difference due to the inclination of the top surface from the focal plane was included. These plots show similar defocus dependence of visibility for the 2^{nd} – 5^{th} columns, although they have different thickness. The visibility of ABF images shows maximum (about 0.8) at +2 nm, and negative values at under-focus regime. On the other hands, the visibility of HAADF images shows maximum (about 0.2) at -2 nm. The optimum defocus values of ABF and HAADF images were the same value, but different sign.

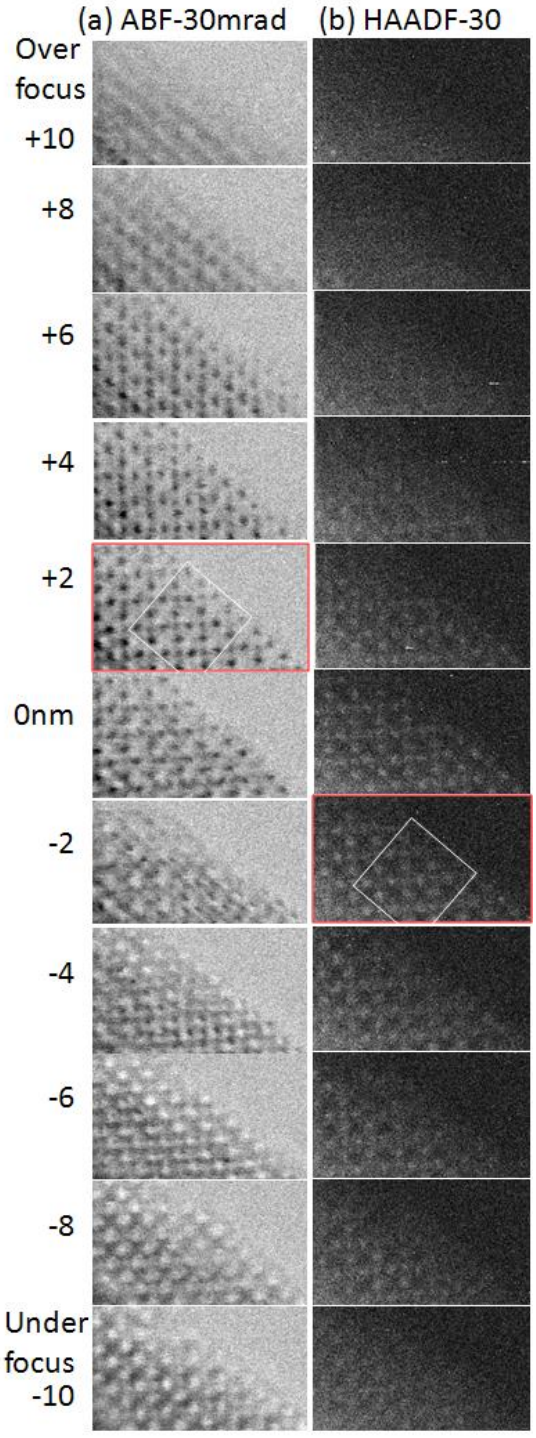

Figure 2.5 Through-focus (a) ABF and (b) HAADF images for convergent angles of 30 mrad. A white square in each focus series shows the unit cell of the spinel $LiMn_2O_4$ (see Fig. 1(b)). The images marked by red rectangles were obtained at the optimum defocus. At positive defocus, the focal plane of the probe is above the specimen surface.

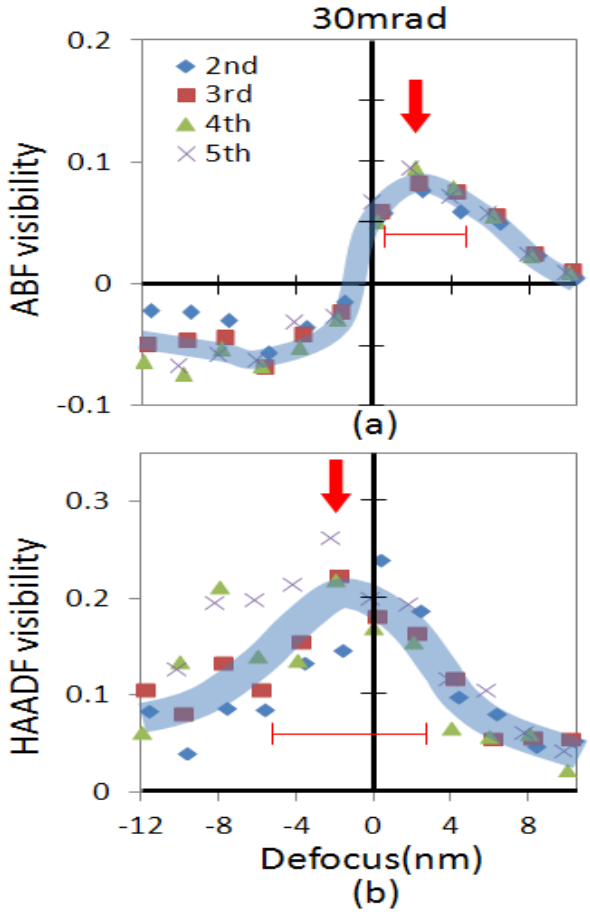

Figure 2.6 The defocus dependence of the visibility of Mn–O columns. (a) ABF and (b) HAADF for a convergent angle of 30mrad. The plots show the visibility of the Mn–O columns in the 2nd–5th rows running parallel to the truncated edge of the $LiMn_2O_4$ nanowire. The blue curves show the defocus dependence. The optimum defocus is shown by a red arrow, and the depth of focus is shown by a red bar.

Figures 2.7(a) and (b) show the experimental ABF images of the $LiMn_2O_4$ nanowire at +2 and -6 nm in defocus, respectively. Figure 2.7(c) shows the intensity profiles along the lines indicated by an arrow in both Figure 2.7(a) and (b). Both intensity profiles are found to reverse in reference to the mean intensity, I_m. The reversal of contrast indicates that the ABF image is contributed by phase contrast.

The mean intensity was obtained by averaging the image intensity at the same thickness region in Figure 2.7. It increases monotonously as the specimen thickness decreases regardless defocus change (From left-side to right-side). It crosses the vacuum intensity, I_{vac} in vacuum region at a distance from the edge, since the specimen edge is truncated. Therefore, mean intensity reflects effective absorption of electrons by the specimen, electrons scattered out of the ABF detector.

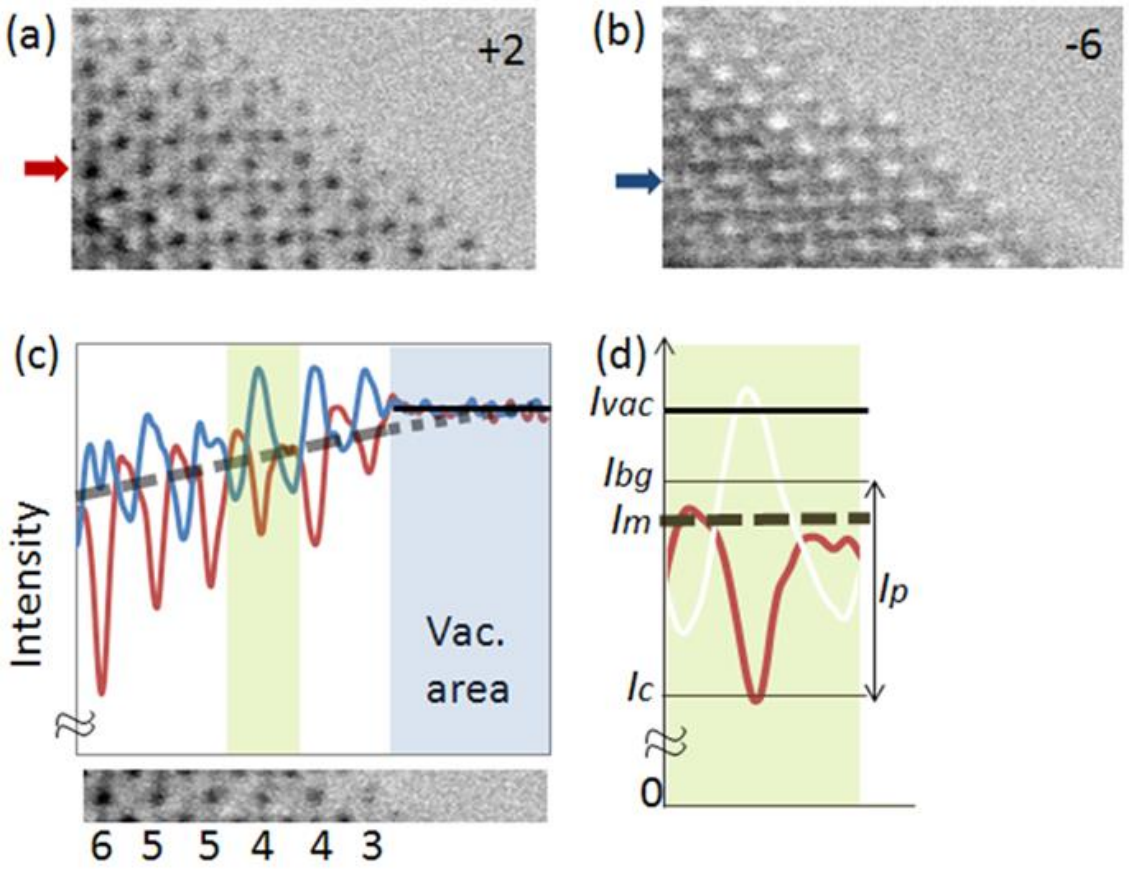

Figure 2.7 ABF image of $LiMn_2O_4$ nanowire. (a) over focus image (+2 nm) and (b) under focus image (-6 nm). (c) Intensity profile of Mn–O columns along the [110] direction. The red curve is for (a) and the blue curve is for (b). The dashed line is the mean intensity (I_m). (d) Intensity profile and definition of mean intensity (I_m), vacuum intensity (I_{vac}), column intensity (I_c), background intensity (I_{bg}), and peak intensity (height) (I_p): $I_c=I_{bg}+I_p$.

The annular detector placed within the bright field region must contribute to improvement of spatial and depth resolution [85]. From Cowley's formulation of interpreting quantitative STEM image (Eq. (11) in ref. 85), the column intensity in the bright field image is expressed by (the second order term of φ(x) is neglected)

$$I_c(x) = I_{vac} - p(x) \otimes \left\{ t(x) \int du D(u) T^*(u) \exp[-2\pi i u x] \right\} - \text{complex\_conjugate}$$

$$p(x) = i\sigma\varphi(x)$$

$$t(x) = F[T(u)]$$

Where φ(x) is a projected potential, σ, the interaction constant ($2me\lambda/h^2$), T(u), transfer function of the probe forming lens and D(u), a detector function. The image contrast is determined by the

convolution of the projected potential and the "effective" probe function, ξ(x) given by

$$\xi(x) = t(x)\int du D(u) T^{*}(u) \exp(-2\pi u x) = \xi_r(x) + i\xi_i(x).$$

Therefore, the reversible contrast of ABF image is expressed by the term,

$$I(x) = +2\varphi(x) \otimes \xi_i(x)$$

Under the same condition with the experiments, the effective probe function, ξ(x), was calculated as shown in Figure 2.8. The sign of ξ(x) is changed from positive to negative defocus, in accordance with the contrast reversal of the observation. Contrast reversal by defocus is well known in conventional TEM images. In ABF images, but, no artificial contrast appears in contrast with TEM images. Therefore, the ABF images of thin specimens are given by the projected potential, "structure image", irrespective to the focus condition. And the ABF image is expected to directly visualize the local potential change due to lithium ion movement.

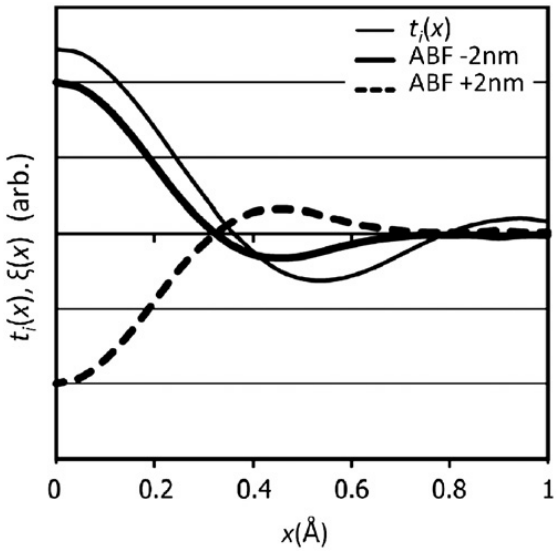

Figure 2.8 Imaginary part of the effective probe function, $\xi_i(x)$ and probe function, t(x).

2.4.2 Demonstration of Li movement imaging

In the previous section, we investigated the ABF image mechanism and concluded that the potential change due to lithium ion movement can be visualized. In this section, we performed *in-situ* ABF imaging of electron beam induced LiV_2O_4 structure change to demonstrate the ability of ABF imaging of visualization of the potential change in Li columns. We used the convergent angle of 24 mrad.

Figure 2.9(a) depicts the spinel LiV_2O_4 crystal viewed from the [110] direction. In this view, there are two kinds of vanadium atomic columns on the sides of the rhombic unit (indicated by the bold line): Vα and Vβ columns. Lithium columns are located on the diagonal of the rhombic unit, between the oxygen columns. The Vα column consists of 16d octahedral sites, while the Vβ column consists of alternating 16c and 16d sites. Since 16c sites are empty, the number density of occupied sites in the Vβ column is half that of the Vα column. Lithium ions occupy 8a tetrahedral sites. The lithium column has the same number density as the Vβ column. The pair of lithium columns along the [110] direction forms a diffusion channel for lithium ions in the LiM_2O_4 spinel structure (M: transition metal such as V, Mn, or Ti) [55]

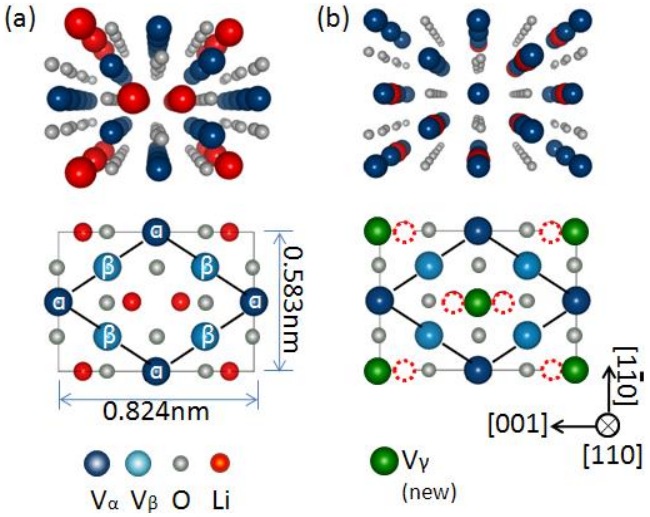

Figure 2.9 (a) Schematic illustration of spinel LiV_2O_4 crystal viewed from the [110] direction. The top image is a perspective view and the bottom image is a top view in which the rhombic unit cell is indicated by the bold black line. Dark blue spheres indicate the vanadium α column (Vα); light blue, the vanadium β column (Vβ); gray, oxygen; and red, lithium. The crystal has a period of 0.583 nm in the {110} and [1-10] directions. (b) Schematic illustration of a defective NaCl structure of $Li_xV_2O_4$ ($0 < x < 1$) viewed from the [110] direction. Dotted circles indicate the positions of lithium columns in the spinel structure, which are vacant in the defective NaCl structure. Dark green spheres indicate the vanadium γ column (Vγ).

Figure 2.9(b) depicts a $Li_xV_2O_4$ ($0 < x < 1$) structure viewed from the [110] direction. It was modeled by experimental images taken after intense electron beam irradiation. The lithium columns in Figure 2.9(a) disappear, while Vγ columns consisting of 16c sites appear. Vanadium ions occupy half of the 16c and 16d octahedral sites, so that the Vα, Vβ, and Vγ columns all have the same number density. For $x = 1$, the model has the same structure as the defective NaCl structure of $MgAl_2O_4$ crystals [86]: Mg and Al ions are uniformly redistributed to 16c and 16d octahedral sites.

In-situ ABF images of structural transformation were observed for a thin LiV_2O_4 specimen. Figure 2.10(a) shows the structural evolution for a single rhombic unit. The specimen thickness was estimated to be 3.2 nm by comparison with simulated images[1]: Vα column has 11 vanadium ions, while lithium column, 5 lithium ions. Dark dots appear at the positions of Vα, Vβ, oxygen, and lithium columns in Figure 2.9(a). Vα columns, which appear at the corner of the rhombic unit, are the darkest, followed by Vβ, oxygen, and lithium columns in order.

The spinel structure is preserved from the first to the fourth image. From the fifth image (after 40 s), the contrast of lithium columns starts to decrease until it almost disappears in the eighth image (after 70 s). Since the dark contrast depends on the number of ions in each column [84], the reduction in the lithium column contrast indicates that the number of lithium ions decreases due to displacement from the 8a tetrahedral sites. Following this displacement of lithium ions, two changes occur in the series of the ABF images. A dark spot begins to appear at the center of the rhombic unit cell (Vγ column) in the fifth image and its dark contrast gradually increases.

In addition, the dark contrast of the Vα columns starts to decrease. The contrast variation for the atomic columns from the first to ninth image is plotted in Figure 2.10(b), where the contrast is defined as described in a previous report [84]. As the contrast of the lithium columns decreases, the contrast of the Vα and Vγ columns simultaneously change. On the other hand, the contrasts of the Vβ and oxygen columns (not shown) did not change much. At the completion of the transformation, Vα, Vβ, and Vγ columns have nearly the same contrast, suggesting that they contain the same number of vanadium ions. Thus, vanadium ions were evenly redistributed at the octahedral sites, which corresponded to a defective NaCl structure.

[1] In the simulated images, the dark contrast of Vβ columns increases linearly up to 5 nm and then fluctuates above 5 nm as well as those of the lithium and oxygen columns. That of Vα column increases linearly up to 2.3 nm and then fluctuates. The contrast ratio of Vα/O is constant (2.8) up to 2.3 nm, and gradually decreases as the thickness increases until 4.1 nm. The contrast ratio of Vα/Vβ columns is also constant (2.0) up to 2.3 nm, and gradually decrease to 1.0 at 4.1 nm. The average thickness was estimated to be 3.2 nm, since the ratio of Vα/O was 1.8 and Vα/Vβ, 1.5.

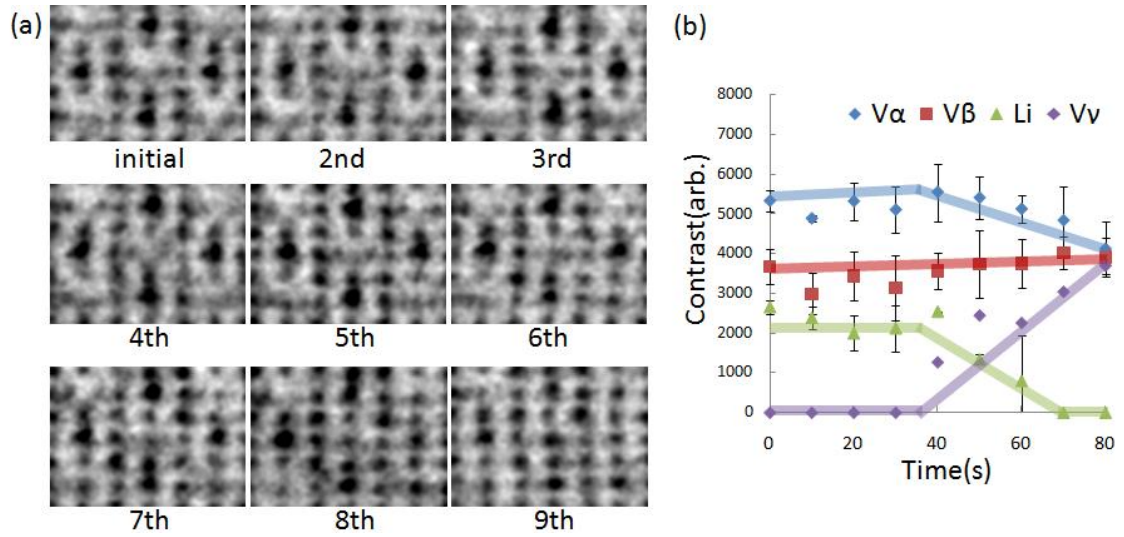

Figure 2.10 (a) A series of *in-situ* ABF images showing structure change from the spinel structure into a defective NaCl structure. The ABF images were obtained in 10 s intervals. (b) Evolution of the contrasts of the Vα, Vβ, Li and Vγ columns in the unit area shown in (a). Dots indicate the average column contrast and the error bars represent the standard deviations of the column contrasts of several equivalent columns in the rhombic unit.

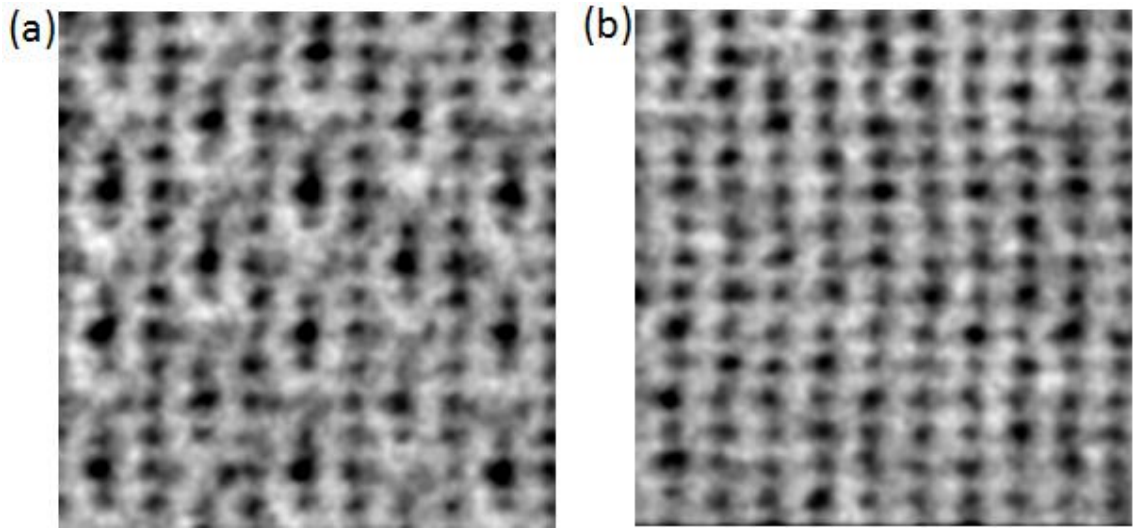

Figure 2.11 (a) ABF image of LiV_2O_4 crystal viewed from the [110] direction at the beginning of electron beam irradiation. The area is 2.06 × 2.19 nm^2. (b) ABF image taken at the same area as that in (a) at the completion of electron beam irradiation.

Similar contrast changes during the structural transformation were observed for every rhombic unit cell (Figure 2.11). Therefore, the spinel structure of LiV_2O_4 crystal was confirmed to be transformed into the defective NaCl structure. No further structural transformation from the defective NaCl structure was observed on further electron beam irradiation. The *in-situ* ABF experiment reveals that vanadium ions rearrange into octahedral sites in response to the displacement of lithium ions from the tetrahedral 8a sites.

Spinel LiV_2O_4 crystals has been reported to nucleate $Li_{0.27}V_2O_4$ crystalline by extracting lithium ions electrochemically. The proposed structure has a layered NaCl structure. Vanadium ions in the spinel structure are redistributed, and occupy the 16c and 16d sites with the ratio of 1:8. Some of one ninth vanadium ions occupy 16c site in Vγ columns in the layered NaCl-structure $Li_{0.27}V_2O_4$ crystalline, the Vγ columns should has less contrast than Vα columns in an ABF image. In the present study, the ABF image of the transformed structure shows same contrast between Vα and Vγ columns (same vanadium ion occupancy in 16c and 16d sites). Therefore the transformed structure was different from the structure of $Li_{0.27}V_2O_4$ crystals.

Lithium ions in the defective NaCl might be deficient because lithium ions has been reported to be ejected from LiC_6 sample by intense electron beam irradiation [87].To determine the number of lithium ions in individual V*i* columns (*i* =α, β or γ), ABF images were simulated for the two extreme cases of zero and six lithium ions in the V*i* columns, since the specimen thickness was 3.2 nm. But, the simulated contrast of the V*i* column was different by only 5 % between them. Taking noise level in the ABF image into account, the number of lithium ions remaining in the V*i* column could not be determined.

In summary, we performed *in-situ* ABF imaging to observe the structural transformation of a spinel LiV_2O_4 crystal induced by intense electron beam irradiation. The spinel structure changed into a defective NaCl structure. We found that the displacement of lithium ions from the tetrahedral sites induced a redistribution of vanadium ions at octahedral sites. *In-situ* ABF imaging is a very powerful technique for visualizing the displacement of light elements in matrices. It provides complementary information to X-ray diffraction [88], neutron diffraction [89], electron diffraction [90], and nuclear magnetic resonance [91] for development of LIB electrodes.

2.4.3 Surface imaging – convergent angle dependence

The surface of cathode materials is the most active area during battery reaction since lithium ions are inserted or extracted through the surface and solid electrolyte interface (SEI) layer is formed at the surface of the cathode materials. Thus to monitor the surface condition is also very important. For visualizing the surface condition such ion defect, we investigated the new method, the ABF imaging with large convergent angle with experiment and theoretical calculation.

First, we investigated the dependence of ABF imaging on the convergent angle. In Figure 2.12, the focal series of ABF images of a spinel $LiMn_2O_4$ crystal viewed from the [100] direction are shown with the simultaneously obtained HAADF images. The images of the same sample were acquired with the convergence angle of 24 mrad and 30 mrad. The optimum focus of the 30 mrad-convergent-angle ABF image is +2 nm while that of 24 mrad one is +4 nm. The optimum focus of larger convergent angle ABF image is closer to the zero focus – the condition that the incident beam is focused to the top surface of the object.

The depth of focus (DOF) also depends on the convergent angle (Figure 2.13). The DOF is defined as the focus range where the visibility was more than 70 % of the maximum value. The ABF images have the DOF of about 4 and 8 nm at the convergent angle of 30 and 24 mrad, respectively. The HAADF images show the DOF of about 8 and 12 nm at the convergent angle of 30 and 24 mrad, respectively. In both ABF and HAADF images, the DOF is narrower at 30 mrad than at 24 mrad. If we assume a relation, $DOF = C \cdot \lambda/\alpha^2$ [92-94], the present results gives C~2.3 for ABF images and C~3.5 for HAADF images. It indicates that the larger convergent-angle ABF image has the narrower DOF and also, ABF images have the narrow DOF than HAADF images.

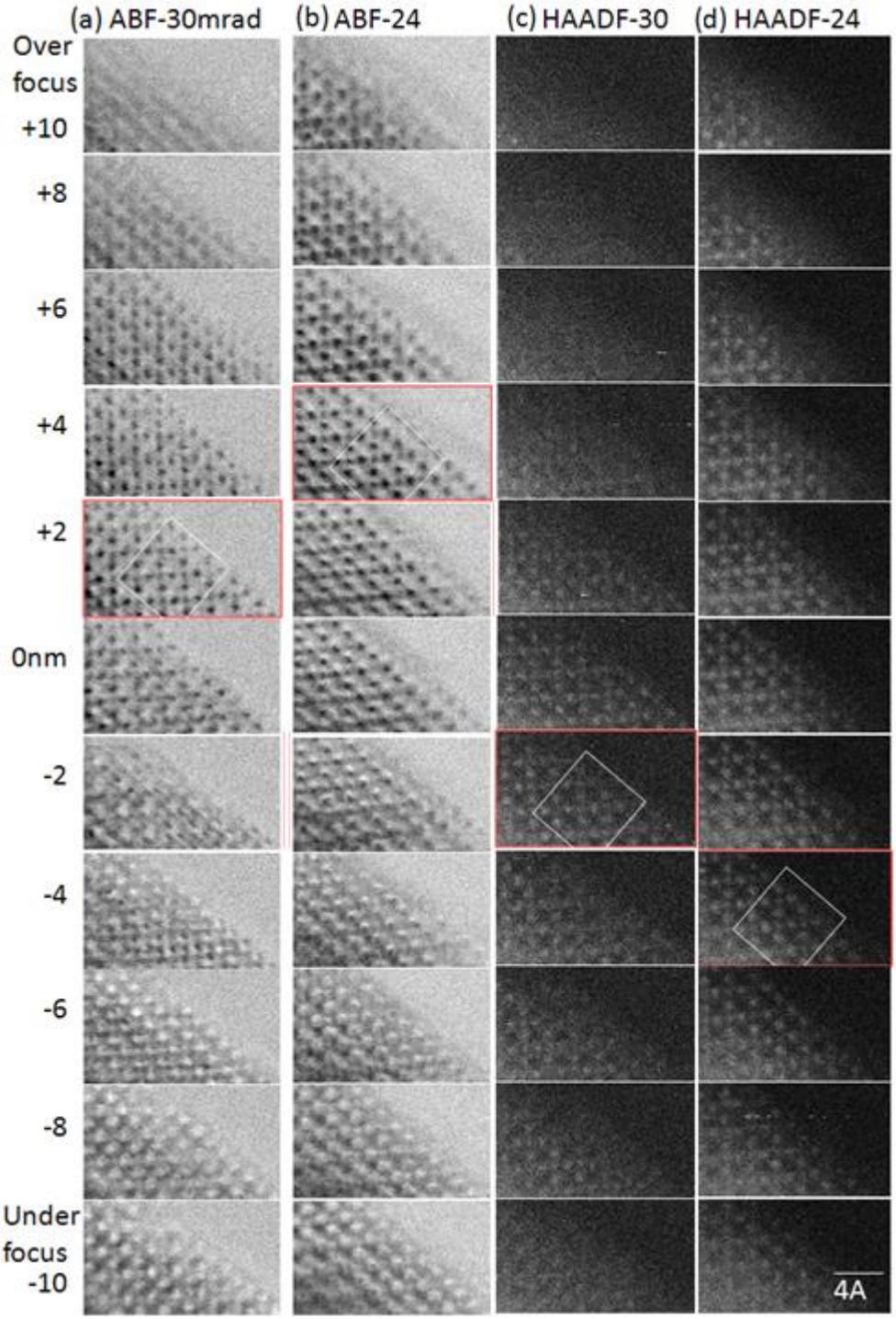

Figure 2.12 Through-focus series of ABF images for convergent angles of (a) 30 mrad, (b) 24 mrad and of simultaneously obtained HAADF images for convergent angles of (c) 30 mrad, (d) 24 mrad. View from the [100] direction. A white square in each focus series shows the unit cell of the spinel $LiMn_2O_4$ (see Figure 2.3(b)). The images marked by red rectangles were obtained at the optimum defocus.

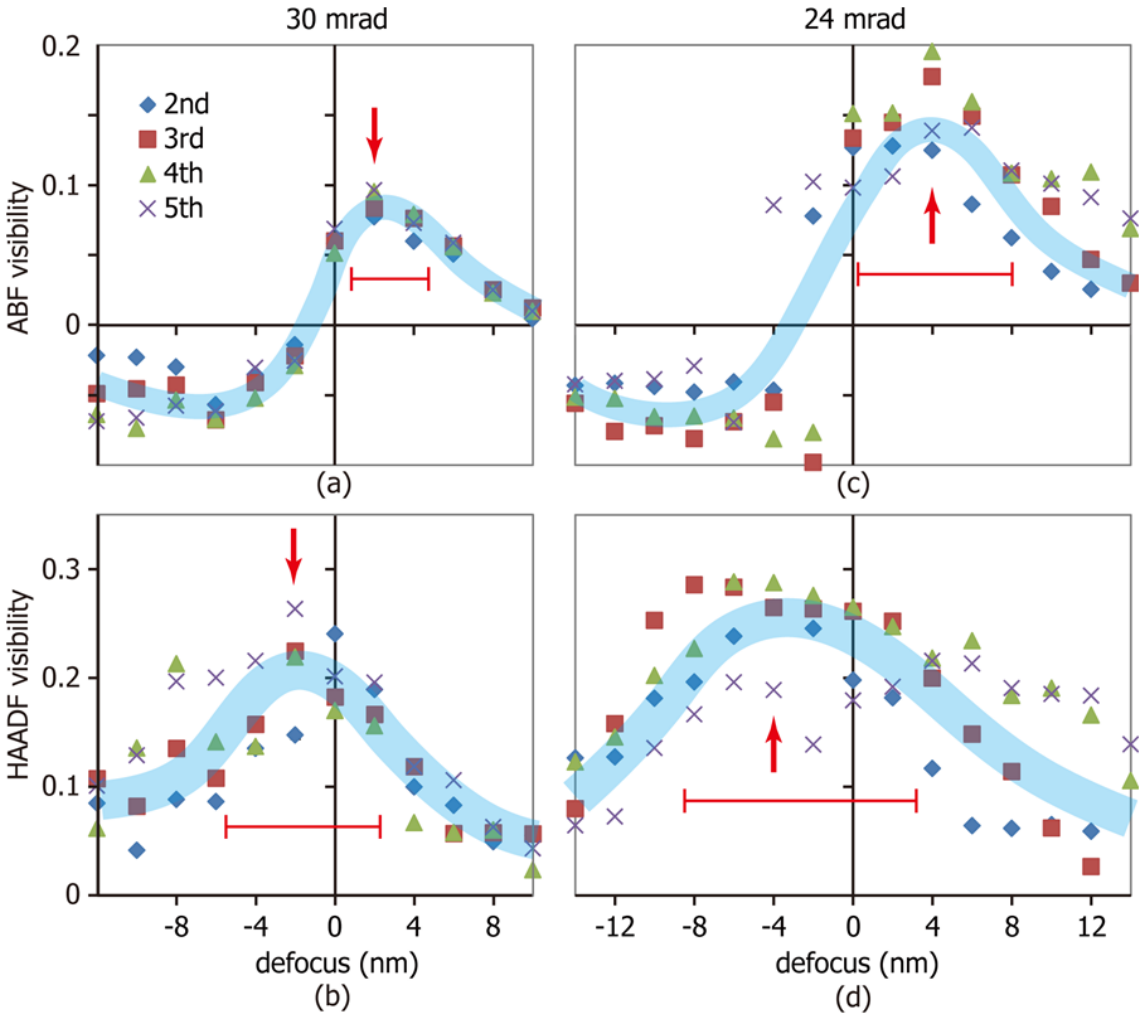

Figure 2.13 The defocus dependence of the visibility of Mn–Ocolumns. (a) ABF and (b) HAADF for a convergent angle of 30 mrad. (c) ABF and (d) HAADF for 24 mrad. The plots show the visibility of the Mn–O columns in the 2^{nd}–5^{th} rows running parallel to the truncated edge of the $LiMn_2O_4$ nanowire. The blue curves show the defocus dependence. The optimum defocus is shown by a red arrow, and the depth of focus is shown by a red bar.

We also investigated the dependence of DOF on the convergent angle from the different crystal orientation, the [110] view direction. Figure 2.14 shows two through-focus series of ABF images observed from the [110] direction with the convergence angle of 24 mrad and 30 mrad. All atomic columns including lithium columns appear as dark dots at over-focus. Mnα columns are positioned at the corner of the rhombic unit marked by black lines in this view direction. As the defocus goes into under-focus, column contrast changes from dark to bright. This reversible contrast is same with the results obtained with the [100] view direction. Also, the ABF images obtained with the convergence angle of 30 mrad shows narrower DOF. The observed DOF values for 24 and 30 mrad are plotted by triangles in Figure 2.15(b) with error bar.

The theoretical calculation of STEM image of a $LiMn_2O_4$ crystal was performed under the same imaging condition with the experiment. The calculation was performed with xHREM program [95] based on Multi-slice method. The detector semi-angle, β, was $\alpha/2 < \beta < \alpha$ (α: the convergence semi-angle of the incident beam). The thermal diffusion scattering absorptive potential approximation was included with Weikenmeier-Kohl scattering factor. The Debye-Waller factors of manganese, oxygen, and lithium were assumed to be 0.84, 1.11, and 1.07 $Å^2$, respectively [96]. The slice thickness was 0.291 nm in the [110] direction. The cut-off scattering vector $\sin\theta_B/\lambda$ was 4.5 A^{-1}, where θ_B is the Bragg-angle and λ is the electron wavelength at 300 keV (λ= 0.00197 nm). The observed images were reproduced after convolving a Gaussian function to the calculated one. Gaussian function with a FWHM=65 pm reproduced the experimental images of 24 mrad, and those of 30 mrad [97]. The Gaussian function, effective source size [97], represents the blur due to residual aberrations, chromatic aberration, statistic noise and instrumental noises.

The simulated images for α=24, 30, 50, and 100 mrad are summarized in Figure 2.15(a). The simulated images of α=24 and 30 mrad reproduce the experimental images, where all atomic columns appear as dark dots at over-focuses. As the convergence angle increases, DOF of ABF images becomes narrower. Then, well-resolved ABF image can be obtained only for the condition that the top surface of specimen is focused. It imposes that the ABF image with a large convergent angle, 50~100 mrad, is sensitive to the top surface profile.

Following the accordance between the experiments and simulations, we calculated the ABF images of a large convergence angle to find imaging conditions for detection of a surface ion vacancy.

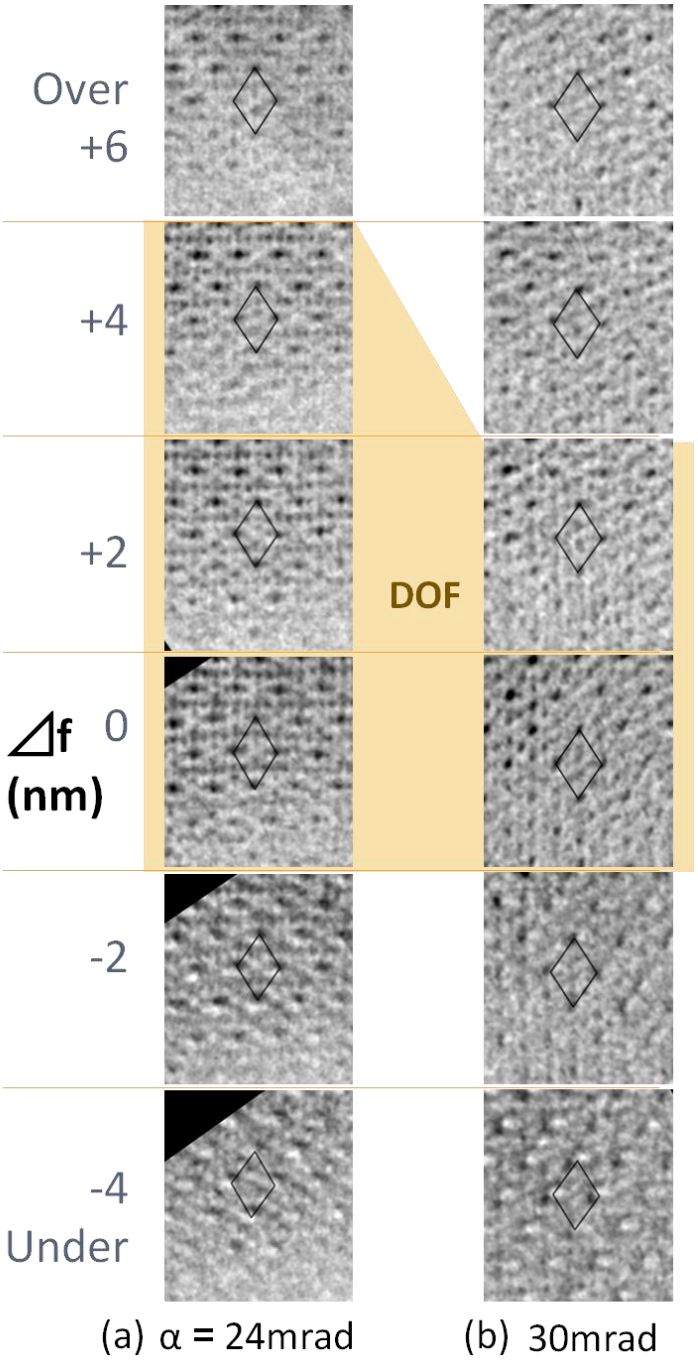

Figure 2.14 Through-focus series of ABF images for convergent angles of (a) 30 mrad, and (b) 24mrad. View from the [110] direction. The rhombic unit of a $LiMn_2O_4$ crystal viewed from the [110] orientation is indicated by black line in the both images. Apparent defocus (Δf) of ABF images are shown: +6 nm (overfocus) to −4 nm (under-focus). The depth of focus (DOF) is 5 nm for (a), and 3 nm for (b).

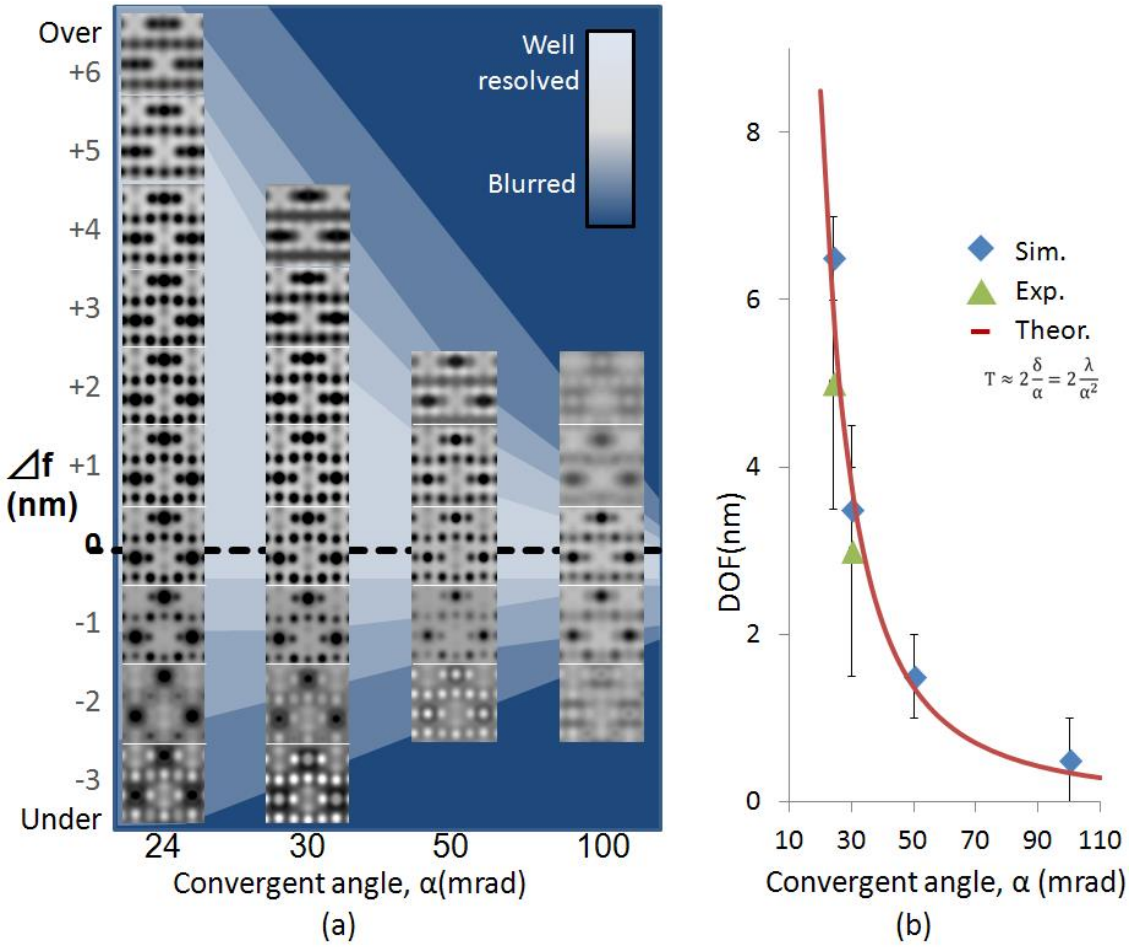

Figure 2.15 (a) Defocus series of simulated image of a $LiMn_2O_4$ crystal for a convergence angle (α) of 24 and 30 mrad. The film thickness is 3 nm. The range of DOF is shown by white region. (b) The plot of DOF as a function of the convergence angle of the incident electron beam.

The ABF images of the model which has ion defect (vacancy) at the top surface were calculated for large convergent angles of 50, 70, and 100 mrad. The defocus value was zero. Figure 2.16 shows simulated the ABF images of manganese columns with and without one vacancy at the top surface. The convergent angle of incident beam was 100 mrad. In Figure 2.16(a), oxygen and Mnβ columns in the rectangled area align alternatively from the left to the right. The second Mnβ column from the left has one vacancy at the top surface. Although the Mnβ columns with and without a vacancy appear dark contrast, the intensity profile shows that one vacancy reduces the column contrast by 25 %.

The simulated image of a 5nm-thick model is shown in Figure 2.16(b). The contrast of Mnβ with a vacancy decreases by roughly 25 % from that without vacancy. For the case of one manganese vacancy positioned at the middle of the column or at the bottom surface, the column

contrast reduced less than 3 %. Thus, one vacancy only at the top surface reduces the column contrast regardless to the film thickness. A smaller convergent angle of 50 mrad gave the contrast decrease by 10 % with the increased DOF, which can also gives the change of ABF image intensity by 10 % due to the existence of vacancy positioned at the middle point of the sample.

Figure 2.17 shows the simulated images of the model with one lithium vacancy in the lithium diffusion channel. The convergent angle of incident beam was 100 mrad. In the area of the red rectangle in Figure 2.17(a), the lithium column at the left side has one lithium vacancy at the top surface. The other lithium column contains no vacancy (four lithium ions within the film thickness of 2nm). The lithium column with a vacancy gives less contrast than the other (without vacancy), as seen in the line profile. One lithium vacancy at the top surface reduced the contrast by roughly 20 %. Contrast decrease is the same amount for a 5nm-thick model (Figure 2.17b). For the case of one lithium vacancy positioned at middle of the column or at the bottom surface, the column contrast was not reduced more than 3 %. Thus, a lithium vacancy at the top surface can be observed with a decreased column contrast. As the convergent angle became small, the contrast of the vacancy at the top surface reduced: 15 % with 70 mrad which could be used to detect lithium vacancy.

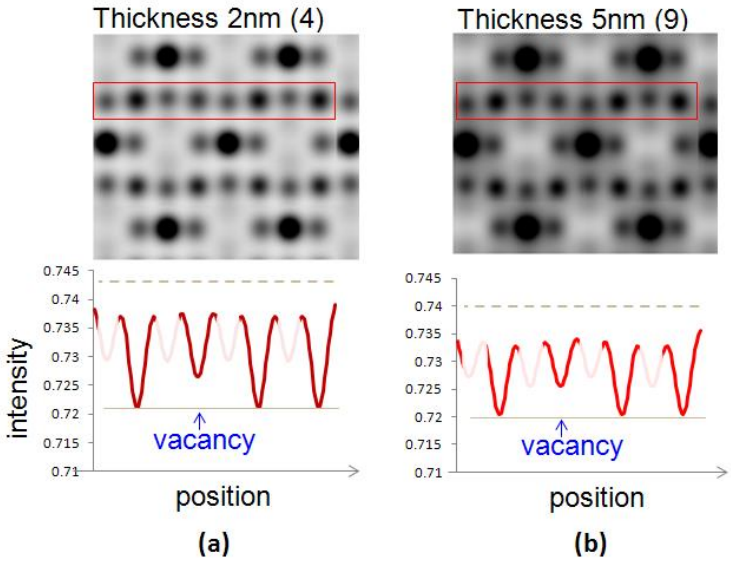

Figure 2.16 Simulated ABF images of one manganese vacancy at the top surface: (a) 2 nm-thick and (b) 5 nm-thick $LiMn_2O_4$ crystal. The convergence semi-angle of the incident beam is 100 mrad. The number in bracket is the number of ions in the Mn column without vacancy for a given film thickness. Intensity profiles show image contrast of oxygen and Mn columns in a red rectangle of each ABF image. Solid horizontal line in the profile is the image intensity of the columns without vacancy and, dashed line is the reference intensity [84]. Intensity profile of oxygen columns is shaded.

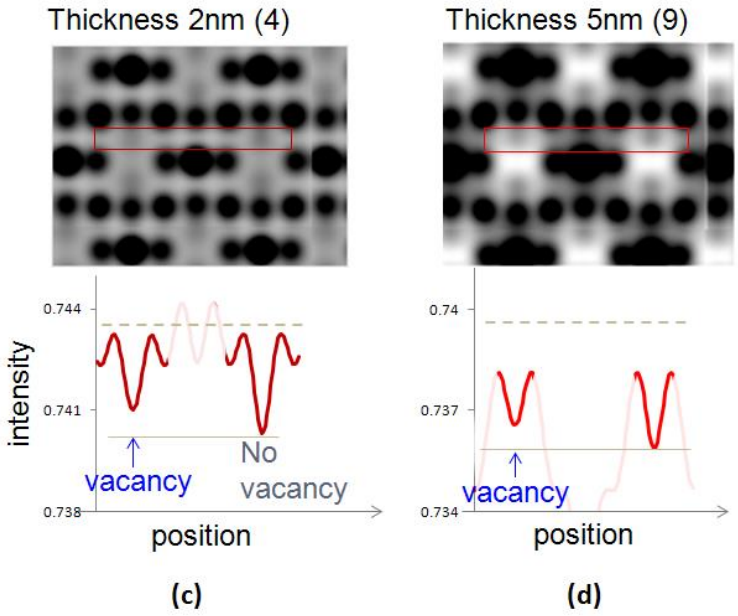

Figure 2.17 Simulated ABF images of one lithium vacancy at the top surface: (a) 2 nm-thick and (b) 5 nm-thick $LiMn_2O_4$ crystal. The convergence semi-angle of the incident beam is 100 mrad. The number in bracket is the number of ions in the lithium column without vacancy for given film thickness. Intensity profiles show image contrast of lithium columns in a red rectangle of each ABF image. Solid horizontal line in the profile is the image intensity of the columns without vacancy and, dashed line is the reference intensity.

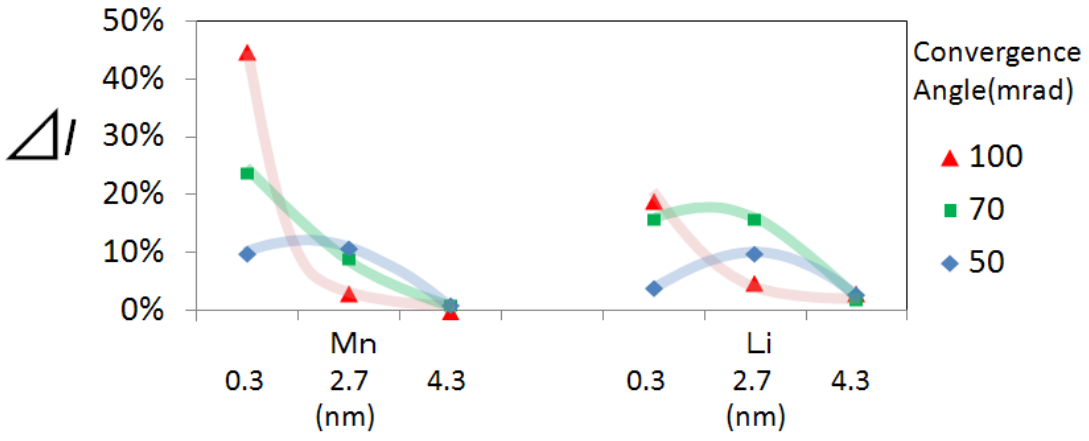

Figure 2.18 The calculated ABF image contrast decrease due to one ion vacancy in 5 nm-thick $LiMn_2O_4$ crystal as a function of the vacancy position from the top surface and the convergent angle.

The contrast decrease of the ABF image due to the ion vacancy as a function of the position of the vacancy and the convergent angle is shown in Figure 2.18. It is clear that the large-convergent-angle ABF image is sensitive to the top surface of the sample: In the 100 mrad-convergent-angle ABF image, manganese vacancy and lithium vacancy can be detected by 45 % and 20 % decreased contrast, respectively. The smaller convergent angle such as 50 mrad shows larger DOF and the deeper position which contributes to the image contrast maximum: the lithium vacancy position at the middle of the sample can be detected by 9 % contrast change which is higher amount than that of the vacancy positioned at the top of specimen.

Surface imaging by ABF imaging with the large convergent angle is promising, although it needs further instrumental development: The convergent angle of 50 mrad at 300 kV had already been achieved [98].

Chromatic aberration gives image blurring because of energy spread of the cold emission source. The blurring is represented by convolution of Gaussian function. According to convolution theorem, Gaussian function does not alter the relative contrast relation (the ratio of the vacancy contrast to the non-vacancy column contrast) but absolute image intensity. By using monochrometer [99,100], and/or chromatic aberration corrector [101-103], the ABF image with high contrast can be obtained.

$LiMn_2O_4$ crystal was observed by ABF imaging with an aberration corrected STEM. In ABF images, all atomic columns including lithium columns are visible as dark dots at over-focuses. As the convergent angle increases, the optimum over-focus giving the maximum intensity approaches to zero-focus. The depth of focus (DOF) decreases, then, and ABF image becomes sensitive to the structure of the top surface: A manganese ion vacancy at the top surface gives the contrast reduction, 10% for 50 mrad, and 25 % for 100 mrad of the convergent angle. A lithium ion vacancy gives the contrast reduction of 15 % for 70 mrad, and 20 % for 100 mrad. This ABF imaging with the large convergence angle of the incident beam could provide the surface image of electrode materials of lithium ion batteries.

2.5 Summary

Since the battery performance depends on the lithium diffusion from anode to cathode, the monitoring of the lithium diffusion is an important issue. For visualization of the diffusion behavior of single lithium ion, ABF imaging is a strong candidate because of its directly lithium imaging ability. However, the imaging mechanism of ABF image is still not uncovered completely.

In this study, we investigated the ABF imaging mechanism for using *in-situ* observation by using aberration corrected electron microscope, R005. The ABF imaging for a thin sample

shows the characteristics of the phase contrast of which contrast has the proportional relationship with the projected potential of the sample. It supports that lithium ion movement can be visualized by *in-situ* ABF imaging. The visualization of the lithium movement during the phase transformation was demonstrated by *in-situ* ABF observation.

The ABF image contrast also has the dependence on the convergent angle of the incident beam: the larger convergent angle give the narrower depth of focus. For monitoring the lithium movement in whole sample the small convergent angle is more suitable while for monitoring the surface of the sample, the large convergent angle.

Therefore, *in-situ* ABF imaging is expected to visualize the single lithium ion movement in lithium ion battery materials during charge/discharge process.

Chapter 3. $LiMn_2O_4$ Nanowire battery for *in-situ* study

3.1 Introduction

As summarized in section 1.2.3, aging of $LiMn_2O_4$ cathode has been studied to conclude several scenarios for the capacity fade out: Mn dissolution into electrolyte [53,69], micro strain [54,70] and fracture due to the Jahn-Teller effect [38,36]. These scenarios are by the fact that valance of the transition metal changes depending on the lithium concentration during charge/discharge cycles. Therefore, lithium concentration change or lithium diffusion process is the key process that correlates with the capacity fade out.

Since lithium diffusion process depends on morphology, defects and electric field applied at the interface between electrode and electrolyte, we need microscope observation during charge/ discharge cycles to see time-dependent behavior of the $LiMn_2O_4$ cathode/electrolyte. Figure 3.1 illustrates our experimental scheme of *in-situ* TEM observation.

In this study, we developed a new nano-battery with nanowire $LiMn_2O_4$ cathode (hereafter, it is called 'nanowire battery'). Also, a new TEM holder was developed for electrically biasing the nanowire battery in TEM. The electrochemical measurement system with the new TEM holder successfully measured the pA-order electrochemical properties of the nanowire battery.

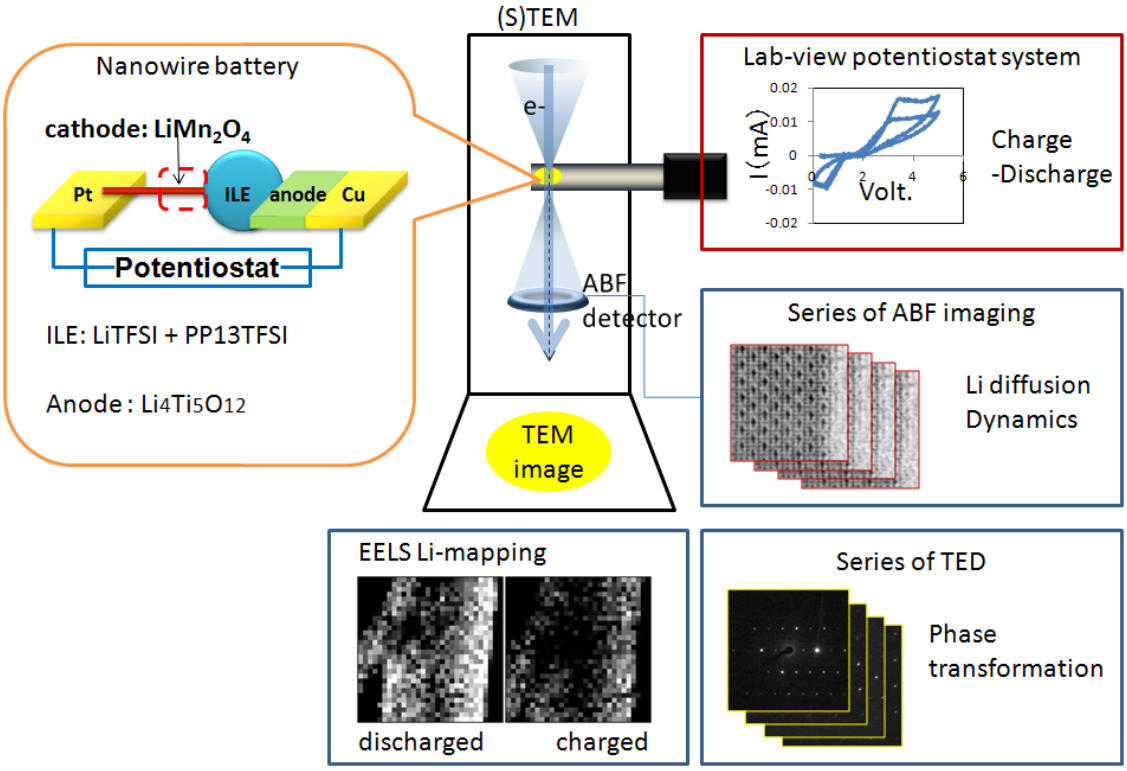

Figure 3.1 The scheme of *in-situ* TEM observation of a new nano-battery. The nano-battery constructed with nanowire was charged and discharged in TEM. The observation is performed with TEM imaging, transmission electron diffraction (TED), ABF imaging and EELS.

3.2 *In-situ* observation system for a nano-LIB

Figure 3.2(a) illustrates the nanowire (NW) battery developed in this work. The nanowire battery consists of $LiMn_2O_4$ nanowire cathode, ionic liquid electrolyte (ILE) and $Li_4Ti_5O_{12}$ anode. The nanowire battery was built on the special sample stage shown in Figure 3.2(b). The sample stage was loaded in the homemade TEM holder which enables us to charge/discharge the nanowire battery. Two electrodes of the holder are connected with source measurement unit (K2635A, Keithley). The electrochemical properties of the nanowire battery were measured by cyclic voltammetry through electric circuit shown in Figure 3.2(d). During charge/discharge cycles, the structure changes of $LiMn_2O_4$ nanowire cathode was observed simultaneously by TEM and transmission electron diffraction (TED). The TEM holder has double tilt axes so as to orient the specimen for structure imaging.

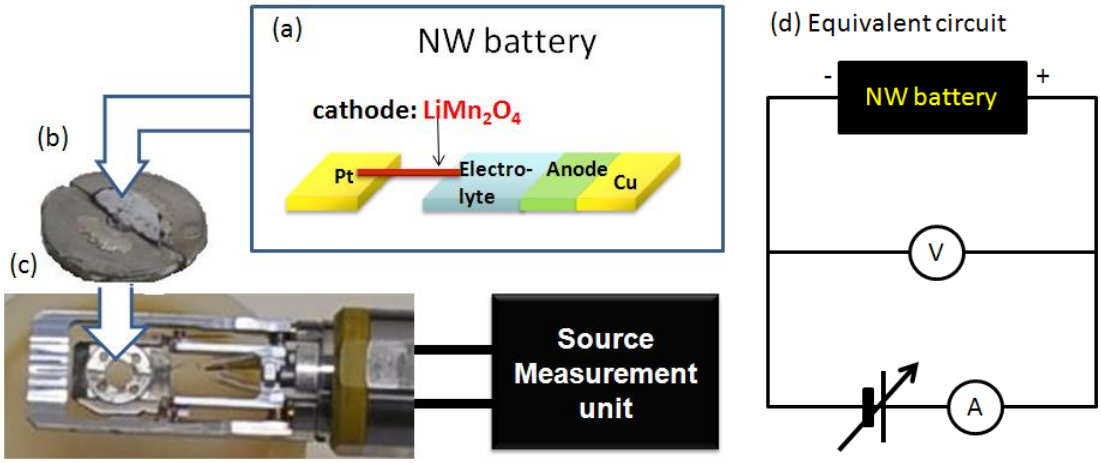

Figure 3.2 The concept of the *in-situ* observation system with a nanowire battery. (a) The schematic illustration of the nanowire battery with $LiMn_2O_4$ nanowire cathode. (b) The optical microscope image of the special sample stage for loading the nanowire battery for TEM observation. (c) The optical microscope image of the developed electric biasing TEM holder. (d) The equivalent circuit of the cyclic voltammetry that we used for evaluating the electrochemical properties of the nanowire battery.

3.3 Structure of nanowire battery

The nanowire battery consists of three parts – cathode, anode and electrolyte. Cathode is made of platinum current collector and $LiMn_2O_4$ nanowires as active materials. Nanowire shape $LiMn_2O_4$ crystals could be understood as a 1-dimensional model electrode of common powder active materials. The $LiMn_2O_4$ nanowires were chosen for understanding the inhomogeneity of active materials depending on the distance from the interface with electrolyte, of course, the nanowire shape giving the benefit of thin thickness of nanowire, easy to observation by TEM, which uses transmitted electron.

Anode is made of copper current collector and $Li_4Ti_5O_{12}$ crystalline powder. A $Li_4Ti_5O_{12}$ crystal is well-known as the most stable anode activation materials. It has been reported the zero strain during charge/discharge reaction [104,105], which causes no stretching or shrinking during *in-situ* observation. A $Li_4Ti_5O_{12}$ crystal also gives the clear electrochemical properties of count electrode ($LiMn_2O_4$ cathode in this study) due to its very flat reaction voltage [104,105].

Ionic liquid is used as electrolyte due to its very low vapor pressure [106], which allows using in high vacuum chamber of TEM (~10^{-6} pa). In order to prevent the short circuit between cathode and anode, we make the slurry of ionic liquid electrolyte (ILE) and the powder of glass-ceramic solid electrolyte, OHARA sheet [107,108]. Since the ionic conductivity of ILE is higher than OHARA sheet [109], the powder of OHARA sheet behaves as only separator. (Without ILE, the cell does not work: no OCV, no charge/discharge properties is obtained.)

The detail of each part is given in following section, and the detail of the construction of a full cell is given in Appendix.

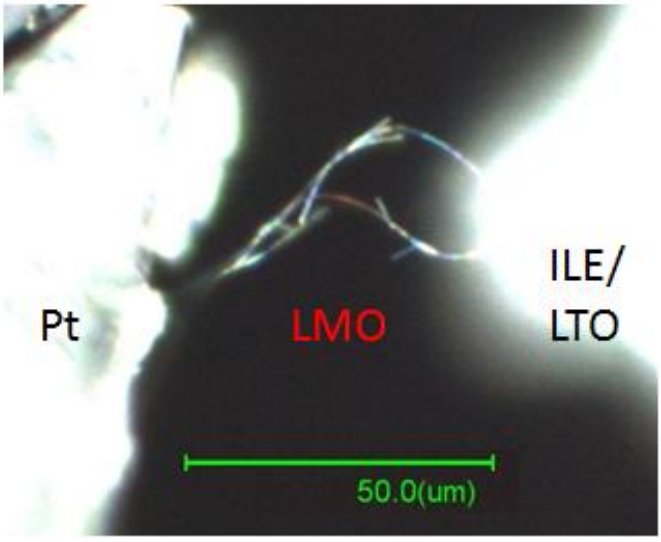

Figure 3.3 The optical microscope image of the nanowire battery.

3.2.1 $LiMn_2O_4$ nanowire cathode

$LiMn_2O_4$ nanowires are provided by Dr. Hosono and Dr. Zhou in AIST. $LiMn_2O_4$ nanowires are fabricated by using template method [20]. First, $Na_{0.44}MnO_2$ nanowires are fabricated by using hydrothermal synthesis. The obtained $Na_{0.44}MnO_2$ nanowires are washed and dried. After that the ion change between sodium and lithium is performed as soaked in the molten salt of lithium salt ($LiCl+LiNO_3$) and washed. Finally, the products are sintered and then they become into $LiMn_2O_4$ nanowires. The $LiMn_2O_4$ nanowires have the normal spinel structure (shown in Figure 1.13~15 in chapter 1). The detail about synthesis is written in Ref. [20].

For identifying the geometry of the nanowires, 20 nanowires were observed by TEM and were classified into mainly four kinds of geometry as shown in Figure 3.4. The largest number of nanowires (60 %) had the geometry shown in Figure 3.4(d), whose surface consists of the {111} planes. Second largest number of nanowire (30 %) had the geometry shown in Figure 3.4(a), whose surface consists of the (100) and (110) planes. Only one nanowire for each case shown in Figure 3.4(b) and (c) was observed (5 %, respectively).

It is considered that the most of nanowires have the {111} surface planes because the (111) plane has lowest surface energy: The (111) surface in face-centered-cubic system has been known to have lowest surface energy due to high atomic density [110] and the dense oxygen layer along the (111) plane would packing lithium ions stably. The *in-situ* surface XRD study has also reported that the (111) plane is more stable than the (110) plane during charge/discharge cycles [32].

Small-diameter nanowires (φ~50nm) are mainly single crystalline as shown in Figure 3.5(a). In contrast, large-diameter nanowires have polycrystalline domains whose boundaries are mainly parallel to the nanowire axis as shown in Figure 3.5(a~c). Of course, some domain boundaries across the section of a nanowire are also detected as shown in Figure 3.5(c). Figure 3.5(e,f) shows the TED patterns obtained from the selected areas in Figure 3.5(d). Figure 3.5(e) shows the TED pattern from the [-122] view direction and Figure 3.5(f) shows the TED from the [011] view direction. For large-diameter nanowires, the number of domains also increase compared with small-diameter one.

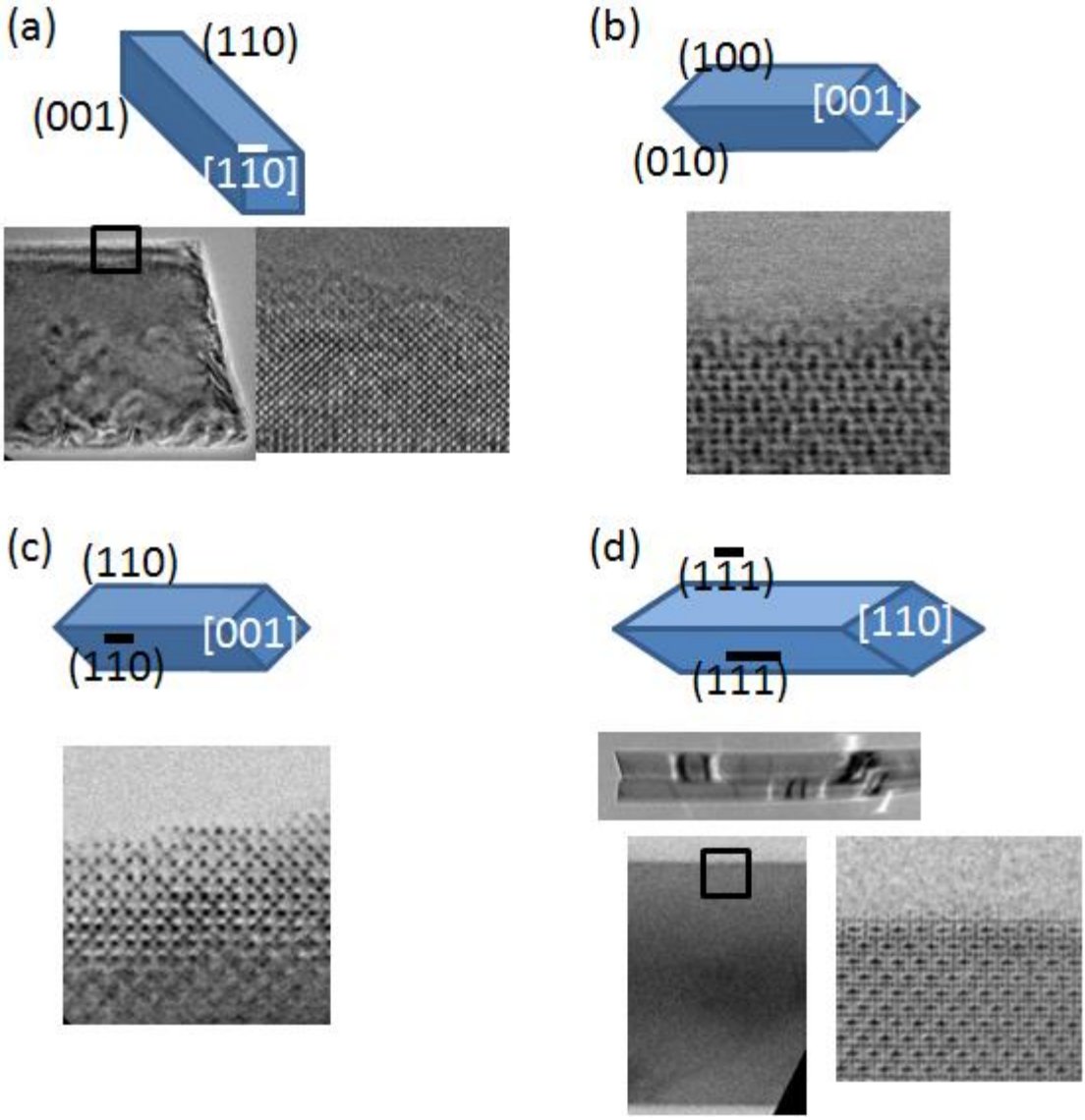

Figure 3.4 Mainly observed four kinds of geometry of $LiMn_2O_4$ nanowires. The schematic of geometry is shown in upper panel and corresponding TEM and/or ABF-STEM images are shown in lower panel for each kind of nanowires.

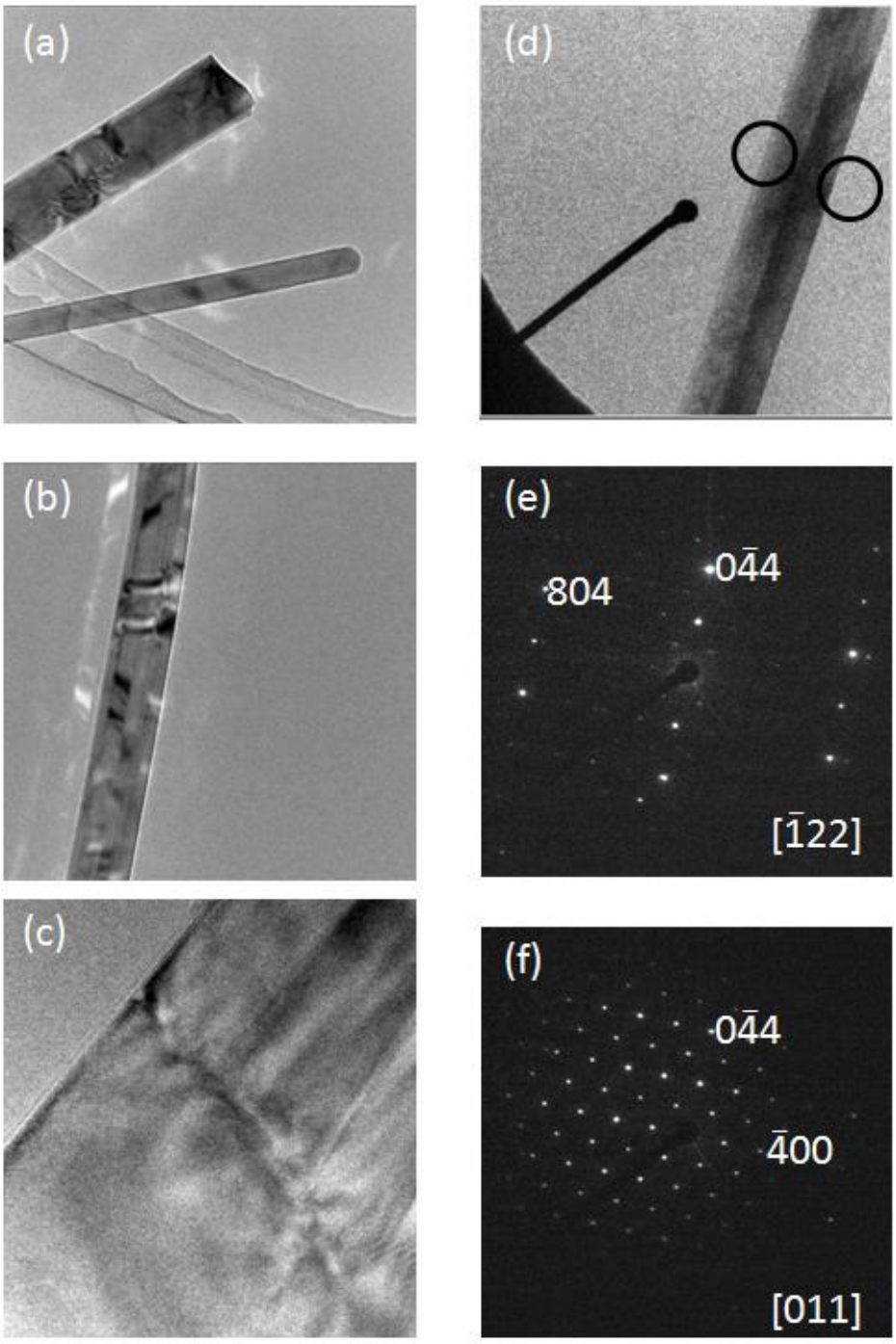

Figure 3.5 Poly-crystal domains in $LiMn_2O_4$ nanowires: (a) thin nanowires have single crystal and (a~c) thick nanowires have poly crystals, whose domain is parallel to the nanowire axis. (a~c) are TEM images with large convergent beam (defocused Ronchigram mode image in STEM) and Kikkuchi bands are visible in nanowires. (c) The domain boundary across the section of a nanowire. (d) The TEM image of a nanowire showing two domains. (e,f) The TED patterns from two selected areas marked by black circles in (d).

3.2.2 $Li_4Ti_5O_{12}$ anode

The $Li_4Ti_5O_{12}$ anode was fabricated as follow:

$Li_4Ti_5O_{12}$ crystalline powder (Sigma-Aldrich,co.), engineering carbon product (ECP, Lion,co.), vapor grown carbon fiber (VGCF, Showa,co) and PolyVinylidene DiFluoride (PVDF, Kureha) were mixed following the weight ratio, $Li_4Ti_5O_{12}$:ECP:VGCF:PVDF=80:8:2:10. The mixture was ground for 15~20 min. And then N-methylpyrrolidone (NMP, Kureha) was added and mixed until the viscosity became like honey. The mixture was spread on copper film (Hosen) by 50 μm thick and dried in heated vacuum desiccators at 110℃ for 10hours.

The obtained $Li_4Ti_5O_{12}$ electrode was tested by making coin cell with lithium metal count electrode. The electrolyte was 1M LiPF4 in EC:DEC=3:7. Figure 3.6 shows the cyclic voltammetry of the coin cell at the scan rate of 0.2 mV/s. The oxidation current peak is symmetric with the reduction peak at 1.6 V vs Li/Li^+. The reaction voltage was stable without significant changes during five charge/discharge cycles.

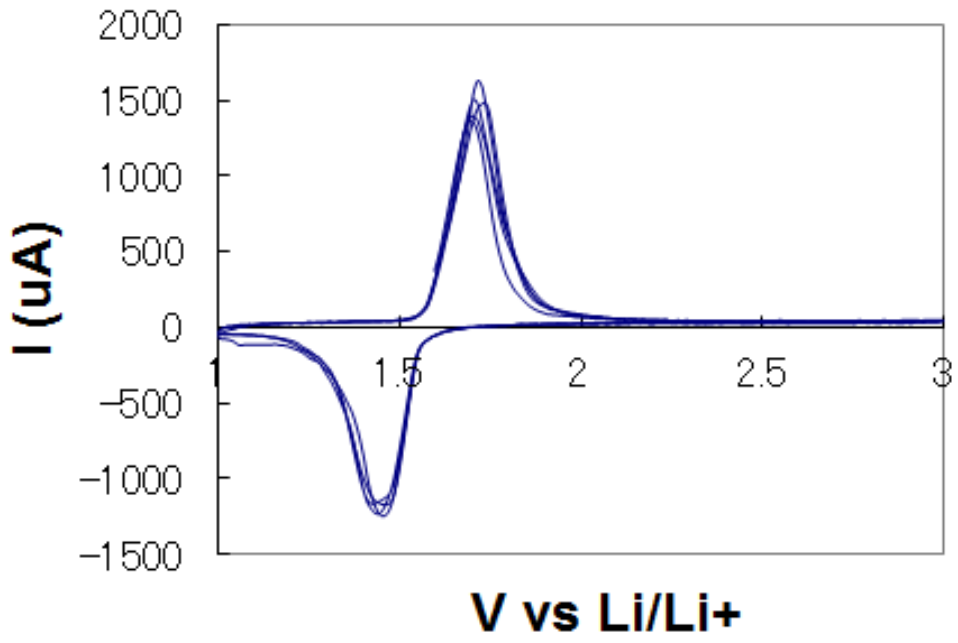

Figure 3.6 The cyclic voltammogram of the coin cell consisting of The $Li_4Ti_5O_{12}$ electrode and lithium metal count electrode. The scan rate was 0.2 mV/s.

3.2.3 Ionic liquid electrolyte

For *in-situ* TEM observation, ionic liquid electrolyte was selected as an electrolyte because its low vapor pressure which enable to perform the battery reaction, charge/discharge in the vacuum environment [106], namely, TEM chamber. 0.5 M Lithium N,N-Bis (trifluoromethane-sulfonyl) imide (Li-TFSI) in *N*-methyl-*N*-propylpiperidinium bis (trifluoromethane- sulfonyl) imide (PP13TFSI) was used as electrolyte. Figure 3.7 shows the structural formula of Li-TFSI and PP13TFSI. In the solution one anion, TFSI, exists. Since the anion is relatively big and its mobility is small, the mobility of the count ion, lithium ion becomes high.

PP13TFSI shows wide potential window as shown in Figure 3.8. From 0 V to 5.3 V (vs Li/Li^+) no redox reaction has been reported to occur [109,111]. Thus, PP13TFSI was suitable as a solvent of ionic liquid electrolyte for in-situ TEM observation, in which large polarization could be accompanied because of the feature of the nanowire battery, small contact area between each component due to miniaturization.

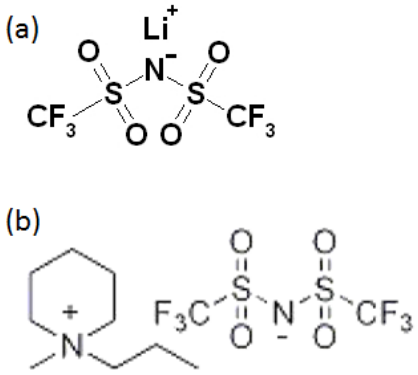

Figure 3.7 The structural formula of (a) Li-TFSI (solute) and (b) PP13TFSI (solvent).

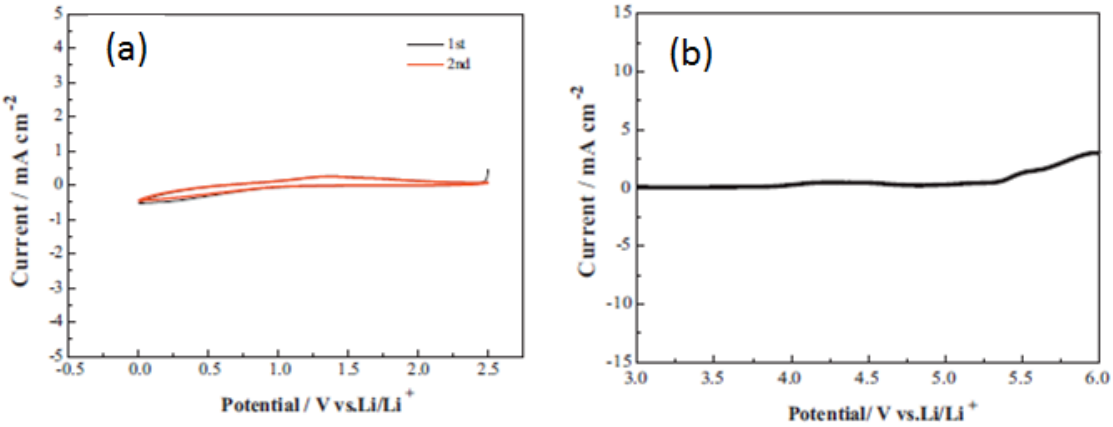

Figure 3.8 Cyclic voltammograms for the voltage range (a) from 0.0 to 2.5 V and (b) 3.0 to 6.0 V. The counter electrode was lithium foil. Working electrode was platinum.

3.3 Electrochemical properties (CV)

The total volume ratio of the $LiMn_2O_4$ nanowire cathode to $Li_4Ti_5O_{12}$ crystal anode (~1/1,000,000) was extremely small in order to keep the voltage of the $Li_4Ti_5O_{12}$ crystal anode during the charge and discharge processes. The cell voltage was converted into voltage vs Li/Li^+ for convenience hereafter.

Figure 3.9 shows the cyclic voltammogram (CV) of the nanowire battery with a $LiMn_2O_4$ nanowire bridge. The voltage was scanned in the range from 3.0 V to 5.0 V vs Li/Li^+ at 2 mV/s. The pair of double anodic/cathodic current peaks is clearly visible, which is characteristics of the 4 V reaction of $LiMn_2O_4$ crystals. For more than 20 cycles, the positions of these current peaks are almost the same in spite of pA-order current level. It shows that the nanowire battery works as a rechargeable battery with the stable cell potential.

The optical images and their properties for another three nanowire batteries are shown in Figure 3.10 and Table 3.1. The practical capacity for each battery is estimated from its cyclic voltammetry curve. The practical capacity is about 80 % of the theoretical capacity estimated from its geometry. Therefore, at least, in the position of 80 % of whole length of the $LiMn_2O_4$ nanowire from ILE, lithium ions were extracted and inserted.

We performed *in-situ* TEM observation during charge/discharge cycles at the vicinity area from ILE and at the position far from ILE by about 50 μm. The results from the vicinity area from ILE will be given in chapter 4 and that of the position far from ILE in chapter 5.

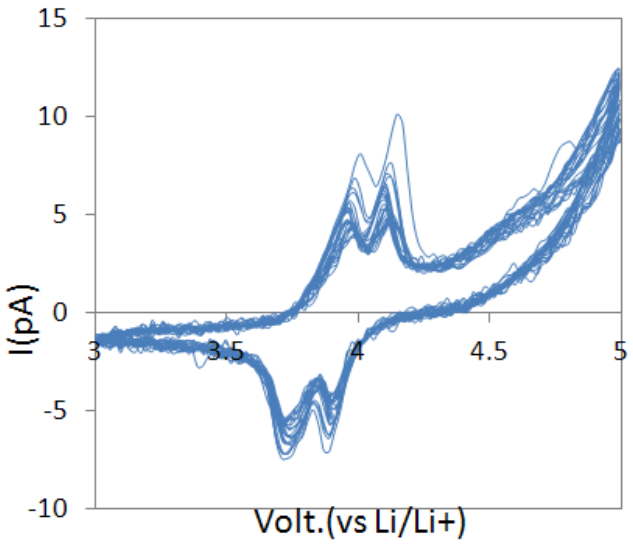

Figure 3.9 Cyclic voltammogram of a nanowire-battery with a single $LiMn_2O_4$ nanowire bridge obtained by *ex-situ* measurement. Cyclic voltammetry was performed between 3.0 V and 5.0 V vs Li/Li^+ at a scan rate of 2 mV/s.

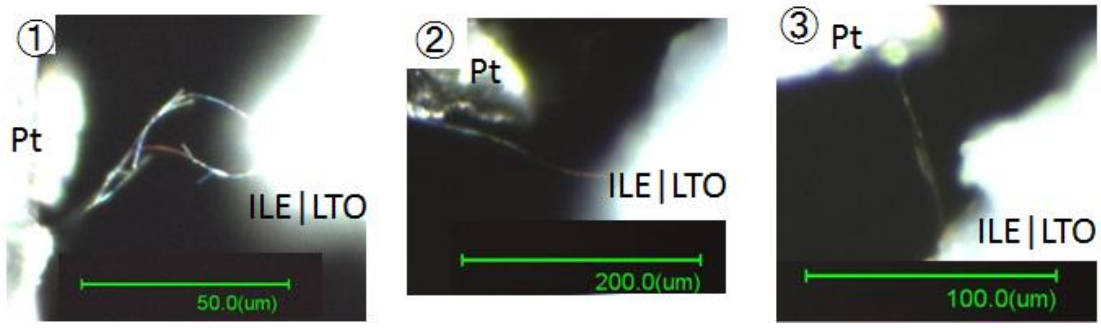

Figure 3.10 The optical microscope images of three nanowire batteries. Second one is made of single long nanowire.

Sample	D (nm)	Scan speed (mV/s)	Capacity (pC)	Corresponding reacted/ whole NW length(um)	
①	200	0.55	2500	**40/50**	**(80%)**
②	200	0.55	900	**140/170**	**(80%)**
③	100~150	0.55	800	**30/70**	**(40%)**

Table 3.1 The diameter, scan speed(experimental condition), estimated capacity from cyclic voltammetry and the corresponding length to the capacity for three nanowire batteries shown in Figure 3.10. The sample number corresponds that in Figure 3.10.

3.4 Summary

For *in-situ* TEM observation, we successfully developed the nanowire battery and the new double tilt bias holder. The nanowire battery consists of $LiMn_2O_4$ nanowire cathode, ionic liquid electrolyte and $Li_4Ti_5O_{12}$ anode. The nanowire battery shows the clear 4 V reaction of $LiMn_2O_4$ crystals in the electrochemical measurement by using the extremely small ratio of $LiMn_2O_4$ to $Li_4Ti_5O_{12}$, ~1 ppm: A pair of double peaks is detected in cyclic voltammetry.

The *in-situ* observation system including the new holder detected pA-order low current peak. The measurement ability enables to match the electrochemical properties and structural change monitored by TEM observation.

Chapter 4. Reversible $LiMn_2O_4$ nanowire-battery working at the 4 V range

4.1 Introduction

In chapter 3, we introduced our developed nanowire battery and *in-situ* observation system. For monitoring the structure change of the $LiMn_2O_4$ cathode causing capacity fading, *in-situ* TEM observation was performed. The vicinity of the interface area of $LiMn_2O_4$ cathode with ILE was monitored during charge/discharge cycles.

In this study, by *in-situ* TEM observation, the deterioration mechanism of $LiMn_2O_4$ cathode during 4 V reaction was revealed: the tetragonal phase appeared at the interface region of $LiMn_2O_4$ nanowires with the electrolyte at early discharge stage, 3.9 V vs Li/Li^+.

Furthermore, the tetragonal phase was reversibly restored to the cubic phase without fracture of the nanowires during the charge process. No fracture while cubic-tetragonal transition is promising for the long-life-time battery with $LiMn_2O_4$ nanowire cathode.

4.2 TEM image of a nanowire-battery

Figure 4.1(a) shows the illustration of our developed nanowire battery. Figure 4.1(b) shows a typical TEM image of the nanowire batteries. Between the gap (50~200 μm) of Pt current collector and ILE, $LiMn_2O_4$ nanowire bridges were shown. At the contact area with ILE, sides of $LiMn_2O_4$ nanowires were cover by thin ILE layer due to capillary phenomenon for 1~3 μm distance from ILE. Due to the high lithium diffusion coefficient in liquid [109,112], this covered area acts as the actual interface where lithium ions are inserted into or extracted from the nanowire.

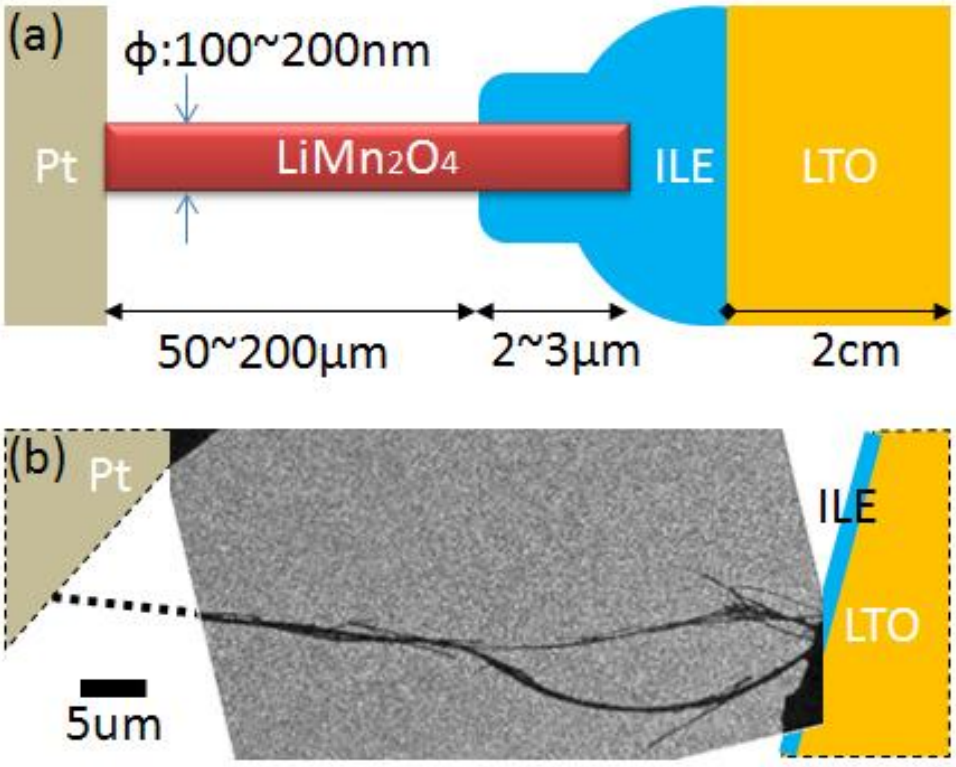

Figure 4.1 (a) Schematic illustration of nanowire-battery. A $LiMn_2O_4$ nanowire-bundle is bridged between Pt current collector (left) and ionic liquid electrolyte (ILE). $Li_4Ti_5O_{12}$ crystals were used as an anode. At the vicinity of ILE, the nanowire is covered by thin ILE layer for a few micrometers. (b) Typical TEM image of 'nanowire-battery'. Two $LiMn_2O_4$ nanowire bridges are contacted with ILE (right bottom).

4.3 *In-situ* TEM observation

In-situ TEM observation was carried out using our home-made electrical biasing double tilt TEM holder. Cyclic voltammetry (CV) was performed by scanning voltage from 3.50 V to 5.50 V vs Li/Li^+ at 0.55 mV/s. The measurement was performed by source-measurement unit, Keithley 2635A. During charge/discharge cycles, crystalline $LiMn_2O_4$ nanowires in the nanowire-battery were observed by an aberration-corrected TEM, R005 at 300 kV. The diffraction spots of the TED patterns were analyzed by comparing with the TED patterns of silicon crystal viewed from the [110] and [111] directions, which were obtained under the same experimental conditions with the present study.

4.3.1 Electrochemical properties

For *in-situ* TEM observation of the nanowire cathode–ILE interface with electrochemical measurement, we fabricated nanowire batteries with a thicker cathode, i.e., about ten bridges of $LiMn_2O_4$ nanowires. Figure 4.2 shows the CV of the nanowire battery while TEM observation. A pair of double current peaks is visible: two anodic current (Li de-insertion) peaks appear at 4.1 and 4.7 V vs Li/Li^+, and two cathodic current (Li insertion) peaks, at 3.9 and 3.6 V (marked by arrow heads in Figure 4.2). The two anodic/cathodic current peaks look broad compared with those in Figure 3.9. This is because each bridge of the nanowires had different impedance and/or contact resistance with the electrolyte to scatter the current peaks. The anodic/cathodic peak current in Figure 4.2 were about ten times higher than those in Figure 3.9. Since these double current peaks correspond to the 4 V reaction, the concentration of lithium ions, x, of $Li_xMn_2O_4$ crystal is expected to change between 0 and 1.

The cell capacity during charge was estimated to be ~30 nC (8.6×10^{-9} mAh) from the CV of Figure 4.2. This amount corresponds to about a half of lithium ions contained in the whole $LiMn_2O_4$ nanowire cathode. The nanowire cathode, bridged between Pt current collector and ILE, had ten $LiMn_2O_4$ bridges of 100 μm in length and 200 nm in diameter. Thus, the lithium ions moved not only from the area of $LiMn_2O_4$ – ILE interface, but also from inside of the $LiMn_2O_4$ nanowires. In the present nanowire battery reactions, a half of the whole nanowires cathode was estimated to react at least for charge/discharge process.

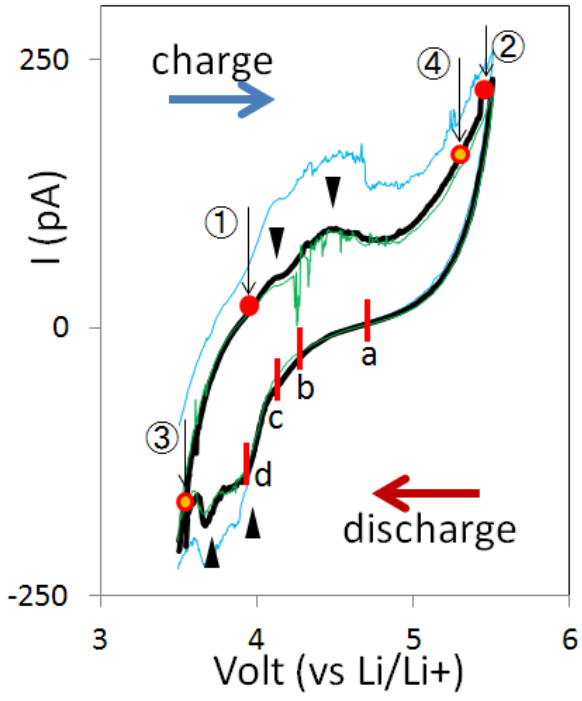

Figure 4.2 Cyclic voltammogram of the nanowire battery with ten $LiMn_2O_4$ nanowire-bridges obtained during *in-situ* TEM observation. Cyclic voltammetry was performed between 3.5 V and 5.5 V vs Li/Li^+ at a scan rate of 0.55 mV/s. Black arrow heads indicate a pair of double (anodic/ cathodic) current peaks. Transmission electron diffraction patterns were obtained following the order of ①-②-a-b-c-d-③-④ which are shown in Figure 4.5 and 4.6

4.3.2 Morphology and phase change during battery cycles

4.3.2.1 Morphology change

During the charge/discharge cycles, the vicinity of the contact point of $LiMn_2O_4$ nanowire with ILE was observed by *in-situ*. The observation area is shown in Figure 4.3(a). The observed area was far from ILE by about 2 μm. The surface of $LiMn_2O_4$ nanowire at the vicinity area of the contact point with ILE was covered by thin ILE layer because of capillary phenomenon. The covered area was about 3 μm from ILE. Thus, the observation area was covered by thin ILE layer as shown in Figure 4.3 (b).

Figure 4.4 shows the TEM images after every charge/discharge cycles – 1st, 2nd and 3rd cycle. The morphology of $LiMn_2O_4$ nanowire did not changed although the thickness of ILE layer which covered the surface of nanowire became thicker. No crack and fracture was observed during four cycles.

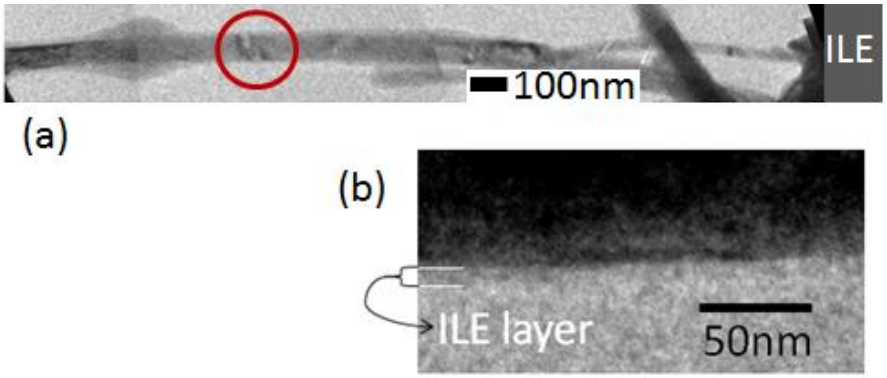

Figure 4.3 (a) TEM image of a single $LiMn_2O_4$ nanowire which contact ionic liquid electrolyte (right-side). The observation area is marked by a red circle. (b) The thin ILE layer which covered the nanowire at the observed area.

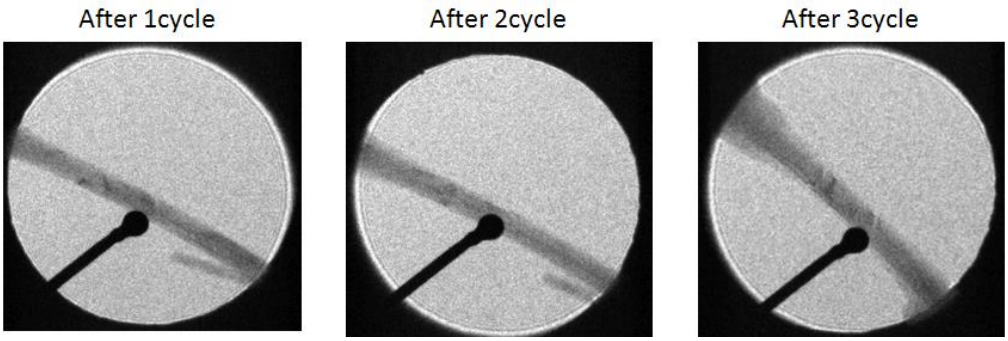

Figure 4.4 TEM images of the observation area of the $LiMn_2O_4$ nanowire after 1, 2 and 3 charge-discharge cycles. The shadows of high contrast aperture and beam stopper are shown as dark contrast.

4.3.2.2 Phase change

Transmission electron diffraction (TED) patterns of the observation area simultaneously obtained with measuring the CV (Figure 4.2) are shown in Figure 4.5. The fitted lattice parameters for each case are given in Appendix (Table A1). The wire axis of the nanowire was the [110] direction of the spinel cubic structure. The $LiMn_2O_4$ nanowire had the cubic phase before the charge process (①) as shown in Figure 4.5(b). The cubic phase was maintained during charge process (① to ② of Figure 4.5b). In the discharge process, the cubic structure was found to change into the tetragonal phase (② to ③ of Figure 4.5b). In the next charge process, the tetragonal phase was recovered into the cubic phase again (③ to ④ of Figure 4.5b). The $LiMn_2O_4$ nanowires changed the structure between the cubic and tetragonal phases reversibly during further charge and discharge processes.

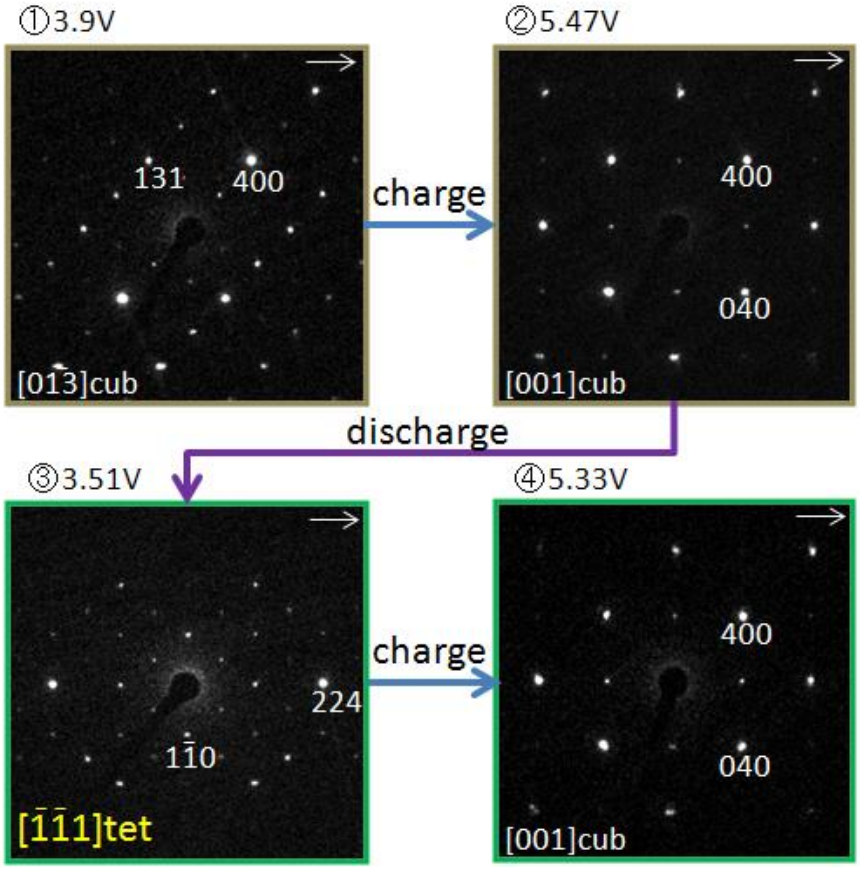

Figure 4.5 Change of the transmission electron diffraction (TED) pattern of the $LiMn_2O_4$ nanowire during charge/discharge cycles. TED patterns ①, ②, ③, and ④ were obtained at spots marked by the same numerical symbols in Figure 4.2. The horizontal direction of TED patterns is the projected nanowire axis (white arrow).

Figure 4.6 shows a details of the cubic-tetragonal phase change during the discharge process, a series of TED patterns was taken at 4.70, 4.25, 4.12 and 3.90 V, respectively (as indicated by red bars on the CV curve of Figure 4.2). At 4.70 V (Figure 4.6a), the nanowire cathode had a cubic structure. At 4.25 V (Figure 4.6b), which corresponds to the beginning of discharge process, the diffraction spots started being split along the $[1\text{-}10]_{cub}$ direction (marked by arrows), while they did not split along the $[110]_{cub}$ direction of the wire axis. The TED pattern (Figure 4.6b) means coexistence of the original cubic structure and an orthorhombic structure at 4.25 V. And, the orthorhombic phase has larger lattice spacing than the cubic phase in the normal direction to the nanowire surfaces, while it keeps the same lattice spacing with the cubic phase in the wire axis.

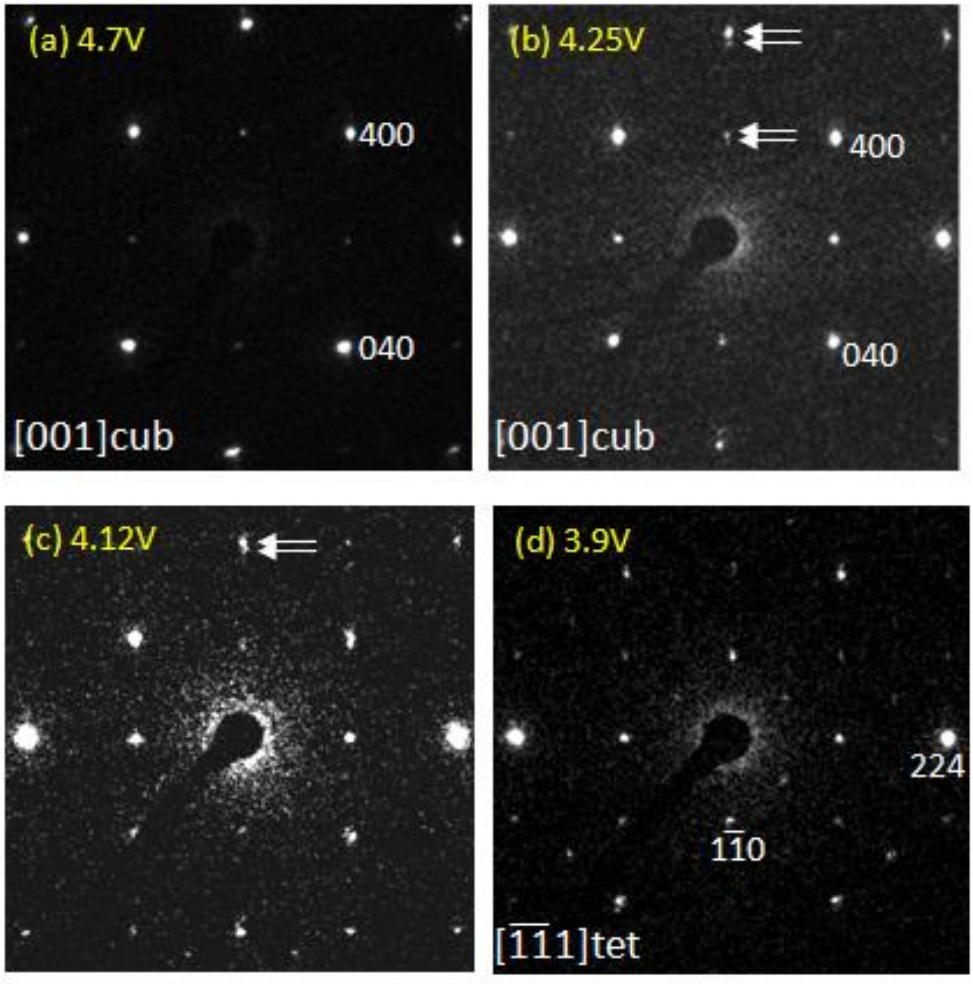

Figure 4.6 (a)-(d) A series of TED patterns taken during the discharge process at 4.70, 4.25, 4.12 and 3.90 V, respectively, of CV curve as indicated by red bars in Figure 4.2. The split diffraction spots are marked by white arrows. The horizontal direction of TED patterns is the projected nanowire axis.

By further discharge, the lattice spacing of the orthorhombic phase increased along the normal direction to the surfaces. And even the cubic phase started to change into orthorhombic structure: In Figure 4.6(c) (at 4.12 V), the spots for the cubic phase ($[1\text{-}10]_{cub}$ spot) were displaced from the original positions toward the orthorhombic ones (the ratio of the lattice spacing of 4-40 spot to 440 spot is shown in Figure 4.8). Finally, the tetragonal phase (a=5.57 Å, c=8.71 Å, c/√2a~1.11, where 'a' is the lattice parameter in the tetragonal structure) appeared as shown in Figure 4.6(d) (at 3.9 V). The appearance is during the first cathodic double-peaks in the CV curve.

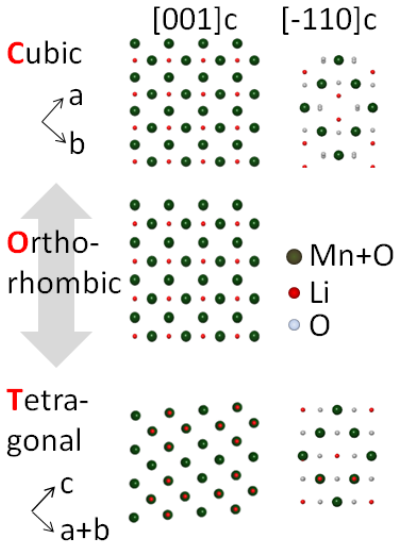

Figure 4.7 Atomic structure models of cubic, orthorhombic and tetragonal phase observed. In orthorhombic phase, the lattice spacing is expanded along the normal direction to the surface as indicated by the gray arrow.

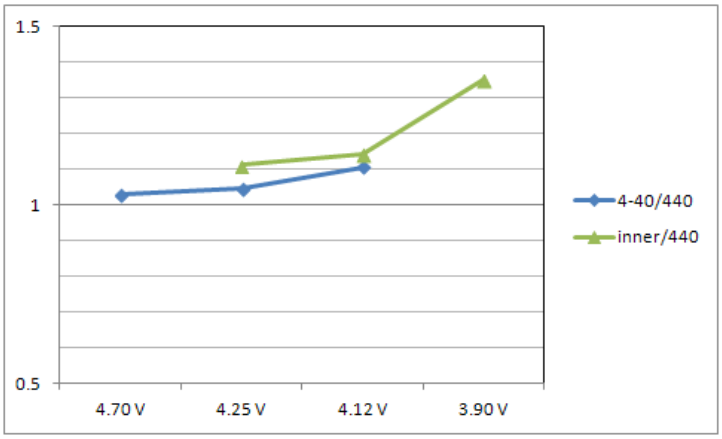

Figure 4.8 The ratio of lattice spacing of the 4-40 spot to the 440 spot changed in during the early stage of discharge. The new phase (marked by the inner arrows from direct spot) in Figure 4.6 is noted as 'inner'. The lattice spacing of the 440 spot was not changed during the discharge process.

4.4 Discussion

4.4.1 Li-rich interface area of $LiMn_2O_4$ Nanowire

After the present *in-situ* observations demonstrated in Figure 4.2 ~ 4.8, we consider about the observed cubic-tetragonal transformation of the nanowire cathode during the 4 V reaction. As seen in the TED patterns of Figure 4.6, the tetragonal phase is obviously nucleated at 3.90 V during the 4 V reaction. It has been known, however, that charged and discharged $Li_xMn_2O_4$ crystals during the 4 V reaction ($0<x\leqq1$) have only cubic phases by previous x-ray diffraction studies [113,114]. In addition, our CV curve (Figure 4.2) shows that concentration of lithium ions at 3.90 V is below x=0.5, being judged from the position of the cathodic double peaks (arrow heads in Figure 4.2). A key observation which gave us an understanding of tetragonal phase formation is the TED patterns in Figure 4.6. At 4.25 V, the orthorhombic phase appears with the cubic phase. The lattice spacing of both orthorhombic and co-existing cubic phase gradually expand along the normal direction to the surfaces by further discharge process until sudden structure transformation into the tetragonal phase occurs at 3.90 V. The process of this phase transformation indicates that the orthorhombic phase is a precursor of the tetragonal transition, and the gradual lattice expansion indicates *the local concentration increase* of lithium ions *in correlation* with the discharge process. We thus consider that lithium-rich region generated locally, at least in the TED observation area, promoted the observed phase transition from the cubic to the tetragonal via orthorhombic phase. As a candidate of highly lithium-rich region, we consider the surface region of the nanowire cathode, more precisely, the interface between the nanowire and ILE (see, Figure 4.1 and Figure 4.3). Of course, low lithium diffusion rate inside the $LiMn_2O_4$ nanowire cause the lithium-rich interface region. The phase transformation was not detected by CV. It can be explained by the fact that the portion of the observed tetragonal phase is too small in comparison with the reaction region of the nanowire (about half of whole nanowire cathode as mentioned above). We think that the observed tetragonal transformation is not caused by oxygen deficiencies, although tetragonal formation due to oxygen defects [115] must be cared. Our observed values of tetragonality (c/a~1.11 and 1.17) were larger than the one due to the oxygen defect (c/a~1.07). We also confirmed the tetragonal formation is not affected by imaging electrons. The cubic spinel structure of the $LiMn_2O_4$ nanowire was not changed even after twelve hours electron irradiation under the same illumination condition with this study.

A possible scenario explaining our tetragonal transition, then, is different local lithium diffusion rates, which results in the inhomogeneous lithium distribution in a $LiMn_2O_4$ nanowire. Figure 4.9 schematically illustrates the distribution of the lithium ions in the $LiMn_2O_4$ nanowire during

discharging process. After charge process, the $LiMn_2O_4$ nanowire has low lithium concentration (shown as blue area in Figure 4.9), having cubic phase (shown in top of Figure 4.7b). At the beginning of the discharge process, lithium ions are accumulated at the interface with ILE, or, surface region of the nanowire, due to fast lithium insertion. Then, the lithium ions are gradually diffused towards the core region of the nanowire. The lattice spacing of the lithium-rich surface layer expands along the normal direction to the surface, while keeping a coherent interface with the cubic core region along the wire axis (orthorhombic phase shown in middle of Figure 4.7b). As discharge proceeds, the boundary of orthorhombic surface propagates toward cubic core region of the nanowire. When local valence of Mn ions lower below the critical value [115] due to the lithium accumulation, the lithium-rich region transforms into the tetragonal phase (shown in bottom of Figure 4.7b) by Jahn-Teller effect. Finally, the lithium ions are diffused along the wire axis through the tetragonal phase.

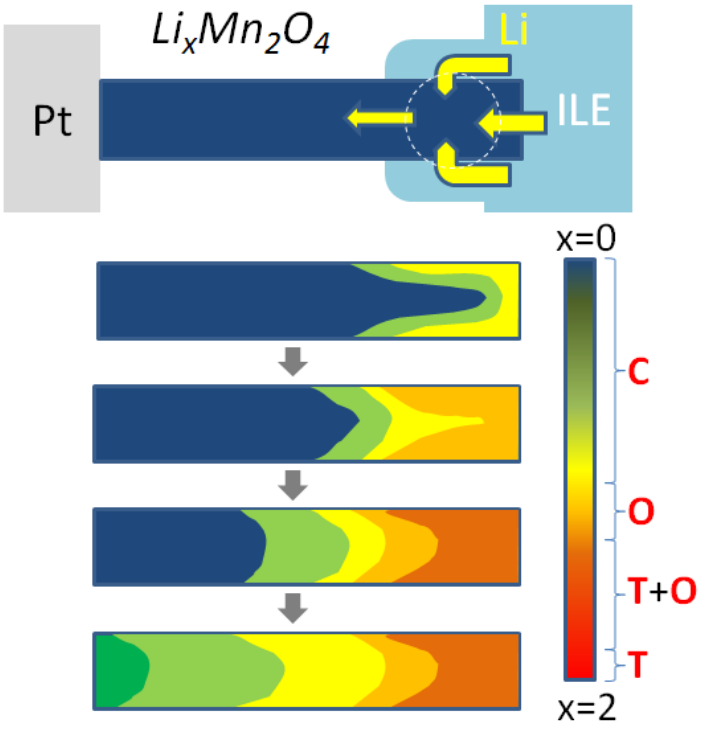

Figure 4.9. (a) Schematic illustration of lithium concentration (x) change in a $Li_xMn_2O_4$ nanowire during discharge. Color indicates the amount of Li concentration. Red capital letters of color scale bar corresponds to each phase, cubic, orthorhombic and tetragonal shown in Figure 4.6. (b) during discharge process (not equilibrium phase).

4.4.2 Reversible cubic to tetragonal phase transformation without fracture

We found that the $LiMn_2O_4$ nanowire was completely restored into the cubic phase from the tetragonal phase in the charge process without fracture. No crack formation was confirmed also by TEM observation (not shown). It is different from the $LiMn_2O_4$ particles, which has been pointed out to be damaged due to the tetragonal formation [37,38]. It might be interesting to consider some mechanisms avoiding fracture. We consider firstly geometric relationships between the cubic and tetragonal phases in the $LiMn_2O_4$ nanowire cathode. For cubic-tetragonal transformation in Figure 4.4, the lattice spacing along the wire axis was conserved: The tetragonal (c/a=1.11)/cubic geometry is $[001]_{tet}//[010]_{cub}$ and $(224)_{tet}//(110)_{cub}$ for the $[110]_{cub}$ wire axis. In another case (Figure 4.10, the fitted lattice parameter is shown in Appendix, Table A2), however, the lattice spacing expanded by 6 % in the wire direction, and 11 % in the normal direction to the surface: The tetragonal (c/a=1.17)/cubic geometry is $[001]_{tet}//[001]_{cub}$ and $(100)_{tet}//(110)_{cub}$ for the $[110]_{cub}$ wire axis. Thus, tetragonal phases grew in the orientation that minimizes the lattice dilatation along the wire axis, taking advantage of the free surface. In addition, the fact that the orthorhombic layer formed along with the nanowire surface covered by ILE must be important, because one mediates between the tetragonal and cubic phases. Nothing has such one-dimensional characteristic but the nanowire. The observed reversible phase transformation without fracture supports that $LiMn_2O_4$ nanowires are promising as a cathode material improving the life-time of $LiMn_2O_4$ crystals based batteries.

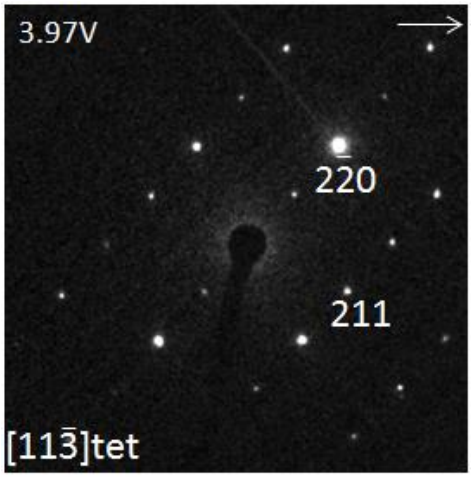

Figure 4.10 The TED pattern of the observed area obtained after another discharge process. The TED pattern shows that the observation area was tetragonal phase with the tetragonality, c/a~1.17. The horizontal direction of TED patterns is the projected nanowire axis (white arrow).

4.5 Summary

We directly observed the structure change of $LiMn_2O_4$ nanowire cathode, *in-situ* by electron microscopy and diffraction, during the charge and discharge processes while measuring the cyclic voltammetry. We found that cubic-tetragonal phase transformation occur at the interface area of $LiMn_2O_4$ nanowire cathode with ionic liquid electrolyte during early discharge stage, 3.90 V, but no fracture of the nanowire occur while 4 V reaction. In discharge processes, the cubic phase of the nanowire transforms firstly into the orthorhombic phase at the side surfaces covered by ILE, and secondly the orthorhombic phase transforms into the tetragonal phase. The appearance of tetragonal phase is understood by local lithium accumulation. Orthorhombic phase that mediates cubic-tetragonal transformation, and strain release via the surface layer avoid the fracture.

Chapter 5. Lithium diffusion inside a single $LiMn_2O_4$ nanowire LIB

5.1 Introduction

The lithium diffusion in macro scale has been studied by electrochemical studies [112,116-119] and X-ray diffraction (XRD) studies [59,60]. For increasing demands on nanoscale understanding of diffusion process in relation with electrochemical CV behavior, in-situ electron microscope observation has become indispensable. For clarifying the lithium diffusion behavior inside of $LiMn_2O_4$ crystal, we devised a model LIB having a single $LiMn_2O_4$ nanowire as a cathode. A single nanowire is important to restrict diffusion path of lithium ions within the nanowire.

In this chapter, the observed behavior of the phase transformation (phase boundary movement) due to lithium movement is reported. And the relationship with the lithium diffusion is discussed based on the simultaneously measured cyclic voltammetry curve.

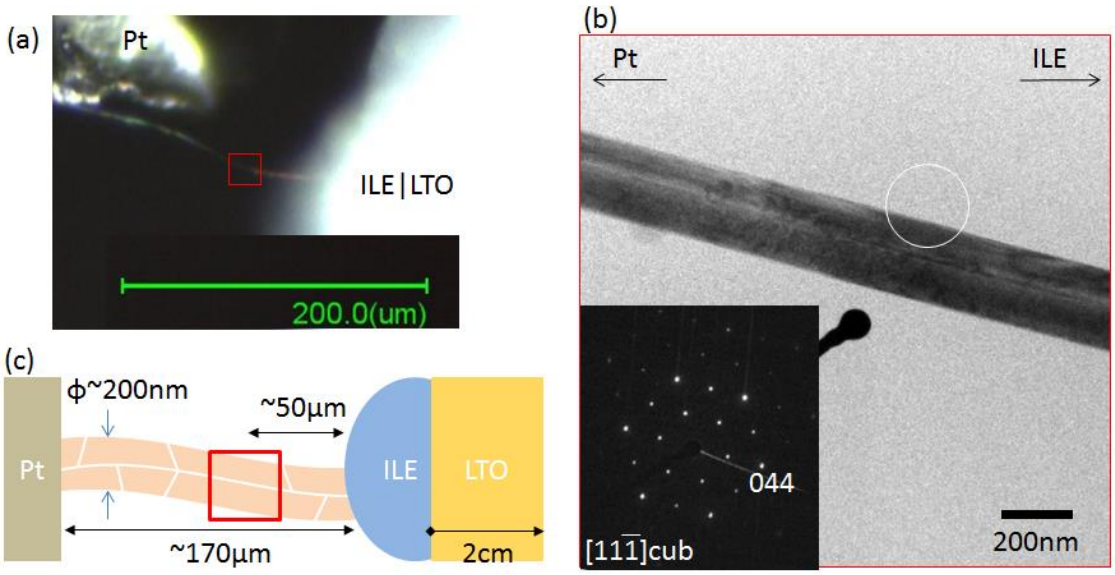

Figure 5.1 (a) The optical microscope image of a single-nanowire battery. The observed area is marked by a red square. (b) The TEM image of observation area. The inset is the TED pattern obtained from the area marked by white circle. The nanowire axis was the [011] direction. (c) Schematic illustration of a single-nanowire battery. White lines in the nanowire are crystalline domain boundaries (see, section. 3.2.1).

5.2 Single $LiMn_2O_4$ nanowire LIB

Figure 5.1 (a) shows an optical microscope image of the nanowire battery whose cathode consists of a single $LiMn_2O_4$ nanowire. Figure 5.1(b) shows the TEM image of the pristine nanowire of the nanowire battery shown in Figure 5.1(a). The pristine $LiMn_2O_4$ nanowire had a morphology illustrated in Figure 5.1 (c). The nanowire was polycrystalline but the nanowire axis was the [011] direction. The diameter of the nanowire was about 200 nm and the length was about 170 μm. The observed area is marked by a red square, which is about 50 μm apart from the $LiMn_2O_4$/ILE interface. The observed area had <111> orientation as shown in the inset of Figure 5.1 (b) and was not covered by ILE layer.

During the charge/discharge cycles, cyclic voltammogram and TEM images were obtained simultaneously.

5.3 *In-situ* TEM observation

5.3.1 Electrochemical properties

Figure 5.2 shows the cyclic voltammetry (CV) of the nanowire battery shown in Figure 5.1. The $LiMn_2O_4$ nanowire was delithiated (charged) at first (①). And then, discharge (②) and charge (③) process was performed. The voltage was scanned in the range from 2.7 V to 5.2 V at the rate of 0.55 mV/s. On the discharge process (②), the cathodic current started to flow at around 3.9 V, and shows two cathodic current peaks at 3.4 V and 3.2 V. The cathodic current was steeply decreased at around 3.1 V. It appears that some (small amount of) residual cathodic current remains until around 3.0 V. On the sequential charge process, the anodic current started to flow above 4.1 V, and shows two anodic peaks at 4.6 and 4.8 V. The anodic current was steeply decreased around 4.9 V. Some residual anodic current remains until around 5.0 V. A pair of double cathodic/anodic current peaks is the characteristic of 4 V reaction of $LiMn_2O_4$ crystals.

The peak current was about 15 pA at 4.8 V (after subtraction of background). The current density across the nanowire section was about 50 mA/cm^2 at the current peak. The charge capacity estimated from CV was about 9 nC, which corresponds to the charge of the amount of lithium ions in about 80 % volume of the $LiMn_2O_4$ nanowire with its geometry. In other words, all lithium ions in about 80 % volume of the $LiMn_2O_4$ nanowire would be extracted during the charge process.

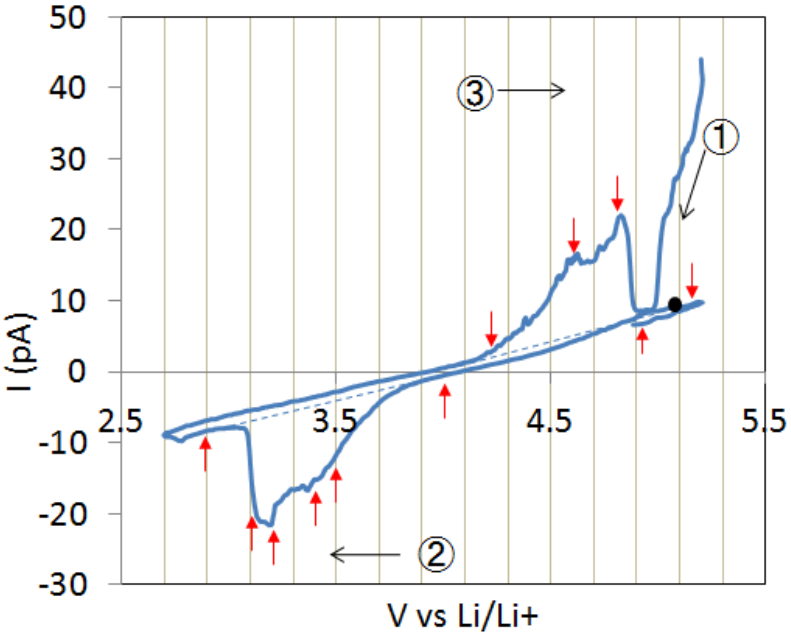

Figure 5.2 The cyclic voltammogram (CV) of the nanowire battery with a single $LiMn_2O_4$ nanowire. The cyclic voltammetry was performed in order of the numbers (①→②→③) with the scan rate of 0.55 mV/s. Red arrows correspond to TEM images shown in Figure 5.6. Black dot at 5.07 V corresponds to TED patterns shown in Figure 5.4. The broken lines in CV correspond to the background current level for estimating the charge/discharge capacity.

5.3.2 *in-situ* TEM images and phase boundary

During the discharge-charge process, phase boundary movement was monitored. Figure 5.3 shows the TEM image of the boundary obtained after the charge process (marked by black dot in Figure 5.2). The boundary had the contrast which consists of many dark and bright fringes across the nanowire section as shown in Figure 5.3. The transmission electron diffraction (TED) patterns obtained from the phase boundary area, left area of the boundary, the boundary area and right area of the boundary, are shown in Figure 5.4. The TED pattern from the left area of boundary shows <100> orientation of the cubic spinel phase as shown in Figure 5.4 (a), while The TED pattern from the right area shows <111> orientation as shown in Figure 5.4 (c). The TED of the boundary area are shown as a mixture of <100> and <111> orientation ones, which correspond to TEDs from the left area and the right area respectively. Thus, the boundary was the domain boundary between two different crystal orientations.

Additional weak peaks can be indexed by the cubic the spinel structure (see, Appendix). In all of three TED patterns, 200 spot and any diffraction spots due to super lattice were not detected.

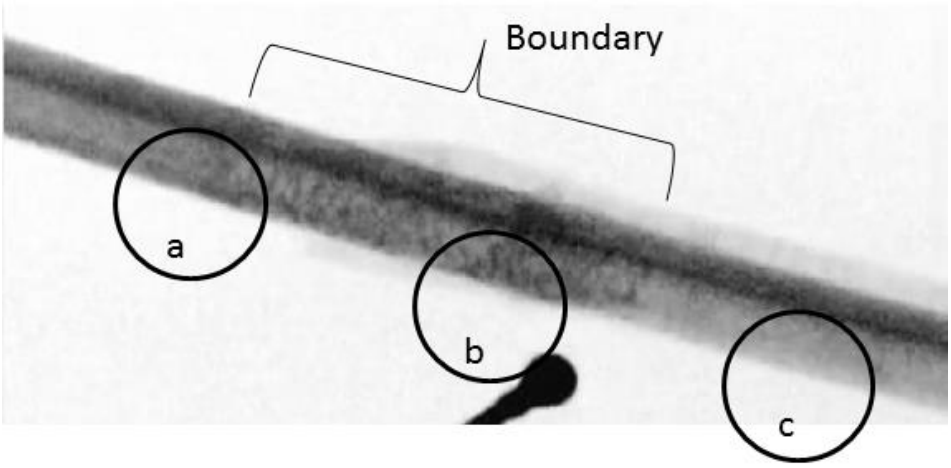

Figure 5.3 The TEM image of the phase boundary obtained after charge process (at 5.07 V, marked by a black dot in Figure 5.2). The boundary has the contrast which consists of many dark and bright fringes across the nanowire section. TED patterns from the black circled areas - a, b and c are shown in Figure 5.4

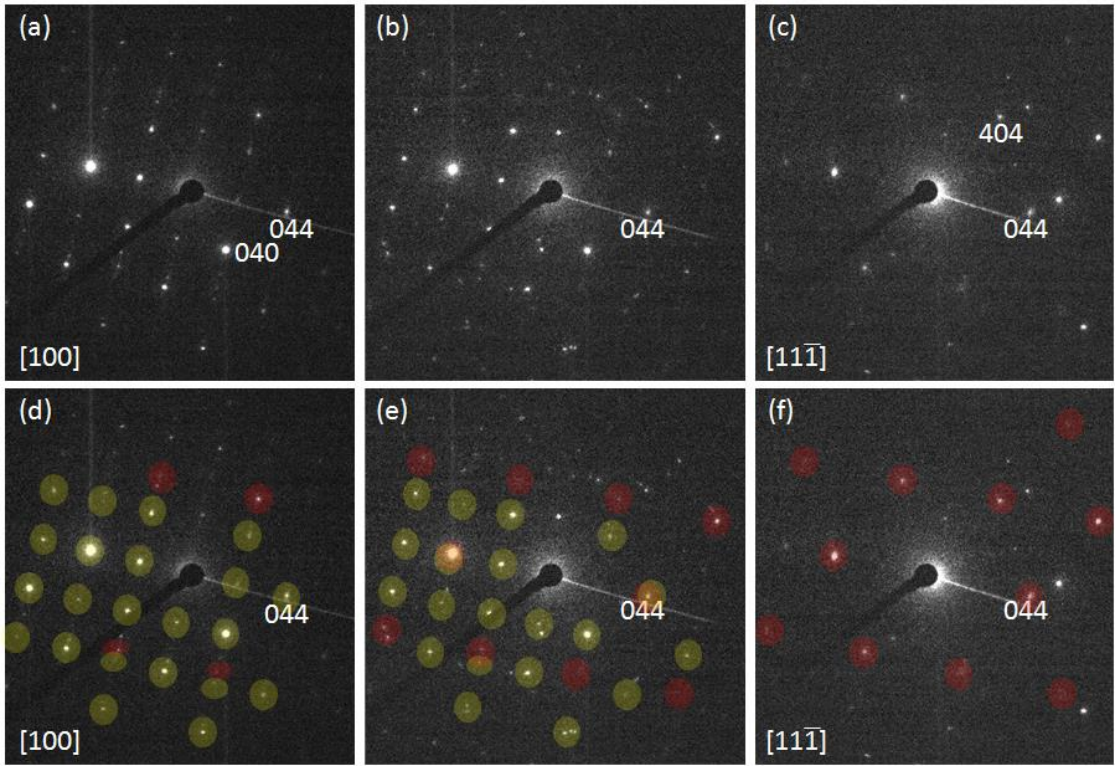

Figure 5.4 TED patterns from the each area marked by black circles in **Figure** 5.3. (a), (b) and (c) correspond to the area a, b and c in Figure 5.3, respectively. All TED patterns were obtained by moving selected area aperture without tilting sample. (d), (e) and (f) are the TED pattern of (a), (b) and (c) with the marks of the diffraction spots of $LiMn_2O_4$ spinel structure with <100> orientation (yellow) and <111> orientation (red).

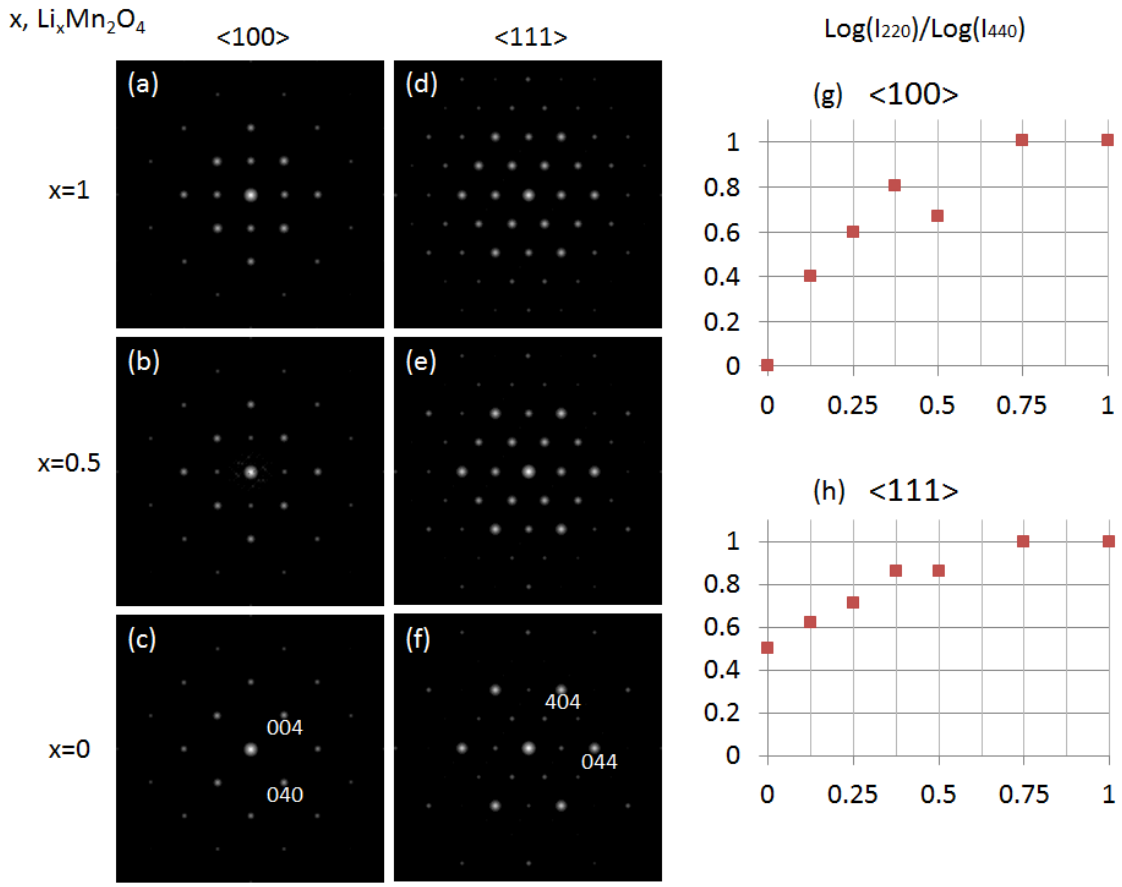

Figure 5.5 Simulated TED patterns of $LiMn_2O_4$ crystals as a function of lithium composition, x in $Li_xMn_2O_4$. The lithium composition, x is 1 for (a)(d), 0.5 for (b)(e) and 0 for (c)(f). The <100> orientation ones are shown in (a)(b)(c) and the <111> orientation ones in (d)(e)(f). The ratio of 220 spot to 440 spot of log scaled intensity ($\log I_{220} / \log I_{440}$) is shown as a function of lithium composition, x, for the <100> orientation in (g), and for the <111> orientation in (h).

In the TED of Figure 5.4 (a), 220 spots are visible, but invisible in the TED of Figure 5.4 (c). We calculated the TED patterns of $Li_xMn_2O_4$ for the cases of x=1, 0.125, 0.25, 0.375, 0.5, 0.75 and 0 in order to investigating the dependence on the lithium composition, x. The sample thickness was 40nm (see Appendix C). The calculation was done by using multi-slice method [95]. The atomic scattering factors were taken from Weikenmeier-Kohl scattering factor.

The calculated TED patterns are shown in Figure 5.5 (a-f). Regardless the view direction, the lithium composition of the range from 1 to 0.5 gives the TED pattern in which 220 spots are clearly visible. However, the 220 spots are very weak when the lithium composition is zero. The ratio of log-scaled intensity of 220 spot to 440 spot ($\log I_{220} / \log I_{440}$) for two orientation ones, <100> and <111>, are shown in Figure 5.5 (g-h) as a function of lithium composition.

Since the experimental TED images (see, Figure A3 in Appendix C) of left area of the boundary (Figure 5.4 a) shows the ratio ($\log I_{220} / \log I_{440}$) of 0.80 ± 0.016, the lithium composition, x, of the left area is estimated as $0.375 < x < 0.75$ by comparison with the calculated results (Figure 5.5 g). The TED of right area of the boundary (Figure 5.4 c) has the ratio less than 0.55 with the assumption that the 220 spot had lower intensity than the background noise level because the 220 spot was not detected. The right area is estimated to have the lithium composition lower than 0.05 by comparison with the calculated results. After TED intensity analysis, we concluded that the left side of the boundary has Li-rich structure, while the right side has Li-poor structure. The lithium composition, x in the Li-rich area is supposed to be in a range $0.375<x<0.75$, while x in the Li-poor area is $x<0.05$ after charge process. Thus, the boundary is the phase boundary (abbreviated hereafter as PB) between the two phases, Li-rich phase and Li-poor phase.

Figure 5.6 shows a series of TEM images of the discharge-charge process. Each TEM image corresponds to each red arrow in Figure 5.2. In the TEM image obtained at 4.0 V (the top-most image in Figure 5.6), the PB is visible as a dark band at the right side of the image (the left-side of the phase boundary is marked by black arrow). In the discharge process (from 4 V to 2.8 V), the PB moved from left to right side, resulting the volume increase of the Li-rich phase. During the charge process, the direction of the PB movement was reversed from the discharge process.

There are three modes of PB movement: translation, expansion and shrinkage. The PB has a width, and its front translates while charge/discharge as a manner shown in Fig.5.6. The PB, in some occasions, expands while the front translates forwards. In another occasion, PB shrinks after the front stops its translation. (In this observation, the detail width change of PB could not be monitored because of limit of view area.)

The relation between the phase boundary movement[2] and the simultaneously measured cyclic voltammogram (CV) is shown in Figure 5.7. The applied voltage change and measured cell current are shown as gray and red lines, respectively. (For guiding of battery reaction current, the background level was marked as red broken lines.) The phase boundary position change is shown as blue markers. The direction of the phase boundary movement toward ILE is noted as (+). Three curves are plotted as functions of time. The deviation of the times measuring CV (voltage and current) and TEM (phase boundary position) is shorter than 5s, which can be ignored in the time scale of Figure 5.7.

[2] In the discharge process, the position change of the left side of the phase boundary (marked by a black arrow in Figure 5.6) was measured. In the charge process, the position change of the right side of the boundary (marked by a white arrow in Figure 5.6) was measured.

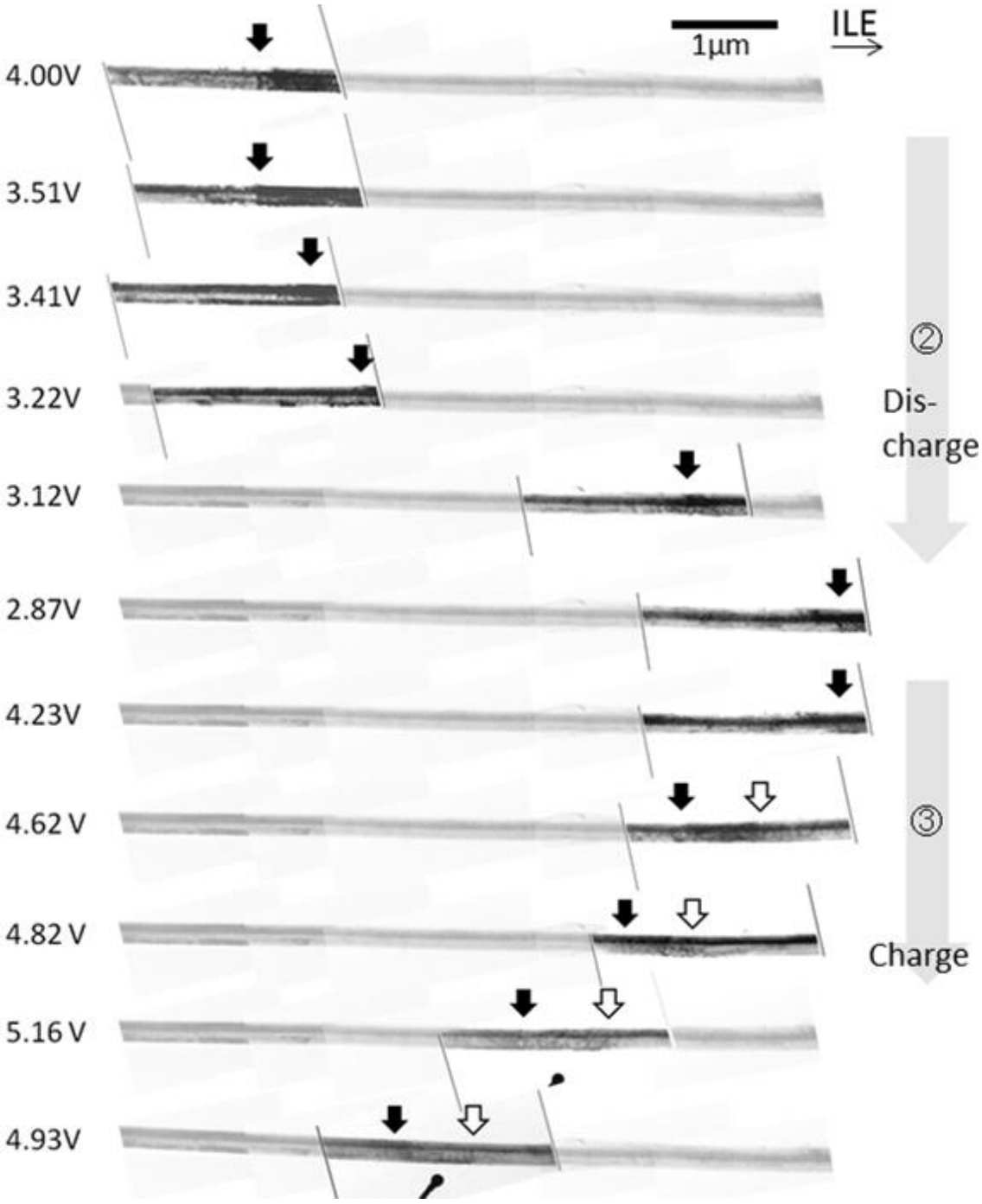

Figure 5.6 The series of TEM images showing phase boundary movement during one discharge-charge cycle. The vivid TEM image was obtained at each voltage. Due to the limit of the view area of one snapshot (~2μm), plural TEM images are superposed (shaded). Black arrows indicate the most left of the phase boundary and white arrows, the most right of the phase boundary. ILE was placed at the right side of the nanowire (far from the observation area by 50 μm).

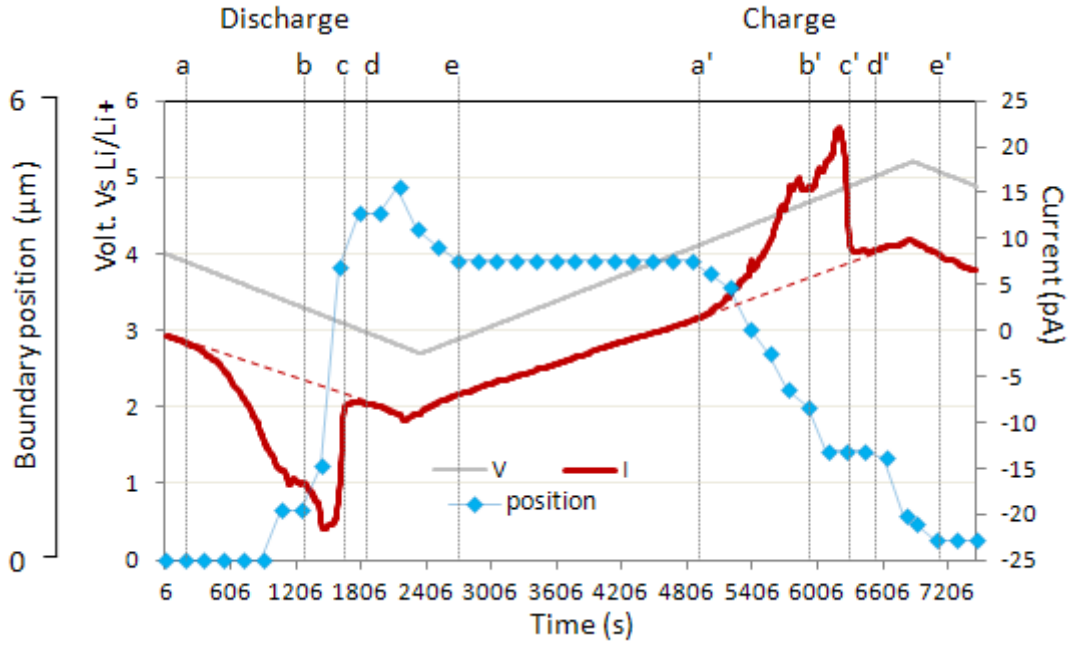

Figure 5.7 The plots of voltage (gray), current (red) and boundary position (blue markers) as functions of time. The displacement of the boundary position toward right-side (toward ILE) is notated as (+). The vertical dotted lines and alphabets are for guide of the stage of the lithium insertion/extraction: a, a', start point of first reaction; b, b', end of first reaction peak; c, c', end of second reaction peak; d, d', elimination point of residual reaction current; e, e', the phase boundary movement stopped. Red broken lines are background level for reaction current.

In the range of **a**-**b** of the discharge process, the phase boundary (PB) started to move 600 s after cathodic current started to flow (stage **a**). And the PB stopped until the stage **b**, which is the saddle point of cathodic current. After the stage **b**, the PB moved drastically, and stopped at the stage **d**, where the cathodic current had stopped flowing. After the stage **d**, the PB moved again, toward ILE and backward. It stopped at the stage **e**.

In the charge process, the PB started to move backward (from ILE to $LiMn_2O_4$ nanowire) at the stage **a'**, where the anodic current started to flow. The PB was still moving at the stage **b'**, which is the saddle point of anodic current. After the stage **b'** the PB stopped moving. Then, the PB moved again after the stage **d'**, where the anodic current did not flow any more. And the PB stopped at the stage **e'**.

In brief summary of Figure 5.7, we found following relation between CV and PB motion. First, the phase boundary started to move during the cathodic or anodic current due to the lithium ion insertion or extraction was flowing. Second, the direction of PB movement reversed as the Li

diffusion direction change, namely, charge process and discharge process. Third, total amount of PB displacement for each of the discharge and of the charge cycle is almost same (4 μm): Compare the PB displacement for **a-e** and one for **a'-e'**. Forth, in correlation with the CV, PB (seems to move) moved in step-wise for each stages of **a-b** (**a'-b'**) and **b-e** (**b'-e'**). Fifth, the phase boundary movement did not directly correspond to the lithium movement: although PB displacement in **a-b** (0.6 μm) is almost the same as the one in **b'-d'**, the displacement in **b-d** (4 μm) is larger than the one in **a'-b'** (2 μm). Finally, there is time-lag from the point where reaction current died down (**d** and **d'**) to the point where the phase boundary stopped (e and e').

5.4 Discussion

5.4.1 Quantitative comparison between CV and TEM

In charge process, though the anodic current died down at the stage **d'**, the PB continued to move until the stage **e'** in Figure 7. The anodic current reflects the lithium extraction from nanowire to ILE. From the stage **d'**, average lithium composition in nanowire would be constant. The PB movement is due to phase transformation between Li-rich and Li-poor. It imposes that the observed phase boundary movement could not be the rate-limit stage for charge/discharge process (lithium insertion/extraction). There are two possible reasons to explain the time lag about 600s between the current change and the PB movement. One is that the phase transformation can occur after lithium composition changed with time delay as an analogy of time-temperature-transformation relation of eutectoid steels, in which phase transformation occurs with time delay after the temperature change due to the exist of interface energy. Since the most different point between Li-rich phase and Li-poor phase is whether lithium ions are present or not (it was determined from TED patterns), this reason is hardly acceptable. The other one is the inhomogeneous distribution of lithium concentration: right after the charge process, local difference of lithium concentration could be present with some reasons which are unclear; it could make the redistribution of lithium ions inside the nanowire, resulting in the further movement of the phase boundary.

The obtained anodic current peak in CV was about 15 pA (=15 pC/s). It corresponds that 9.4 x 10^7 Li ions were extracted from $LiMn_2O_4$ nanowire in every second. Since 8 Li ions can be contained in unit cell volume, (8.245 A) ^{3}, for cubic $Li_xMn_2O_4$ as maximum solubility, 15 pA corresponds that all Li ions from the volume of 6.6 x 10^6 nm^3 should be removed in every second. With the approximation of the shape of nanowire as a cylinder whose diameter is about 200nm, the PB should move with the velocity of about 200 nm/s. However, the measured

highest instantaneous velocity of the phase boundary movement was about 15 nm/s. It is more than 10 times slower compared with the expected velocity, 200 nm/s, which was estimated from CV.

The charge capacity was estimated to be about 9 nC from CV. During charge, the phase boundary moved about 4 μm. If the Li-rich phase had the lithium composition of x=1 which is the highest Li composition for cubic phase, and the Li-poor phase had the lithium composition of x=0 which is the lowest Li composition, the corresponding capacity from the PB movement of about 4 μm is about 0.3 nC. It is 30 times smaller than the capacity from CV.

The possible reasons for these quantitative inconsistency can be considered as follows. First, the existence of the other Li host places such binder, additive or surface area, etc. can be considered. If lithium insertion/extraction reaction occurred at the other host places, it should be reflected by the appearance of different reaction voltage from the 4 volt double peak of $LiMn_2O_4$. Because the reaction voltage is dependent on the circumstantial structure and chemical elements. However, obtained CV shows no additional reaction voltage.

Second possible reason is that the PB movement non-related with lithium insertion/extraction was observed. However, the observed PB movement shows the strong correlation with Li flow: The direction of PB movement reversed as the Li diffusion direction change, namely, charge process and discharge process. And the PB started move when the current due to Li diffusion flowed.

Third possible reason is that the number of the PB was not single, but plural: the phase transformation occurred not only at the observed area, but also at another positions, simultaneously. If the number of PBs were 30, the cell capacity of 9 nC obtained from CV can be covered by same PB movement. And if plural PBs moved simultaneously, the inconsistency of PB velocity between 15nm/s (measured from TEM observation) and 200nm/s (estimated from CV) could be explained. Since the view area of one snapshot of TEM image (~2 μm) is still smaller than the length of the nanowire (~170 μm), the phase transformation at plural positions can be expected. Thus, the model of simultaneous phase transformation at plural positins, *multi-PBs model*, is most probable scenario based on the observed TEM and CV results.

5.4.2 Multi-PBs model

The observed area was apart from the $LiMn_2O_4$/ILE interface by about 50 μm. Since the observed area was not covered by ILE layer, lithium ions should be inserted or extracted through the cross section of $LiMn_2O_4$ nanowire in right-side of observed area.

Based on multi-PBs model in which plural Li-rich and Li-poor phases are placed alternately,

there are two patterns to explain the phase transformation. One is that the PBs moved in sequence from the $LiMn_2O_4$/ILE interface to bulk-side of $LiMn_2O_4$: after one PB which is close to the $LiMn_2O_4$/ILE interface stops moving, next PB starts to move. The other is that plural PBs move simultaneously. Since the observed PB moved at the stage **a'** during charge process without delay time from the anodic current change, the first model, PB movement in sequence is not suitable. The model which is coincident with the observed PB movement is the *simultaneous moving* multi-PB model, even though it is not understood how to move lithium ions in local lithium composition distribution: lithium ions should diffuse through the area of sequence of Li-poor phase and Li-rich phase.

With the assumption that lithium can move regardless of local lithium concentration distribution, the possible phase transformation model in our study is as follows: During the discharge-charge cycle, lithium ions would flow throughout the nanowire causing overall composition change. The composition change induced the phase transform at plural positions simultaneously and the volume fraction between Li-rich and Li-poor phases changes by moving the PBs with time delay due to the inhomogeneous lithium distribution.

5.4.3 Comparative study with the reported phase transformation of $Li_xMn_2O_4$

In-situ XRD study has reported the phase transition during discharge process of $Li_xMn_2O_4$ ($0<x<1$) by monitoring the (111) XRD peak [59]. The lattice parameter changed in following manner: in the region 0-10% state of discharge (SOD), only one phase was monitored to expand its lattice parameter (from 8.07A to ~8.09A). In the region 10-35% SOD, two different-lattice-parameter phases appeared (~8.09A and ~8.14A). As discharge proceeded, the fraction of larger-lattice phase increased linearly, while the fraction of smaller-lattice phase decreased linearly. In the region 35-100% SOD, only larger-lattice phase was remained, and expanded its lattice parameter (from ~8.14A to 8.249A).

Based on the reported in-situ XRD study, our observed Li-rich and Li-poor phases could correspond to the phase transformation with two phases in the region 10-35% SOD. However, in our results, Li-rich phase and Li-poor phase were remained during whole charge-discharge process. For the time between discharge process and sequence charge process, about 50min, the PB did not disappear. This discrepancy is considered due to the experimental condition: in-situ XRD study was performed with C/10 and 0.08 mA/cm^3, while our results was obtained under higher charge rate, in which the peak anodic current corresponds to instantaneously 6 C and 50 mA/cm^3. The relaxation time would not be enough to make system in the equilibrium state in this study.

In-situ XRD study reported that no XRD peak broadening due to concentration and/or phase gradients was detected [59]. They concluded that phase boundary movement can be excluded as the rate-limiting step. In our study, the in-situ TEM images directly showed that lithium ion movement is not limited by the phase boundary movement.

Simulation studies have reported that ordering phase of $Li_{0.5}Mn_2O_4$ crystal, which should make 200 spot visible [120,121]. And another simulation study has reported the ordered structures, 3x3x3 superlattice at x=0.5 and 7x7x7 superlattice at x=0 in $Li_xMn_2O_4$ [122]. However, in this study, any superlattice spots and 200 spot were not detected.

5.5 Summary

In-situ TEM observation of a single $LiMn_2O_4$ nanowire battery was performed under several tens mA/cm^3 current density (<50 mA/cm^3). We observed the phase boundary movement due to the phase transformation between Li-rich and Li-poor phases. We found that the phase boundary moved with about 10 times slower velocity than the expected boundary velocity from the simultaneously measured cyclic voltammogram (CV). The estimated capacity from the boundary movement was 30 times smaller than that from CV. And there was time delay from the point where the cathodic or anodic current died down to the point where the phase boundary stopped moving. The phase transformation between Li-rich and Li-poor phases is considered to occur at many positions along the nanowire simultaneously and be completed with the time delay. The time delay is considered due to the redistribution of inhomogeneous lithium concentration inside the nanowire right after charge/discharge process. Based on this analysis, we conclude that lithium ions diffusion is not limited by the phase transformation, even though the lithium diffusion process through the inhomogeneous lithium distributed nanowire is not clarified.

Chapter 6. Concluding remarks and Future vision

This study has been performed to clarify the deterioration mechanism of $LiMn_2O_4$ crystals during battery cycles by *in-situ* TEM observation. In order to obtain new knowledge of local lithium diffusion behavior by *in-situ* observation, (1) imaging method, (2) subject to image (nano-battery) and (3) charge/discharge able environment should be developed. Thus, this thesis consists of two parts: methodology (chapter 2, 3) and material science (chapter 4, 5).

A short summary of each part is as follow,

I. Methodology:

1. ABF image is a potential image, which visualizes the potential change in a sample, such as Li ion movement.
2. Surface profile including an ion vacancy can be monitored by using large convergent ABF imaging which gives surface sensitive contrast due to the narrower depth of focus.
3. For *in-situ* EM observation, nano-batteries have been developed with the construction of $LiMn_2O_4$ nanowires cathode, ionic liquid electrolyte and $Li_4Ti_5O_{12}$ anode.
4. The *in-situ* EM observation system including sample holder was developed. It enables to measure the electrochemical properties (I-V curve) of pA-order current level of nano-batteries.

II. Lithium diffusion behavior in $LiMn_2O_4$:

5. During the early stage (3.9V) of the discharge process of 4 V reaction, the cubic $LiMn_2O_4$ at the interface area with electrolyte changed into tetragonal phase through orthorhombic structure.
    1. The tetragonal phase is considered to appear by Li accumulation at the interface area due to higher Li insertion rate from electrolyte than the rate of Li diffusion inside $LiMn_2O_4$ nanowire.
6. For nanowire $LiMn_2O_4$ cathode, the tetragonal phase was changed into cubic phase reversibly during sequence charge process without physical fracture.
    1. Robustness of $LiMn_2O_4$ nanowires during the phase transformation shows the possibility of twice larger capacity ($0<x<2$, $Li_xMn_2O_4$)
7. At the bulk side (far from ILE), it was observed the delay in stopping the phase boundary movement between Li-rich and Li-poor phases from the cathodic or anodic current changing in cyclic voltammogram (CV) due to lithium insertion or extraction. The charge capacity estimated from phase boundary movement was 30 times smaller than that estimated from CV.

1. Under non-equilibrium state, the structure change can be delayed from the net current change which reflects the lithium insertion/extraction. It is considered due to the redistribution of local inhomogeneity of lithium composition.

Based on these conclusions, this study suggests that to make the 1-D like morphology prevent the capacity fade out during fast charge/discharge cycles: Nanowire shape makes $LiMn_2O_4$ overcome the severe volume change due to the transformation to tetragonal phase. The geometry of nanowires soaked in electrolyte for common battery allow short lithium diffusion path, which would allow the local lithium concentration become the average lithium concentration instantly using fast lithium movement. These features would be suitable not only for long-life and fast chargeable battery cathode materials but also super capacitor. In aspect of engineering, the remained task is how to make the $LiMn_2O_4$ nanowire with simple process and low cost. And if the pure lithium diffusion velocity in $LiMn_2O_4$ on a micro scale is determined, it must be important factor for battery design.

In aspect of science, the combination of macro measurement (CV) and micro measurement (TEM) is an interesting approach. By collaboration of *in-situ* diffraction methods such as XRD and neutron diffraction, dynamics of lithium diffusion can be revealed.

In addition, the visualization of lithium diffusion at the atomic scale during charge/discharge cycles has not been succeeded unfortunately, however such observation is expected to be performed and to reveal the pure lithium diffusion mechanism in cathode materials in near future.

Reference

[1] J. M. Tarascon, M. Armand, *Nature* **414**, 359 (2001)

[2] A. D. Pasquier, I. Plitz, S. Menocal, G. Amatucci, *J. Power Sources* **115**, 171 (2003)

[3] E. Karden, S. Ploumen, B. Fricke, T. Miller, K. Snyder, *J. Power Sources* **168**, 2 (2007)

[4] M. Armand, J. M. Tarascon, *Nature* **451**, 652 (2008)

[5] B. Scrosati, J. Garche, *J. Power Sources* **195**, 2419 (2010)

[6] J. B. Goodenough, Y. Kim, *Chem. Mater.* **22**, 587 (2010)

[7] D. Aurbach, A. Zaban, Y. Ein-Eli, I. Weissman, O. Chusid, B. Markovsky, M. Levi, E. Levi, A. Schechter, E. Granot, *J. Power Sources* **68**, 91 (1997)

[8] K. Mizushima, P. C. Jones, P. J. Wiseman, J. B. Goodenough, *Mat. Res. Bull.* **15**, 783 (1980)

[9] T. Ohzuku, Y. Makimura, *Chem. Lett.* **30**, 642 (2001)

[10] A. K. Padhi, K. S. Nanjundaswamy, C. Masquelier, S. Okada, J. B. Goodenough, *J. Electrochem. Soc.* **144**, 1609 (1997).

[11] A. K. Padhi, K. S. Nanjundaswamy, J. B. Goodenough, *J. Electrochem. Soc.* **144**, 1188 (1997)

[12] K. Amine, H. Yasuda, M. Yamaji, *Electrochem. Solid stat.* **3**, 178 (2000)

[13] M. M. Thackeray, P. J. Johnson, L. A. Picciotto, P. G. Bruce, J. B. Goodenough, *Mat. Res. Bull.* **19**, 179 (1984)

[14] C. Sigala, D. Guyomard, A. Verbaere, Y. Piffard, M. Touroux, *Solid State Ionics* **81**, 167 (1995)

[15] K. Amine, H. Tsukamoto, H. Yasuda, Y. Fujita, *J. Power Sources* **68**, 604 (1997)

[16] Y. Ein-Eli, W. F. Howard, H. L. Sharon, S. Mukerjee, J. McBreen, J. T. Vaughey, M. Thackeray, *J. Electrochem. Soc.* **145**, 1238 (1998)

[17] Q. Zhong, A. Bonakdarpour, M. Zhang, Y. Gao, J. R. Dahn, *J. Electrochem. Soc.* **144**, 205 (1997)

[18] F. Jiao, J. Bao, A. H. Hill, P. G. Bruce, *Angew. Chem. Int . Ed.* **120**, 9857 (2008)

[19] F. Jiao, K. M. Shaju, P. G. Bruce, *Angew. Chem. Int. Ed.* **44**, 6550 (2005)

[20] E. Hosono, T. Kudo, I. Honma, H. Matsuda, H. Zhou, *NanoLetters* **9**, 1045 (2009)

[21] H. W. Lee, P. Muralidharan, R. Ruffo, C. M. Mari, Y. Cui, D. K. Kim, *NanoLetters* **10**, 3852 (2010)

[22] C. H. Chen, J. Liu, K. Amine, *J. Power Sources* **96**, 321 (2001)

[23] M. Itagaki, N. Kobari, S. Yotsuda, K. Watanabe, S. Kinoshita, M. Ue, *J. Power Sources* **135**, 255 (2004)

[24] J. Li, X. Xiao, F. Yang, M. W. Verbrugge, Y.-T. Cheng, *J. Phys. Chem. C* **116**, 1472 (2012)

[25] D. Aurbach, B. Markovsky, I. Weissman, E. Levi, Y. Ein-Eli, *Electrochimica Acta* **45**, 67 (1999)

[26] M. Odziemkowski, M. Krell, D. E. Irish, *J. Electrochem. Soc.* **139**, 3052 (1992)

[27] D. Aurbach, Y. Ein-Eli, B. Markovsky, A. Zaban, *J. Electrochem. Soc.* **142**, 2882 (1995)

[28] K. Kanamura, H. Tamura, S. Shiraishi, Z. Takehara, *J. Electrochem. Soc.* **142**, 340 (1995)

[29] H. L. Zhang, F. Li, C. Liu, J. Tan, H. M. Cheng, *J. Phys. Chem. B.* **109**, 22205 (2005).

[30] F. Wang, J. Graetz, M. S. Moreno, C. Ma, L. Wu, V. Volkov, Y. Zhu, *ACS Nano* **5**, 1190 (2011)

[31] D. Aurbach, Y. Ein-Eli, *J. Electrochem. Soc.* **142**, 1746 (1995)

[32] M. Hirayama, H. Ido, K. Kim, W. Cho, K. Tamura, J. Mizuki, R. Kanno, *J. Am. Chem. Soc.* **132**, 15268 (2010)

[33] J. Kim, K. Kim, W. Cho, W. Shin, R. Kanno, J. Choi, *Nano Lett.* **12**, 6358 (2012)

[34] F. Orsini, A. D. Pasquier, B. Beaudoin, J. M. Tarascon, M. Trentin, N. Langenhuizen, E. D. Beer, P. Notten, *J. Power Sources* **76**, 19 (1998)

[35] M. Morcrette, P. Rozier, L. Dupont, E. Mugnier, L. Sannier, J. Galy, J. M. Tarascon, *Nature Mater.* **2**, 755 (2003).

[36] M. M. Thackeray, Y. Shao-Horn, A. J. Kahaian, D. Kepler, E. Skinner, J. T. Vaughey, S. A. Hackney, *Electrochem. Solid Stat.* **1**, 7 (1998)

[37] Y. Shao-Horn, S. A. Hackney, A. J. Kahaian, K. D. Kepler, E. Skinner, J. T. Vaughey, M. M. Thackeray, *J. Power Sources* **81**, 496 (1999)

[38] R.J. Gummow, A. D. Kock, M. M. Thackeray, *Solid State Ionics* **69**, 59 (1994).

[39] S. Muto, Y. Sasano, K. Tatsumi, T. Sasaki, K. Horibuchi, Y. Takeuchi, Y. Ukyo, *J. Electrochem. Soc.* **156**, A371 (2009)

[40] J. Y. Huang, L. Zhong, C. M. Wang, J. P. Sullivan, W. Xu, L. Q. Zhang, S. X. Mao, N. S. Hudak, X. H. Liu, A. Subramanian, H. Fan, L. Qi, A. Kushima, J. Li, *Science* **330**, 1515 (2010)

[41] C. M. Wang, W. Xu, J. Liu, J. G. Zhang, L. V. Saraf, B. W. Arey, D. Choi, Z. G. Yang, J. Xiao, S. Thevuthasan, D. R. Baer, *Nano Lett.* **11**, 1874 (2011)

[42] X. H. Liu, L. Q. Zhang, L. Zhong, Y. Liu, H. Zheng, J. W. Wang, J. H. Cho, S. A. Dayeh, S. T. Picraux, J. P. Sullivan, S. X. Mao, Z. Z. Ye, J. Y. Huang, *Nano Lett.***11**, 2251 (2011)

[43] X. H. Liu, H. Zheng, L. Zhong, S. Huang, K. Karki, L. Q. Zhang, Y. Liu, A. Kushima, W. T. Liang, J. W. Wang, J. H. Cho, E. Epstein, S. A. Dayeh, S. T. Picraux, T. Zhu, J. Li, J. P. Sullivan, J. Cumings, C. Wang, S. X. Mao, Z. Z. Ye, S. Zhang, J. Y. Huang *Nano Lett.* **11**, 3312 (2011)

[44] X. H. Liu, S. Huang, S. T. Picraux, J. Li, T. Zhu, J. Y. Huang, *Nano Lett.* **11**, 3991 (2011)

[45] Y. Liu, N. S. Hudak, D. L. Huber, S. J. Limmer, J. P. Sullivan, J. Y. Huang, *Nano Lett.***11**, 4188 (2011)

[46] C. M. Wang, X. Li, Z. Wang, W. Xu, J. Liu, F. Gao, L. Kovarik, J. G. Zhang, J. Howe, D. J. Burton, Z. Liu, X. Xiao, S. Thevuthasan, D.R. Baer, *Nano Lett.* **12**, 1624 (2012)

[47] M. T. McDowell, I. Ryu, S. W. Lee, C. Wang, W. D. Nix, Y. Cui, *Adv. Mater.* **24**, 6034 (2012)

[48] F. Wang, H. C. Yu, M. H. Chen, L. Wu, N. Pereira, K. Thornton, A. Ven, Y. Zhu, G. Amatucci, J. Graetz, *Nat. Commun.* **3**, 1201 (2012)

[49] M. T. McDowell, S. W. Lee, J. T. Harris, B. A. Korgel, C. Wang, W. D. Nix, Y. Cui, *Nano Lett.* **13**, 758 (2013)

[50] J. Vetter, P. Novak, M. R. Wagner, C. Veit, K.-C. Moller, J. O. Besenhard, M. Winter, M. Wohlfahrt-Mehrens, C. Vogler, A. Hammouche, *J. Power Sources* **147**, 269 (2005)

[51] H. Arai, S. Okada, H. Ohtsuka, M. Ichimura, J. Yamaki, *Solid State Ionics* **80**, 261 (1995)

[52] D. P. Abraham, R. D. Twesten, M. Balasubramanian, J. Kropf, D. Fischer, J. McBreen, I. Petrov, K. Amine, *J. Electrochem. Soc.* **150**, A1450 (2003)

[53] D. H. Jang, Y. J. Shin, S. M. Oh, *J. Electrochem. Soc.* **143**, 2204 (1996)

[54] Y. J. Shin, A. Manthiram, *Electrochem. Solid Stat*. **5**, A55 (2002)

[55] L. A. Picciotto, M. M. Thackeray, *Mater. Res. Bull.* **20**, 1409 (1985)

[56] W. David, M. Thackeray, L. Picciotto, J. Goodenough, *J. Solid State Chem.* **67**, 316 (1987)

[57] K. Tateishi, D. Boulay, N. Ishizawa, K. Kawamura, *J. Solid State Chem.* **174**, 175 (2003)

[58] M. M. Thackeray, W. I. F. David, P. G. Bruce, J. B. Goodenough, *Mat. Res. Bull.* **18**, 461 (1983)

[59] T. Eriksson, A-K. Hjelm, G. Lindbergh, T. Gustafsson, *J. Electrochem. Soc.***149**, A1164 (2002)

[60] W. Liu, K. Kowal, G. C. Farrington, *J. Electrochem. Soc.* **145**, 459 (1998)

[61] T. Kudo, M. Hibino, *Electrochim. Acta* **43**, 781(1998).

[62] H. Abiko, M. Hibino, T. Kudo, Electrochem. Solid State Lett., 1, 114(1998).

[63] A. Van der Ven, C. Marianetti, D. Morgan, G. Ceder, Solid State Ionics, 135, 21(2000).

[64] R. Darling , J. Newman, *J. Electrochem. Soc.* **146**, 3765 (1999)

[65] S. W. Kim, S. I. Pyun, *Electrochim. Acta* **46**, 987 (2001)

[66] B. Ammundsen, G. R. Burns, M. S. Islam, H. Kanoh, J. Roziere, J. Phys.Chem. B 103, 5175 (1999)

[67] Y. Gao, J. N. Reimers, J. R. Dahn, *Phys. Rev. B* **54**, 3878 (1996)

[68] http://home.utad.pt/~cqvr/ceramicos

[69] D. H. Jang, S. M. Oh, *J. Electrochem. Soc.* **144**, 3342 (1997)

[70] Y. Shin, A. Manthiram, *J. Electrochem. Soc.* **151**, A204 (2004)

[71] J. M. Tarascon, W. R. McKinnon, F. Coowar, T. N. Bowmer, G. Amatucci, D. Guyomard, *J. Electrochem. Soc.* **141**, 1421 (1994)

[72] A. Blyr, C. Sigala, G. G. Amatucci, D. Guyomard,Y. Chabres, J. M. Tarascon, *J. Electrochem. Soc.* **145**, 194 (1998).

[73] Y. Oshima, H. Sawada, F. Hosokawa, E. Okunishi, T. Kaneyama, Y. Kondo, S. Niitaka, H. Takagi, Y. Tanishiro, K. Takayanagi, *J. Electron Microsc.* **59**, 457 (2010)

[74] R. Huang, Y. H. Ikuhara, T. Mizoguchi, S. D. Findlay, A. Kuwabara, C. A. Fisher, H. Moriwake, H. Oki, T. Hirayama, Y. Ikuhara, *Angew. Chem. Int . Ed.* **50**, 3053 (2011)

[75] R. Huang, T. Hitosugi, S. D. Findlay, C. A. J. Fisher, Y. H. Ikuhara, H. Moriwake, H. Oki, Y. Ikuhara, *Appl. Phys. Lett.* **98**, 051913 (2011)

[76] L. Gu, C. Zhu, H. Li, Y. Yu, C. Li, S. Tsukimoto, J. Maier, Y. Ikuhara, *J. Am. Chem. Soc.* **133**, 4661 (2011)

[77] S. D. Findlay, N. Shibata, H. Sawada, E. Okunishi, Y. Kondo, Y. Ikuhara, *Ultramicroscopy* **110**, 903 (2010)

[78] E. Okunishi, H. Sawada, Y. Kondo, *Micron* **43**, 538 (2012)

[79] H. Rose, *Optik* **85**, 19 (1990).

[80] M. Haider, S. Uhlemann, E. Schwan, H. Rose, B. Kabius, K. Urban, *Nature* **392**, 768 (1998)

[81] O. L. Krivanek, N. Dellby, A. R. Lupini, *Ultramicroscopy* **78**, 1 (1999).

[82] H. Sawada, Y. Tanishiro, N. Ohashi, T. Tomita, F. Hosokawa, T. Kaneyama, Y. Kondo, K. Takayanagi, *J. Elec. Micro*. **58**, 357 (2009)

[83] J. Cowley, "Diffraction physics", 3rd edition, Elsevier, North-Holland, 1995.

[84] S. Lee, Y. Oshima, H. Sawada, F. Hosokawa, E. Okunishi, T. Kaneyama, Y. Kondo, S. Niitaka, H. Takagi, Y. Tanishiro, K. Takayanagi, *J. Appl. Phys.* **109**, 113530 (2011)

[85] J. M. Cowley, *Ultramicroscopy* **49**, 4 (1993)

[86] T. Yamamoto, A. Chartier, K. Yasuda, C. Meis, K. Shiiyama, S. Matsumura, *Nucl. Instrum. Methods Phys. Res., Sect. B* **266**, 2676 (2008)

[87] A. Hightower, C. C. Ahn, B. Fultz, *Appl. Phys. Lett.* **77**, 238 (2000)

[88] C. Delmas, M. Maccario, L. Croguennec, F. Le Cras, F. Weill, *Nat. Mater.* **7**, 665 (2008)

[89] S. Nishimura, G. Kobayashi, K. Ohoyama, R. Kanno, M. Yashima, A. Yamada, *Nat. Mater.* **7**, 707 (2008)

[90] C. K. Chan, H. Peng, G. Liu, K. McIlwrath, X.-F. Zhang, R. A. Huggins, Y. Cui, *Nat. Nanotechnol.* **3**, 31 (2008)

[91] B. Key, R. Bhattacharyya, M. Morcrette, V. Seznec, J.-M. Tarascon, C. P. Grey, *J. Am. Chem. Soc.* **131**, 9239 (2009)

[92] L.Reimer, "Transmission Electron Microscopy", Springer, Berlin, 1997.

[93] D. O. Klenov, S. Stemmer, *Jpn. J. Appl. Phys.* **45**, L602 (2006)

[94] K. Benthem, A. R. Lupini, M. P. Oxley, S. D. Findlay, L. J. Allen, S. J. Pennycook, *Ultramicroscopy* **106**, 1062 (2006)

[95] K.Ishizuka,*Ultramicroscopy* **90**, 71 (2002)

[96] M. Yonemura, A. Yamada, H. Kobayashi, M. Tabuchi, T. Kamiyama, Y. Kawamoto, R. Kanno, *J. Mater. Chem.* **14**, 1948 (2004).

[97] S. Kim, Y. Oshima, H. Sawada, T. Kaneyama, Y. Kondo, M. Takeguchi, Y. Nakayama, Y. Tanishiro, K. Takayanagi, *J. Electron Microsc.* **60**, 109 (2011).

[98] H. Sawada, T. Sannomiya, F. Hosokawa, T. Nakamichi, T. Kaneyama, T. Tomita, Y. Kondo, T. Tanaka, Y. Oshima, Y. Tanishiro, K. Takayanagi, *Ultramicroscopy* **108**, 1467 (2008).

[99] P. C. Tiemeijer, M. Bischoff, B. Freitag, C. Kisielowski, *EMC 2008 14th Euro. Microsc.*

Congress **1-5**, **I1 I2**, 53-54 (2008).

[100] P. C. Tiemeijer, M. Bischoff, B. Freitag, C. Kisielowski, *Ultramicroscopy* **114**, 72 (2012).

[101] P. Hartel, H. Muller, S. Uhlemann, J. Zach, U. Lobau, R. Hoschen, M. Haider, *EMC 2008 14th Euro. Microsc. Congress* 1-5, **I1 I1**.1, 27-28 (2008).

[102] B. Kabius, P. Hartel, M. Haider, H. Muller, S. Uhlemann, U. Loebau, J. Zach, H. Rose, *J. Electron Microsc.* **58**, 147 (2009).

[103] H. Sawada, F. Hosokawa, T. Sasaki, S. Yuasa, M. Kawazoe, M. Terao, T. Kaneyama, Y. Kondo, K. Kimoto, K. Suenaga, *Microsc. Microanal.* **17** (Suppl 2), 1184 (2011).

[104] T. Ohzuku, A. Ueda, N. Yamamoto, *J. Electrochem. Soc.* **142**, 1431 (1995)

[105] S. Scharner, W. Weppenr, P. Schmid-Beurmann, *J. Electrochem. Soc.* **146**, 857 (1999)

[106] T. Welton, *Chem. Rev.* **99**, 2071 (1999)

[107] J. Fu, *Solid State Ionics* **96**, 195 (1997)

[108] http://www.ohara-inc.co.jp/jp/product/electronics/licgc.html

[109] H. Sakaebe, H. Matsumoto, *Electrochem. Commun.* **5**, 594 (2003)

[110] D. H. Buckley, "Surface effects in adhesion, friction, wear, and lubrication", Elsevier (1981)

[111] Y. An, P. Zuo, X. Cheng, L. Liao, G. Yin, *Electrochim. Acta* **56**, 4841 (2011)

[112] M. Wakihara, L. Guohua, H. Ikuta, T. Uchida, *Solid State Ionics* 86-88, 907 (1996)

[113] M. M. Thackeray, *J. Am. Ceram. Soc.* **82**, 3347 (1999)

[114] X. Sun, X. Yang, M. Balasubramanian, J. McBreen, Y. Xi, T. Sakai, *J. Electrochem. Soc.* **149**, A842 (2002)

[115] A. Yamada, K. Miura, K. Hinokuma, M. Tanaka, *J. Electrochem. Soc.* **142**, 2149 (1995)

[116] W. weppner and R.A. Huggins, *J. Electrochem. Soc.* **124**, 1569 (1977)

[117] C. John Wen, B. A. Boukamp, R. A. Huggins W. Weppner, *J. Electrochem. Soc.* **126**, 2258 (1979)

[118] M. D. Levi, K. Gamolsky, D. Aurbach, U. Heider, R. Oesten, *J. Electrochem. Soc.* **147**, 25 (2000)

[119] M. Okubo, Y. Mizuno, H. Yamada, J. Kim, E. Hosono, *ACS Nano* **4**, 741(2010)

[120] Y. Gao, J. N. Reimers, J. R. Dahn, *Phys. Rev. B* **54**, 3878 (1996)

[121] R. Darling, J. Newman, *J. Electrochem. Soc.* **146,** 3765–3772 (1999)

[122] H. Bjork, T. Gustafsson, J. O. Thomas, *Electrochem. Commun.* **3**, 187 (2001)

APPENDIX A. Construction of nanowire battery

The nanowire battery was fabricated on the special sample stage for developed *in-situ* TEM observation holder. The prepared $Li_4Ti_5O_{12}$ anode was cut into 2mm x 2mm size and set one side of the stage. On the $Li_4Ti_5O_{12}$ anode, the slurry of ionic liquid electrolyte and OHARA sheet powder was painted. On the opposite side, platinum current collector was set. Both were attached by silver conductive paste. After that, $LiMn_2O_4$ nanowires are picked up by micro-manipulator (**Figure** A1) and bridged both side. In most cases, more than two nanowires connect each other and make the bridge between platinum and $Li_4Ti_5O_{12}$ anode side. Sometimes, only one nanowire which is long enough bridge between two sides.

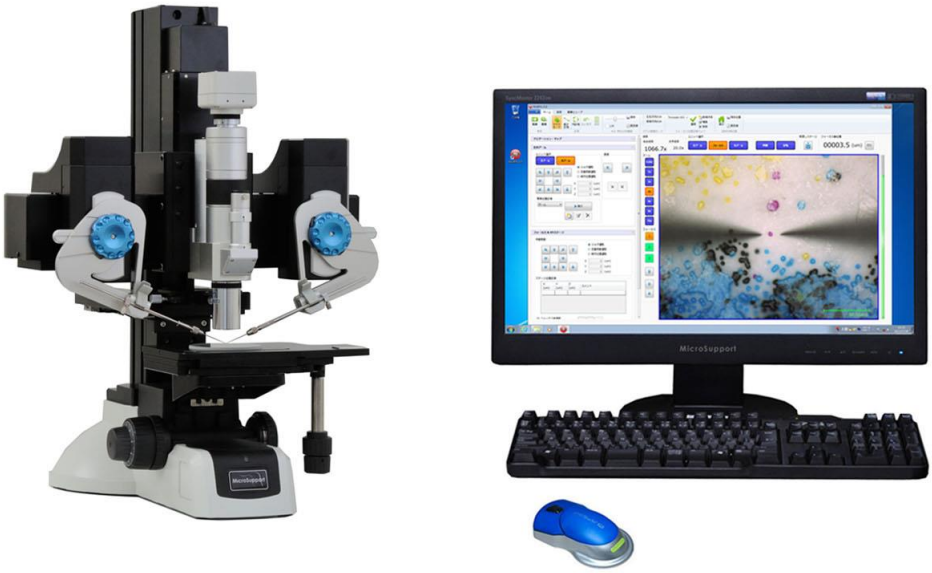

Figure A1 The image of micro-manipulator (Axis pro, Microsupport. Co.)

APPENDIX B. Lattice parameter for each stage of $Li_xMn_2O_4$

Table A1. Lattice parameter for each stage of $Li_xMn_2O_4$ nanowire in **Figure** 4.5

① 3.90 V			a=8.30 Å	
			Exp.	Cal.
h	k	l	d (Å)	d (Å)
2	0	0	4.149	4.150
3	1	1	2.500	2.503
4	0	0	2.075	2.075
3	3	1	1.912	1.904
5	3	1	1.401	1.403
6	0	0	1.383	1.383
6	2	0	1.323	1.312
6	2	2	1.256	1.251
6	4	2	1.114	1.109
7	3	1	1.079	1.081
8	0	0	1.037	1.038

② 5.47 V			a=8.22 Å	
			Exp.	Cal.
h	k	l	d (Å)	d (Å)
2	2	0	2.959	2.906
4	0	0	2.053	2.055
4	4	0	1.462	1.453
6	2	0	1.295	1.300
8	0	0	1.027	1.028

③ 3.51 V			a=5.57 Å	c=8.71 Å
			Exp.	Cal.
h	k	l	d (Å)	d (Å)
1	0	1	4.717	4.691
1	1	0	3.937	3.939
1	1	2	2.915	2.920
2	1	1	2.469	2.395

2	0	2	2.358	2.345
2	2	0	1.905	1.969
3	1	2	1.637	1.633
3	0	3	1.572	1.564
2	2	4	1.458	1.460
3	1	4	1.370	1.369
3	2	5	1.155	1.155

④ 5.33 V			a=8.30 Å	
			Exp.	Cal.
h	k	l	d (Å)	d (Å)
2	2	0	2.937	2.934
4	0	0	2.075	2.075
4	4	0	1.470	1.467
8	0	0	1.037	1.038

Table A2 Lattice parameter of $Li_xMn_2O_4$ nanowire after discharge process in **Figure** 4.8

c/a = 1.17			a=5.5 Å	c=9.15 Å
			Exp.	Cal.
h	k	l	d (Å)	d (Å)
1	1	0	3.891	3.889
2	1	1	2.370	2.375
2	2	0	1.946	1.945
3	0	1	1.799	1.798
4	1	1	1.325	1.320
3	3	0	1.297	1.296
3	3	2	1.245	1.247
4	2	2	1.188	1.188
5	1	2	1.052	1.050

APPENDIX C. TED patterns

The TED pattern obtained from the phase boundary area.

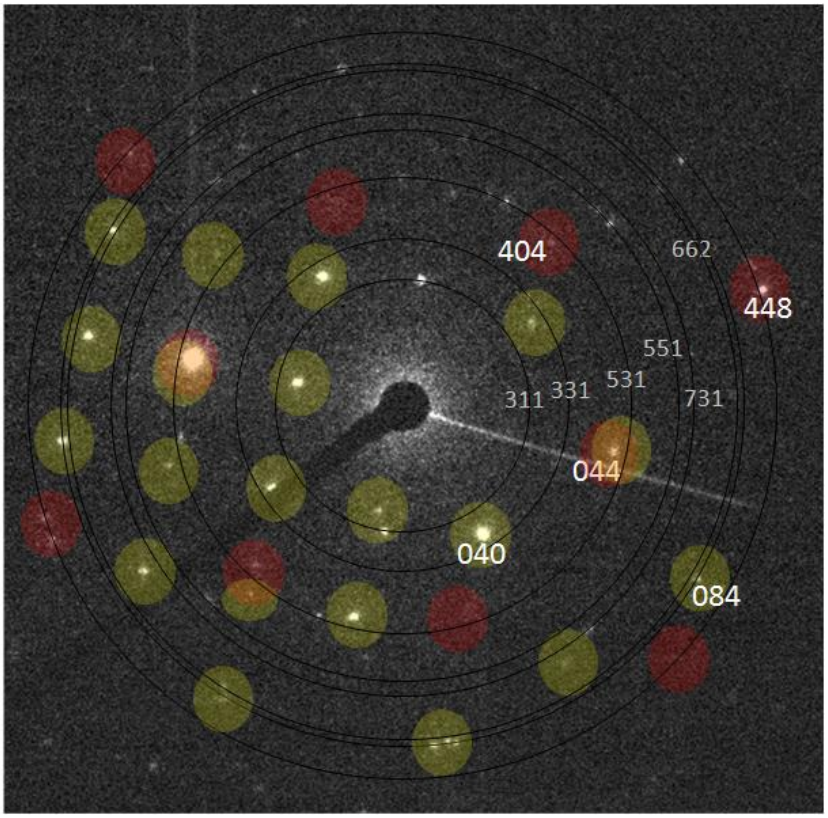

Figure A2. Enlarged TED pattern of **Figure** 5.5(b). The spots of $LiMn_2O_4$ spinel structure viewed from the [100] direction and from the [111] direction are marked by yellow shade circles and red ones, respectively. Additional spots can be also indexed by cubic spinel structure (black rings).

The intensity of diffraction spots in TED images obtained in experiment.

In order to determine the sample thickness and lithium composition of each phase (Li-rich and Li-poor phases), the intensity of diffraction spots in TED images were investigated by comparing the calculated results. The intensity ratio between three spots, 220 spots, 224 spots and 440 spots, was used to compare the calculated results. The comparison was performed with the ratio of log-scale intensity of each spots.

As all TED patterns was obtained in same nanowire and obtained at the edge area of the nanowire, the thickness was assumed to be same. The thickness was determined with the criterion that the proper thickness should allow all the intensity ratios in three TED images obtained with pristine sample, in Li-rich phase and in Li-poor phase.

The image intensities of each diffraction spot in three TED images are shown in Figure A3. From the TED of pristine sample (Figure A3.a), the ratio of log-scaled intensity of 440 spot to 220 spot (log I_{440} / log I_{220}) was 1.11 ± 0.07. (The error is the standard deviation from 6 pairs of 220 and 440 spots.) The ratio of (log I_{224} / log I_{220}) was 0.89 ± 0.08. From the TED of Li-rich phase, the ratio of log I_{220} / log I_{440} was 0.80±0.016 (Figure A3.b). In the TED of Li-poor phase, Since 220 spot was not detected, we assume the intensity of 220 spot should be lower than noise level. We put the intensity of 220 spot as $I_{220} < I_{mean} + 2\sigma$, where I_{mean} is background mean intensity and σ is the standard deviation of background intensities. The ratio of log I_{220} / log I_{440} was less than 0.55 (Figure A3.c).

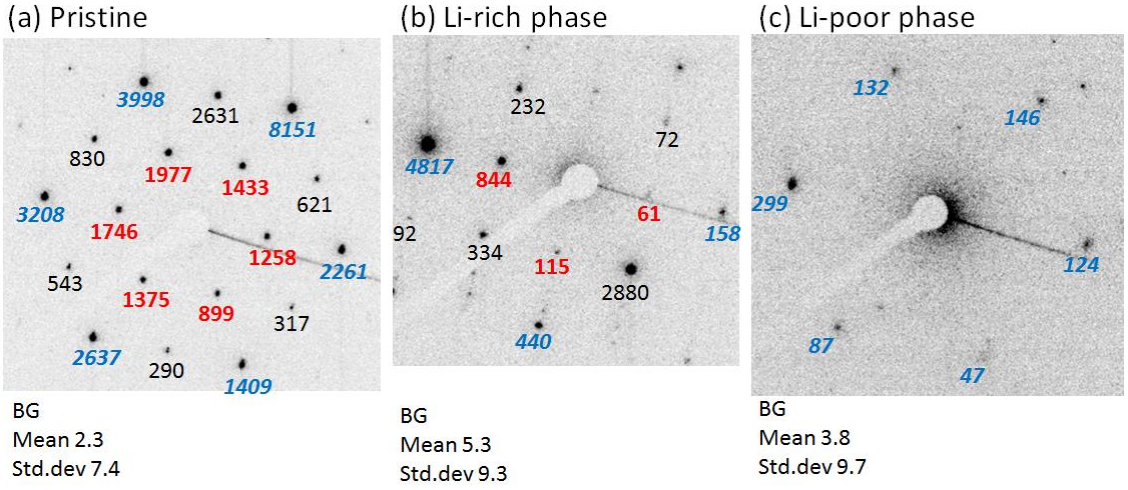

Figure A3. Experimentally obtained TED patterns with image intensities of diffraction spots. (a) TED patterns obtained from pristine sample, (b) TED pattern obtained from Li-rich phase, (c) TED pattern obtained from Li-poor phase. (a) is the enlarged TED corresponding to the TED in the inset of Figure 5.1b, (b) and (c) corresponding to the TEDs in Figure 5.4a and c, respectively. Measured image intensities of 440 diffraction spots are shown as blue numbers, those of 220, as red numbers.

The calculated intensity ratios are shown Figure A4. Figure A4(a) shows the intensity ratio of 440 and 220 spots as blue line, and shows the intensity ratio of 224 and 220 spots as red line. Each line is a function of thickness with the lithium composition of x=1. We assumed that the pristine nanowire would have lithium composition of x~1, and compared the ratios from the experimentally obtained TED (blue horizontal bend corresponds to the ratio of 440 to 220 spot; red bend, the ratio of 224 to 220 spot) and theoretically calculated TED. There are three thickness points where the experimental intensity ratios are coincident with the calculated ones: 17 nm, 40 nm and 134 nm.

Figure A4(b) shows the intensity ratio of 220 and 440 spots in <111> orientation TED for 17 nm thickness as blue line, 40 nm as red and 134 nm as green. Each line is a function of the lithium composition, x in $Li_xMn_2O_4$. Since the experimental intensity ratio from Li-poor phase is less than 0.55, 134 nm thickness can be excluded.

Figure A4(c) shows the intensity ratio of 220 and 440 spots in <100> orientation TED for 17 nm thickness as blue line and 40 nm as red one. Each line is a function of the lithium composition, x in $Li_xMn_2O_4$. Since the experimental intensity ratio from Li-rich phase is about 0.80, 17 nm thickness can be excluded. The proper sample thickness is determined as 40nm. Even though the thickness of observed sample is not constant due to thickness gradient, we regard 40nm as effective mean thickness of the sample.

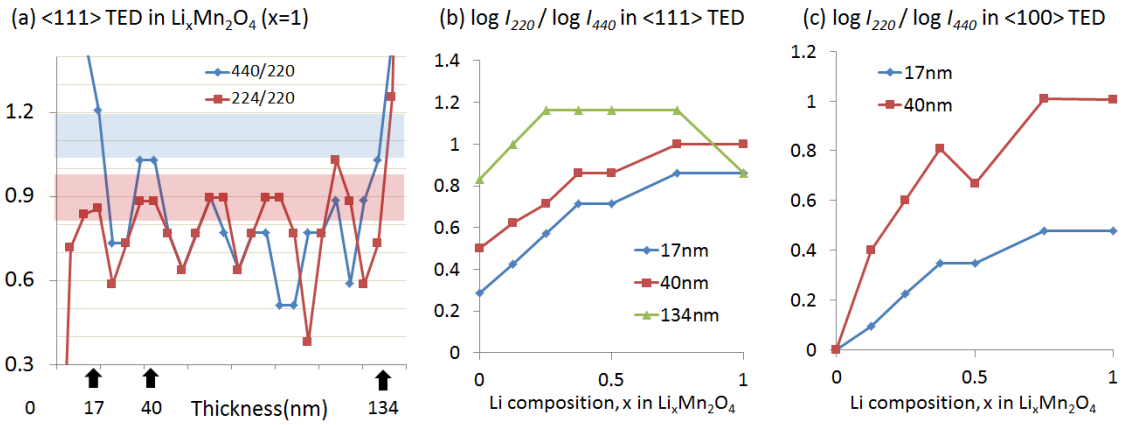

Figure A4. The ratio of log-scaled intensity of diffraction spots from the theoretical calculation results. (a) The ratio of log-scale intensity of 440 spot to 220 spot (log I_{440} / log I_{220})(blue line) and the ratio of log-scale intensity of 224 spot to 220 spot (log I_{440} / log I_{220})(red line) in <111> orientation TED pattern are plotted as functions of sample thickness. (b) The ratios of log-scale intensity of 220 spot to 440 spot (log I_{220} / log I_{440}) in <111> orientation TED pattern are plotted as functions of lithium composition, x. The plots for three thicknesses, 17, 40 and 134 nm are shown as blue, red and green lines respectively. (c) The ratios of log-scale intensity of 220 spot to 440 spot (log I_{220} / log I_{440}) in <100> orientation TED patterns for two thicknesses, 17 (blue) and 40 (red) are plotted as functions of lithium composition, x.

Publication

This thesis comprises the following publications (1~5). But the paper (6) is not included

Original paper

1. Soyeon Lee, Yoshifumi Oshima, Hidetaka Sawada, Fumio Hosokawa, Eiji Okunishi, Toshikatsu Kaneyama, Yukihito Kondo, Seiji Niitaka, Hidenori Takagi, Yasumasa Tanishiro and Kunio Takayanagi, "Counting lithium ions in the diffusion channel of an LiV_2O_4 crystal", *Journal of Applied Physics*, **109**, 113530 (2011)

2. Soyeon Lee, Yoshifumi Oshima, Seiji Niitaka, Hidenori Takagi, Yasumasa Tanishiro, and Kunio Takayanagi," *In-situ* Annular Bright-Field Imaging of Structural Transformation of Spinel LiV_2O_4 Crystals into Defective LixV2O4", *Jpn. J. Appl. Phys.* **51,** 020202 (2012)

3. Soyeon Lee, Yoshifumi Oshima, Hidetaka Sawada, Fumio Hosokawa, Eiji Okunishi, Toshikatsu Kaneyama, Yukihito Kondo, Yasumasa Tanishiro and Kunio Takayanagi, "Surface Imaging by ABF-STEM: Lithium Ions in Diffusion Channel of LIB Electrode Materials", *e-J. Surf. Sci. and Nanotech.* **10,** 454-458 (2012)

4. Soyeon Lee, Yoshifumi Oshima, Eiji Hosono, Haoshen Zhou and Kunio Takayanagi, "Reversible Contrast in Focus Series of Annular Bright Field Images of a Crystalline $LiMn_2O_4$ Nanowire", *Ultramicroscopy* **125**, 43–48 (2013)

5. Soyeon Lee, Yoshifumi Oshima, Eiji Hosono, Haoshen Zhou, Kyungsu Kim, Hansen M. Chang, Ryoji Kanno, and Kunio Takayanagi, "*In Situ* TEM Observation of Local Phase Transformation in a Rechargeable $LiMn_2O_4$ Nanowire Battery", *J. Phys. Chem. C*, **117** (46), 24236–24241 (2013)

6. S. Niitaka, H. Ohsumi, K. Sugimoto, S. Lee, Y. Oshima, K. Kato, D. Hashizume, T. Arima, M. Takata, and H. Takagi, "A-type antiferro-orbital ordering with I41/a symmetry and geometrical frustration in the spinel vanadate MgV_2O_4", *Phys. Rev. Lett* **111**, 267201 (2013)

Review paper

7. K. Takayanagi, S. Kim, S. Lee, Y. Oshima, T. Tanaka, Y. Tanishiro, H. Sawada, F. Hosokawa, T. Tomita, T. Kaneyama and Y. Kondo, " Electron microscopy at a sub-50 pm resolution", *J. Electron Microsc*. **60,** S239–S244 (2011)

8. 大島　義文、李　少淵、高柳　邦夫, "超高分解能電子顕微鏡によるリチウム原子の可視化"、*真空* **55(4)** (2012)

9. 大島　義文, 李　少淵, 高柳　邦夫, 収差補正ABF-STEM 法によるLi 原子の直接観察, *顕微鏡*, **47**, 144-148 (2012)

10. 高柳邦夫, 大島義文, 李少淵, 田中崇之, 谷城康眞, 収差補正電子顕微鏡と表面・界面科学表面科学, **34**, 226 (2013)

My contribution to the papers in this thesis (paper 1~5)

Paper 1. Evaluation of data; writing the manuscript.

Paper 2. Planning experiment; performing experiment except synthesis LiV_2O_4 crystals (S. Niitaka); evaluation of data; writing manuscript.

Paper 3. Planning experiment; performing experiment except synthesis $LiMn_2O_4$ crystals (S. Niitaka); evaluation of data; writing manuscript.

Paper 4. Planning experiment; performing experiment except synthesis $LiMn_2O_4$ nanowire (E. Hosono); evaluation of data; writing manuscript.

Paper 5. Planning experiment; fabrication of 'nanobattery' except synthesis $LiMn_2O_4$ nanowire (E. Hosono). $Li_4Ti_5O_{12}$ anode fabrication in collaboration with H. Chang and K. Kim; developing *in-situ* observation system with Y. Oshima; performing *in-situ* TEM observation; Evaluation of data; writing manuscript.

All papers were discussed with Y. Oshima and K. Takayanagi.

Paper 5 was discussed with H. Zhou, K. Kim, R. Kanno.

Acknowledgement

I am so gratiful to all people who have made my Ph. D thesis completed.

First, I'd like to show my deep thanks to my supervisor, Prof. Takayanagi, who has given me the chance to glance the beautiful nano-world. Always, he inspires me not only to consider a matter from various anles and but also to grip the essential which hides in matters. Without his kind teaching and passion for physics my thesis would not be completed. At the starting point as a researcher, his messages and instructions will never be forgotten.

I am grateful to my co-supervisor, Prof. Yamamoto for his kind instruction and discussion. I can not forget the scence that he teachs all his students how to use the instruments by himself. I am grateful to Assist. Prof. Tanishiro for his help and advices, and also Assist. Prof. Tanaka.

From my colleagues and alumni, I have been received unaccountable supports. Special thanks to Suhyun Kim, who is like my eldder brother, and one of role model. Owing to his help, I could start my graduate life. He had supported me not only by moral but also with knowledge and food. I never forget the one and half of year with him. Thank Abe san, for teaching me how to use the instruments in laboratory including TEM and STEM. He also teached me how to use the TEM simulation program. I am grateful to Sumiya san, Takeshita san and Suzuki san. They helped me to adapt new Japanese life. I also thank Wada san, Izumihara san, Koyanagi san and Zhang san for their friendship. I would like to thank secretary Ms. Mori, who is like a mother for our laboratory. I would like to thank Mr. Endo for teaching me the basic knowledge of TEM. And thank all of my colleagues and alumni.

I am so grateful to Dr. Sawada at JEOL. He had teached me how to operate the beautiful TEM, Roo5 – STEM, EELS and correction of aberrations. The lithium imaging method, ABF imaging was also taught by Dr. Sawada. He is also 'sensei' for me. I would like to thank Dr. Endo at JEOL for his meaningful advices on EELS. I thank Dr. Sannomiya for kind explanation of aberration.

I am also grateful to Mr. Omori at Kitano Seiki for developing special TEM holder for *in-situ* observation together. His sophisticated manufacturing ability enabled the developing.

I thank the members of Kanno lab. Kyungsu Kim has taught me how to obtain and anaylize the electrochemical properties of LIBs - Thank you Kim san. Hansen Chang had taught how to fabricate the coin cell with $Li_4Ti_5O_{12}$ powder. Sanryun Kim and me have collaborated, with my sample and his sample. I wish bigbang with next new samples. Jaemin Im gave me a joy by chattering in Korean.

I am grateful to Dr. Zhou and Dr. Hosono for providing excellent $LiMn_2O_4$ nanowire and excellent advices. The nanowire $LiMn_2O_4$ has been the most suitable sample for *in-situ* observation.

I would like to thank KOBAYASHI internation scholarship foundation for financial support.

I would like to show my deep thanks to co-advisor, Prof. Oshima. He have everyday called me and given me instructions. He never hesitated to scole me when I selected wrong way. Somtimes It looked tiresomes and sometimes very precious. However, his passion and patience transformed me into self-supportive individual. He had taught not only knowledge but also life habit as a fresh researcher. Without his support, my Ph. D project could not bear any fruitful results.

I owe my thanks to my wife, Jiyoung Choi, who is the most lovely woman. With her devotion for supporting daily life, especially taking care my son, I could focus on my research and study.

Finally, Thank all my Japanese and Korean friends and teachers. And Great thanks to God for giving amazing opportunity and keeping my graduate life.

Tokyo, February 2014

Soyeon Lee